



# Ice Sheets & Ice Cores

Data Analysis & Stochastic Modeling



**Ph.D. Thesis**

Troels Bøgeholm Mikkelsen, February 2017

Submitted to the University of Copenhagen, Faculty of Science

**Academic Advisors:**

Peter D. Ditlevsen (supervisor)

Susanne Ditlevsen (co-supervisor)

THIS THESIS HAS BEEN SUBMITTED TO THE PHD SCHOOL OF THE FACULTY  
OF SCIENCE, UNIVERSITY OF COPENHAGEN  
IN PARTIAL FULFILLMENT OF THE REQUIREMENTS OF THE PHD PROGRAM

ACADEMIC ADVISORS:

Peter D. Ditlevsen (supervisor)

Susanne Ditlevsen (co-supervisor)

SUBMITTED: February 24th, 2017

DEPARTMENT: Centre for Ice and Climate, Niels Bohr Institute

AUTHOR: Troels Bøgeholm Mikkelsen

TITLE: Ice Sheets & Ice Cores

SUBTITLE: Data Analysis & Stochastic Modeling

SUBJECTS: Climate physics | Ice cores | Ice sheets | Time series analysis |  
Dynamical systems | Stochastic modeling | Transfer operators

FRONT PAGE: EastGRIP – The East Greenland Ice Core Project – is a current  
multinational endeavor to obtain an ice core from the Northeast Greenland Ice  
Stream ([eastgrip.org](http://eastgrip.org)).

The front page picture is of the EastGRIP camp (see Figure 1.1) and was  
taken by the author in July, 2016.

git revision: 8d26d9c (2017-02-23)

## Abstract

Since the discovery of the Ice Ages it has been evident that Earth's climate is liable to undergo dramatic changes. In recent years the debate concerning global warming has prompted a great effort to understand the dynamics of Earth's climate.

The previous climatic period known as the Last Glacial saw large fluctuations in the extent of ice sheets covering the Northern hemisphere, and in the temperature over Greenland. These fluctuations are known as Dansgaard-Oeschger (DO) events after their discoverers. While the evidence for the fluctuations is solid, their causes are not yet fully understood. An improved understanding of the DO events would add to our knowledge of the climatic system and – hopefully – enable better forecasts. Likewise, to forecast possible future sea level rise, it is crucial to correctly model the large ice sheets on Greenland and Antarctica.

This project is divided into two parts. The first part concerns time series analysis of data from the NGRIP ice core obtained from the Greenland Ice Sheet. After introducing the appropriate theory we analyze parts of the time series where DO events occur using the transfer operator, and compare the results with time series from a conceptual double well model. This model is capable of undergoing transitions caused by 1) a bifurcation resulting from a slow parameter change, or 2) stochastic fluctuations. We find that the DO event time series is most consistent with the model undergoing a stochastic transition. Several previous studies have found that the DO transitions most likely happen at random, while other studies have reported early warning signals, excluding a stochastic transition. Our analysis supports the first scenario using a method that – to the author's knowledge – has not been used for this problem before.

In the second part we use a minimal complexity ice sheet model subject to constant and fluctuating temperatures, respectively. We find that the steady state volume of the ice sheet is lower for fluctuating temperatures than for a constant temperature. We obtain an analytical relationship between the two steady state volumes, and evaluate this numerically. The agreement is found to be good. This finding may have implications for future long-range ice sheet projections, as the steady state ice sheet volume could be underestimated in studies using a constant temperature.

Noise in the climate system may be interpreted as “the weather”. This study illustrates that noise may play a role both in a deterministic sense – as changing the steady state of a system – and in a non-deterministic sense, causing the climate system to change state.



## Resumé på Dansk

Siden istiderne blev opdaget har det været klart at Jordens klima tidligere har oplevet store forandringer. De seneste års debat om global opvarmning har motiveret en omfattende indstats rettet mod at forstå dynamikken i Jordens klima.

I den seneste klimatiske periode, den sidste istid, var der store udsving i udbredelsen af iskapper på den nordlige halvkugle, og i temperaturen i Grønland. Disse udsving kaldes DO begivenheder efter deres opdagere. Beviserne for disse DO-begivenheder er klare, men årsagerne er endnu ikke fuldt klarlagt. En forbedret forståelse af DO-begivenhederne vil bidrage til vores viden om det klimasystemet og – forhåbentlig – gøre os i stand til at lave bedre forudsigelser. Ligeledes er det essentielt at være i stand til på korrekt vis at modellere de store iskapper i Grønland og på Antarktis for at forudsige eventuelle fremtidige stigninger i havniveau.

Denne afhandling er inddelt i to. Den første del omhandler tidsserieanalyse af iskernedata fra den Grønlandske iskappe. Efter at have introduceret den nødvendige teori, analyserer vi de dele af tidsserierne hvor DO-begivenhederne fremstår ved at bruge den såkaldte ‘transfer operator’. Dernæst sammenligner vi resultaterne med en analyse af tidsserier fra en konceptuel model der kan skifte tilstand på to måder, enten 1) som følge af en bifurkation i systemet på grund af langsom drift af en parameter, eller 2) som følge af et stokastisk spring. Vi finder at tidsserien med DO-begivenheder er mest konsistent med modellen i det tilfælde hvor den springer stokastisk. Flere tidligere studier finder at DO begivenhederne mest sandsynligt sker tilfældigt, mens andre studier har rapporteret ‘early warnings’ – det sidste udelukker tilfældige skift. Vores analyse støtter således det førsnævnte scenarie med en metode der – såvidt vi ved – ikke tidligere blevet anvendt på dette problem.

I den anden del af afhandlingen bruger vi en simpel model af en iskappe og udsætter den for henholdsvis konstant og tidsligt svingende temperatur. Vi finder at ligevægtsvolumenen af iskappen er mindre når temperaturen svinger. Vi udleder et analytisk udtryk for forskellen i isvolumen imellem de to tilfælde, og evaluerer dette udtryk numerisk. Sammenhængen mellem simulationer og den analytiske tilgang er god. Dette bidrag kan have betydning for fremtidige iskappesimulationer, da ligevægtsvolumenen af iskappen muligvis overvurderes såfremt man bruger en konstant temperatur i modellerne.

I klimasystemet kan man tænke på “vejret” som “støj”. Dette studie illustrerer at støj både kan spille en rolle i en deterministisk forstand – ved at sænke ligevægtsvolumenen af en iskappe – og i en ikke-deterministisk forstand, ved at forårsage store ændringer i klimasystemet.



# Preface

## Previous Work by the Author

I have previously written a short course paper (Mikkelsen 2012) on the topics of dynamical systems and bifurcations that included numerical analysis of the Lorenz (1963) system and the logistic map (eg. Strogatz (1994)).

Next my Master's thesis (Mikkelsen 2013) dealt with the Duffing Oscillator (eg. Guckenheimer and Holmes (1983)) and the occurrence of Arnold tongues in its parameter space and the numerical and theoretical analysis of these phenomena.

The two main themes in this thesis are 1) ice core data analysis and 2) ice sheet modeling, neither of which featured in Mikkelsen (2012) or Mikkelsen (2013). As both this thesis and the two mentioned studies employ the theory of dynamical systems and numerical methods, they necessarily draw on a common body of well known theory; some overlap is natural. When such theory is introduced in this thesis, I will refer to original sources and textbooks only.

## Acknowledgements

First I would like to thank my supervisor Peter Ditlevsen and co-supervisor Susanne Ditlevsen, both for advice and for always asking interesting questions. I also thank Helle Kjær and Anne Solgaard for advice and helpful discussion on my Ph.D. panel. It has been hard not to be infected by the enthusiasm of Aslak Grinsted who collaborated with Peter and me on the manuscript presented in Appendices D and E. I am grateful to Johannes Oerlemans for sharing the Fortran code for the model he presented in Oerlemans (2003) and to Alexander Robinson for sharing the results from Robinson et al. (2012).

The Centre for Ice and Climate (CIC) has been a tremendous place to work and I am grateful to all my colleagues for making CIC feel like a second home. The ice coring business is definitely a team effort, and so I am much obliged to the teams drilling the North Greenland Ice Core Project (NGRIP) ice core and turning it into useful data.

It was a wonderful adventure to be a part of the EastGRIP camp, and I thank everybody involved; especially Sune Olander Rasmussen, Dorthe Dahl-Jensen, Jørgen Peder Steffensen, Lars Berg Larsen, Thomas Blunier, Marie Kirk, and chiefs of the EastGRIP storytelling team, Trevor & Steff. Running a camp like EastGRIP would be close to impossible without Arctic/Antarctic mechanic, Sverrir Hilmarsson. It was a pleasure flying to the ice with the 109th Airlift Wing and I will never forget the experience of standing behind the running engines of a LC-130 Hercules on the Greenland Ice Sheet; incidentally the

same place as Bill Nye the Science Guy presented the EastGRIP crew members, myself included, with a wonderfully inspiring quote (reproduced below) in July, 2016.

I look forward to future collaboration with Lisbeth Tangaa Nielsen on exploring the results of running the Parallel Ice Sheet Model (PISM) with fluctuating temperature, hopefully expanding on the results in the manuscript in Appendix D. Thanks also goes to Anders Svensson and Thomas Blunier for being very helpful with providing and interpreting ice core data.

I thank Holger Kantz and Henk Dijkstra, as well as the MPI-PKS and IMAU staff for tremendous hospitality during my stays abroad, as well as Henk Dijkstra, Alexis Tantet and Mickaël Chekroun for valuable discussions on applications of the transfer operator

Ellen Chrillesen and Lone Hansen have made life on CIC much easier, and NBI librarians Lisbeth Dilling and Kader Ahmad have always been helpful. My office mate Marius Simonsen has hosted a vast array of inspiring discussions over time, on topics such as morals, physics, fixing democracy and leading a good life. I thank my friend Jacob Østergaard for suggesting clarifications on an early version of Chapter 2. A tip of the hat goes to the global [Stackexchange](#) community, especially for coding tips.

I thank very warmly my family and friends, and finally Randi Keinicke Nielsen for her service as Field Doctor at EastGRIP, and for putting up with me during the writing of this thesis.

*“Don’t blow it!”*

– **Bill Nye**

# Contents

<b>Abstract</b>	<b>iii</b>
<b>Resumé på Dansk</b>	<b>v</b>
<b>Preface</b>	<b>vii</b>
Previous Work by the Author . . . . .	vii
Acknowledgements . . . . .	vii
<b>Contents</b>	<b>ix</b>
<b>1 Introduction &amp; Scientific Background</b>	<b>1</b>
1.1 A Brief Look at Earth's Climatic History . . . . .	1
1.2 Ice Cores & Dansgaard-Oeschger Events . . . . .	2
1.3 Previous Research on Tipping Points . . . . .	6
1.4 Applications of the Transfer Operator . . . . .	12
1.5 Outline . . . . .	13
<b>2 Time Series Analysis and Modeling</b>	<b>15</b>
2.1 Time Series From Dynamical Systems . . . . .	15
2.2 Autoregressive Processes . . . . .	16
2.3 Stochastic Differential Equations . . . . .	17
2.4 Detrending . . . . .	21
2.5 The Transfer Operator . . . . .	22
2.6 Relating the Spectra of the Liouville and Transfer Operators . . . . .	28
2.7 Decay of Correlations . . . . .	30
2.8 Ulam Approximation of the Transfer Operator . . . . .	32
2.9 Estimating Errors on Markov Matrices . . . . .	34
2.10 The Transfer Operator and Noise . . . . .	35
2.11 How to Apply the Transfer Operator . . . . .	38
<b>3 Bifurcations and Tipping Points</b>	<b>41</b>
3.1 Linear Stability Analysis . . . . .	41
3.2 Some One-Parameter Bifurcations . . . . .	42
3.3 Bifurcations and Noise – Early Warning Signals . . . . .	46
<b>4 A Conceptual Model of Dansgaard-Oeschger Events</b>	<b>49</b>
4.1 1D and 2D Double Well Models . . . . .	49
4.2 Analysis of Data From the Double Well Models . . . . .	50
4.3 Parameter Variation for the Spectral Gap Computations . . . . .	58

<b>5</b>	<b>Ice Core Data Analysis</b>	<b>61</b>
5.1	Climate Proxies . . . . .	61
5.2	Data and Methods . . . . .	64
5.3	Analysis Using the Transfer Operator . . . . .	74
5.4	Varying Parameters in the Transfer Operator Analysis . . . . .	78
5.5	Discussion . . . . .	82
<b>6</b>	<b>Minimal Ice Sheet Model With Stochastic Forcing</b>	<b>83</b>
6.1	Summary of Mikkelsen et al. (2017) . . . . .	83
6.2	Discussion . . . . .	85
6.3	Ideas for Future Work . . . . .	85
<b>7</b>	<b>Discussion &amp; Conclusion</b>	<b>87</b>
7.1	Transfer Operator Analysis of NGRIP Data . . . . .	87
7.2	Minimal Ice Sheet Model With Stochastic Forcing . . . . .	88
<b>A</b>	<b>List of Acronyms</b>	<b>89</b>
<b>B</b>	<b>Numerical Tools</b>	<b>93</b>
B.1	Libraries Developed and Reproducibility of Results . . . . .	93
B.2	Python Tools Used . . . . .	94
B.3	MATLAB Tools Used . . . . .	95
<b>C</b>	<b>Co-Author Statements</b>	<b>97</b>
<b>D</b>	<b>Influence of temperature fluctuations on equilibrium ice sheet volume</b>	<b>99</b>
<b>E</b>	<b>Supporting Information for “Influence of temperature fluctuations on equilibrium ice sheet volume”</b>	<b>115</b>
	<b>Bibliography</b>	<b>125</b>

# 1 Introduction & Scientific Background

This work consists of two parts. The first part is concerned with time series analysis of ice core data from a Greenland ice core in order to determine whether early warning signals (EWS) can be found before the onset of Dansgaard-Oeschger (DO) events, large past fluctuations in Greenland temperature. We use a method based on the transfer operator that – to the author’s knowledge – has not been used for this purpose and in this way before. This part is presented in Chapters 2 to 5.

In the second part, we use a simple ice sheet model that takes surface temperature as the only forcing input and investigate the consequences of letting the temperature fluctuate from year to year. This part is presented in the manuscript Mikkelsen et al. (2017) in Appendices D and E, which is summarized in Chapter 6.

In Section 1.1 we take a look at the fascinating history of Earth’s climate from about 715 million years (Ma) ago to the present. Unless otherwise noted, Section 1.1 is based on Ruddiman (2013, Chapters 4–13). Section 1.2 presents the history leading up to the discovery of DO events as well as hypotheses for their causes.

In Section 1.3 we review earlier work focused tipping points and their detection, with special emphasis on time series analysis of ice core data. We digress slightly and mention other related areas of active research.

Both theory and possible applications of the transfer operator are being actively researched. In Section 1.4 we review a few recent papers where this approach has been applied to data from climate models. Finally we outline the rest of this thesis in Section 1.5.

## 1.1 A Brief Look at Earth’s Climatic History

Changes in Earth’s climate have taken place on very different time scales. These are commonly referred to by the processes that are relatively most important on that particular time scale (Bartlein 2013). On tectonic time scales (10–400 Ma) significant processes are the motion – and collision – of Earth’s continents, and removal of CO<sub>2</sub> from Earth’s atmosphere by weathering.

The amount of insolation – incoming solar radiation – varies on orbital timescales (20–400 kilo years (ka)) due to changes in the Earth’s axis of rotation, precession of the same axis, as well as precession and change in eccentricity of Earth’s orbit around the Sun. This phenomenon is often called Milankovitch

cycles after the astronomer who proposed the influence of orbital changes on the insolation received on earth (Lowe et al. 2013).

The DO events happen on sub-orbital, millennial time scales (Dansgaard et al. 1993; Wolff et al. 2010; Bartlein 2013). On even shorter time scales, prominent examples of climatic variability are the El Niño-Southern Oscillation (ENSO) (sub-decadal) as well as the annual cycle.

The climate of the Earth has varied significantly in the past. Glacial deposits on several continents suggest that glaciers existed in what is now the tropics about 715 – 640 Ma ago, and that the Earth was near completely frozen in some periods, the so-called “Snowball Earth.”

At the other extreme, fossil records indicate that around 100 Ma the South Pole may have been completely ice free. Sea levels at this time were likely 80 meters higher than today, and the South Pole up to 40°C warmer, termed the “Greenhouse Earth.”

Approximately 50 Ma ago a gradual cooling started, as indicated by fossil evidence and  $\delta^{18}\text{O}$  data obtained from benthic foraminifera, tiny ocean bottom dwelling shelled organisms. This cooling continued, and 2.75 Ma ago progressively larger ice sheets would periodically appear and disappear in the Northern Hemisphere. These ice sheets became more prominent from 600 ka ago; the last 600 ka has seen 6 glacial periods – or glacials – with large portions of the Northern Hemisphere covered in ice. Each glacial is followed by an interglacial with significantly smaller ice sheets. The last of these interglacials is the present period, the Holocene.

The Last Glacial culminated in the Last Glacial Maximum (LGM) about 21 kilo years before year 2000 (ka b2k). At this time, ice sheets covered large parts of North America and Europe. The amount of ice is estimated to correspond to a decrease in sea level of more than 100 meters compared to present levels.

The Last Glacial started with a gradual cooling from  $\sim 122$  ka b2k to  $\sim 115$  ka b2k (NGRIP 2004) and ended with large fluctuations; from glacial to mild conditions during the Bølling-Allerød (BA) ( $\sim 14.6$ – $12.9$  ka b2k) and back into glacial conditions during the Younger Dryas (YD) ( $\sim 12.9$ – $11.7$  ka b2k), after which the Holocene started (Steffensen et al. 2008; Rasmussen et al. 2014).

## 1.2 Ice Cores & Dansgaard-Oeschger Events

Dansgaard et al. (1982) compared a newly drilled ice core from the Distant Early Warning Line (Cape Dyer), Station 3 (DYE-3) to a core previously drilled at Camp Century (Figure 1.1). In the Camp Century core, large fluctuations in  $\delta^{18}\text{O}$  – a proxy for site temperature (Section 5.1) – had been observed in ice from the Last Glacial period. However, it was not clear whether the fluctuations in the Camp Century core were of a local nature.

Camp Century and DYE-3 were drilled 1400 km apart and  $\delta^{18}\text{O}$  in the two cores were found to correlate well. Thus Dansgaard et al. (1982) found support for the hypothesis that these fluctuations were not of a local nature, but rather a consequence of climatic events affecting the North Atlantic region in general. The DYE-3 site was not optimal for drilling since it was chosen for logistical reasons; the “well-equipped” (Dansgaard et al. 1982) American radar station DYE-3, part of the distant early warning (DEW) line, was already situated on the ice cap (Lackenbauer et al. 2005).

In contrast to DYE-3, the Greenland Ice Core Project (GRIP) core was drilled in much better locations at Summit with minimal horizontal ice flow and negligible summer melting; both may disturb the signal (Johnsen et al. 1992). The results from Camp Century and DYE-3 were reproduced by Johnsen et al. (1992) and Dansgaard et al. (1993) using data from the GRIP core, and by Grootes et al. (1993) using data from the Greenland Ice Sheet Project 2 (GISP2) core; GRIP and GISP2 are situated about 28 km apart. As the  $\delta^{18}\text{O}$  variations could now be excluded to be of a local nature, and as similar signal were found in ocean cores, Dansgaard et al. (1993) and Grootes et al. (1993) concluded that the cause of the  $\delta^{18}\text{O}$  signal was large scale atmospheric events in the Northern Hemisphere.

It turned out that the bottom  $\sim 10\%$  of ice in both the GISP2 and GRIP cores were disturbed, ultimately leading to the drilling of the North Greenland Ice Core Project (NGRIP) core (NGRIP 2004).

The amplitudes of the DO events were quite dramatic, with Greenland temperature variations from  $5^\circ\text{C}$  to  $16^\circ\text{C}$  between the cold Greenland Stadials (GSs) and the warm Greenland Interstadials (GIs) on a decadal scale (Rasmussen et al. 2014). Some GIs saw Greenland temperatures almost as warm as today (Lowe et al. 2013).

### 1.2.1 Probable Cause for the Dansgaard-Oeschger Events

Since the DO events happen on a sub-orbital time scale, an explanation cannot be sought only in terms of Milankovitch forcing (Lowe et al. 2013). There is a general agreement that the DO events are connected with changes in the thermohaline circulation (THC).

The THC is a driving mechanism for large ocean currents whereby warm sea water is transported from the tropics and subtropics to higher latitudes; here, in the deep water formation zones (such as the Greenland-Norwegian Sea, The Labrador Sea, The Ross and Weddell Seas), the warm water releases some of its heat (Rahmstorf 2013). Note that these deep water formation zones include Antarctic waters. Cold water is then transported at depth to upwelling zones; these are much less well defined and localized than the deep water formation areas. Heat is required for the deep, cold water to rise to the surface; this heat is supplied from the surface by turbulent mixing (Rahmstorf 2013). The THC is thus primarily driven by heat, although increased salinity in the deep water formation areas create a positive feedback (Rahmstorf 2013).

The THC is thus one of the driving mechanisms for the Atlantic Meridional Overturning Circulation (AMOC), the Atlantic north-south flow, where another significant driver is the wind. We note that the two terms THC and AMOC are often (incorrectly) used interchangeably (IPCC 2013) – Rahmstorf (2013) makes the distinction between the THC as a *mechanism* on the one hand, and the AMOC as a *measurable quantity* (in principle) on the other. The AMOC has a significant influence on the Northern hemisphere, at present transporting about 15 Sverdrup (Sv) (1 Sv is  $10^6 \text{ m}^3/\text{s}$ ) of sea water and 1.2 PW of heat (Rahmstorf 2013).

Johnsen et al. (1992) argue that the DO events were likely caused by changes in the intensity or direction of the AMOC. Grootes et al. (1993) note that the rapidity of the DO events excludes causes such as changes in insolation, deep water transport or global ice volume, since these phenomena happen on a much

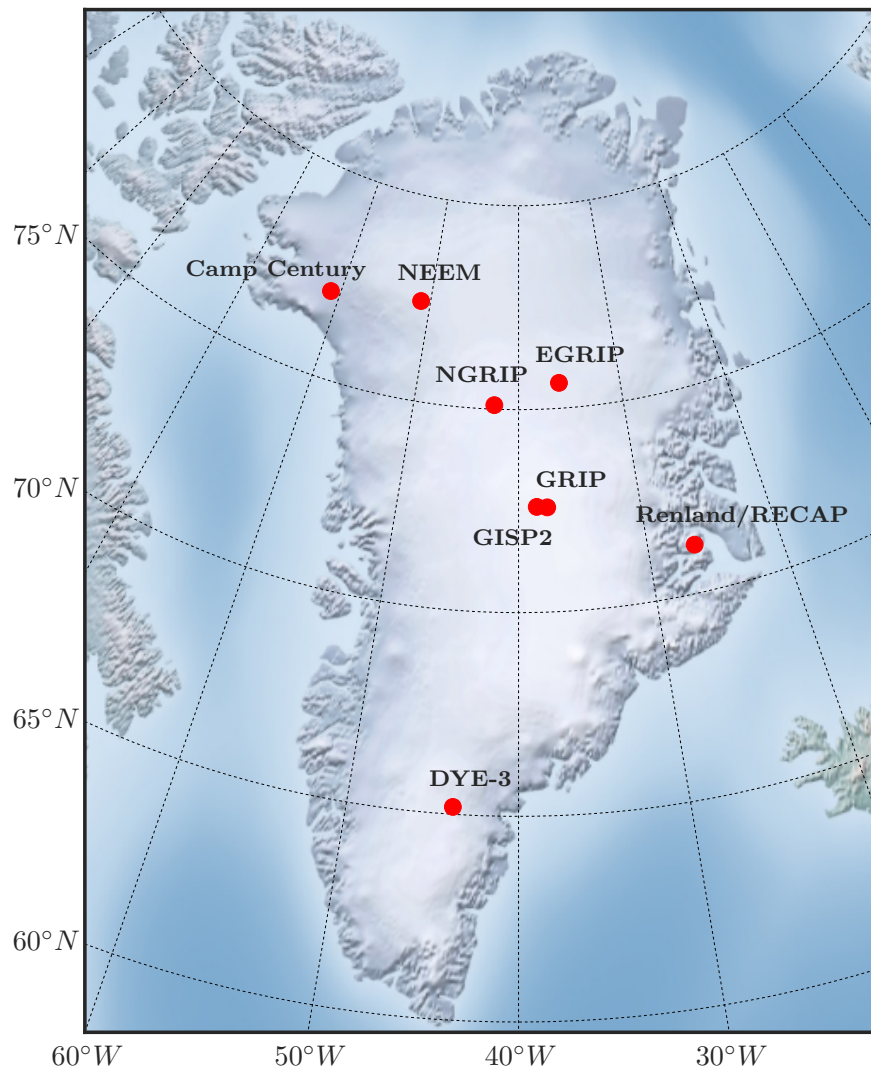


**Figure 1.1 | Ice core drill sites.** Location of NGRIP, GRIP and DYE-3 from Vinther et al. (2006); North Greenland Eemian Ice Drilling (NEEM) location from Rasmussen et al. (2013); East Greenland Ice-core Project (EGRIP) location from Dahl-Jensen et al. (2016); GISP2 location from Wolff et al. (2010); Renland & Camp Century from private communication with J. P. Steffensen.

longer time scale than the DO – thus the causes are likely atmospheric forcing, or North Atlantic Ocean mixed layer<sup>1</sup> forcing (Grootes et al. 1993).

If a decrease in the AMOC is responsible for Greenland *coolings* then one would expect to see a *warming* in the Southern hemisphere, and vice versa for Greenland warmings; this idea is aptly named the “bipolar seesaw” (Stocker

<sup>1</sup> Depending on the season, roughly the upper 100 meters of the oceans can be considered to be mixed by wind (Ruddiman 2013, Section 18.3).

and Johnsen 2003) and is confirmed by ice core observations. WAIS (2015) find that Antarctica cooled during Greenland warmings, with Greenland warming leading Antarctic cooling by  $218 \pm 92$  years. On the other hand, Greenland cooling leads Antarctic warming by  $208 \pm 96$  years – the DO events thus initiate in the Northern Hemisphere. Furthermore, since the DO events are seen in multiple ice core locations as well as marine cores, the  $\delta^{18}\text{O}$  signal likely represents a large scale event affecting the North Atlantic region (Grootes et al. 1993; NGRIP 2004).

The AMOC was operating at reduced intensity during GSs (Steffensen et al. 2008). The amount of water transported by the AMOC can be reduced disturbed by large influxes of fresh surface water (Lowe et al. 2013; Rahmstorf 2013).

One possible mechanism for alternating warm and cold periods over Greenland can thus be proposed; melting of large ice sheets in Greenland releases large amounts of fresh water into the North Atlantic, preventing deep water formation. The AMOC is reduced and transports less heat to the Northern Hemisphere (Lowe et al. 2013).

An explanation confined to the ocean is not sufficient though. (Steffensen et al. 2008) investigate the warmings at the beginning of the BA and end of YD using data from the NGRIP core, and report a decrease in dust content approximately 10 years *before* observing a change in  $\delta^{18}\text{O}$  – since the dust in Greenland is carried from Asian deserts (Section 5.1) this finding suggests that atmospheric circulation patterns over the Northern Hemisphere changed significantly in connection with DO events. This changing atmospheric pattern was likely a northward shift of the intertropical convergence zone (ITCZ) resulting in a wetting of Asian deserts by a more intense monsoon; this “was followed by a complete reorganization of the mid- to high-latitude atmospheric circulation almost from one year to the next” (Steffensen et al. 2008) and ultimately followed by a retreat of sea ice.

The following quote is from Alley et al. (2003):

“Systems exhibiting threshold behavior are familiar. For example, leaning slightly over the side of a canoe will cause only a small tilt, but leaning slightly more may roll you and the craft into the lake. [...] An abrupt change, of a canoe or the climate, requires a trigger, such as you leaning out of a canoe; an amplifier and globalizer, such as the friction between you and the canoe that causes the boat to flip with you; and a source of persistence, such as the resistance of the upside-down canoe to being flipped back over.”

Even though the causes of DO events are not fully understood at present (WAIS 2015), we can identify at least two positive feedbacks that serve as ‘persistence’. The ice-albedo feedback will cause a cooling in an already ice covered area by increasing surface reflectivity; conversely, bedrock exposed by melting will absorb more incoming solar radiation. As the THC is driven in large part by high latitude cooling (Rahmstorf 2013), a shift of the deep water formation areas to higher, colder latitudes will amplify the THC.

As ‘globalizers’ we can identify the northern shift of the ITCZ during Greenland warm periods as well as the strengthened AMOC, as the first strengthens the monsoons and the latter cools the Southern Hemisphere.

What is ultimately lacking is the ‘trigger’ – even if melt events trigger an AMOC shutdown, what triggers the melt event? At present, this ‘trigger’ mechanism is unknown, and not necessarily observable in ice core data (Lowe et al. 2013; Rahmstorf 2013; WAIS 2015).

### 1.3 Previous Research on Tipping Points

As the climate of the Earth has shifted between drastically different states over the course of its history, it is natural to ask if such large transitions are likely to happen again. Given the discussion of DO events above, one could also ask *how* such a transition may occur; will a given transition happen slowly or abruptly? Several authors put forward the idea that elements of Earth’s climate may be susceptible to *tipping* or abruptly switching between states:

“I reserve the term *critical transition* for the subclass of regime shifts that in models would correspond to shifts between alternative attractors. Those are the transitions in which a positive feedback pushes a runaway change to a contrasting state once a threshold is passed” (Scheffer 2009, p. 104).

The term “tipping element” is derived from the influential <sup>2</sup> paper by Lenton et al. (2008) which evaluates – by expert elicitation – large scale elements of the Earth’s climate system, ranging the Amazon rainforest to the West Antarctic ice sheet, and attempts to identify which elements are most “policy-relevant”.

#### 1.3.1 The Double Well Potential Model and EWS

As a conceptual model for a system capable of undergoing a critical transition, a double well potential model (Chapter 3) is often considered (eg. Scheffer et al. (2009), Livina et al. (2010), Ditlevsen and Johnsen (2010), and Cimadoribus et al. (2013). This is the simplest model with two states separated by a potential barrier (Kwasniok and Lohmann 2009).

This model will be investigated in detail in Section 3.3 and Chapter 4. Crucially, it is able to undergo a transition in either of two ways; 1) as a result of a bifurcation when a parameter  $p$  is varied or 2) by stochastically jumping from one state to the other. In the first case, it is sometimes possible to observe EWS before the transition happens, while in the latter case it is not.

The EWS one looks for are typically lag-1 autocorrelation, variance and detrended fluctuation analysis (DFA) exponent  $\alpha$ , each calculated from the time series in a sliding window.

DFA was introduced by Peng et al. (1994). Here one measures the *fluctuation function*  $F(s)$  as a function of window size  $s$  for a range of window sizes, and determine the scaling exponent  $\alpha$  such that  $F(s) \propto s^\alpha$ ;  $\alpha = 0.5$  for white noise and  $\alpha = 1.5$  for a random walk, and DFA thus measures the length of memory in the system (Livina and Lenton 2007).

---

<sup>2</sup>When searching [Web of Science](#) for the term “tipping point” on November 23, 2016 Lenton et al. (2008) was the second most cited paper with 845 citations; the most cited paper Hoegh-Guldberg et al. (2007) with 1740 citations specifically pertained to coral reefs. When searching for “tipping points” (plural) Scheffer et al. (2009) was the most cited paper with 871 citations, and Lenton et al. (2008) the second most cited.

The DFA method is advantageous to use when the dataset considered is non-stationary since detrending is built in to the method (Kantelhardt et al. 2001). However, it has been shown to be substantially more data consuming than computing the autocorrelation function (ACF) (Höll and Kantz 2015). Lag-1 autocorrelation and the DFA exponent measure memory in the system and thus *detects critical slowing down* (see Chapter 3 or eg. Scheffer et al. (2009)). In general, variance and lag-1 autocorrelation are expected to increase before a bifurcation (eg. Ditlevsen and Johnsen (2010)) although in some special cases the variance will not increase (Dakos et al. (2012b), see below).

The lag-1 autocorrelation can be calculated by fitting an autoregressive (AR) model of order 1, known as an AR(1) model, to the time series – AR model are described in Section 2.2.

A note on terminology: in the literature these quantities are sometimes called “indicators” and sometimes “propagators”; further, Livina and Lenton (2007) introduce a rescaling of the DFA exponent (see below) which they called the “DFA propagator”, symbolized with  $\zeta$ . I will use the term “indicator” exclusively, unless referring to the original DFA *exponent*  $\alpha$ .

### 1.3.2 Research on Time Series and Tipping Points

The main results concerning ice core data analysis from the articles discussed here in Section 1.3.2 are summarized in Table 1.1.

Held and Kleinen (2004) use a model of the AMOC and consider the leading empirical orthogonal function (EOF) (von Storch and Zwiers 2003, Chapter 13) of the Atlantic salinity field. The overturning strength is denoted  $q$  (in units of Sv) and the bifurcation parameter  $p$  is the freshwater flux into the North Atlantic. The object of interest is  $q(p)$  and the especially the critical value  $p_c$  where the AMOC experiences a shutdown. They note that in the small noise limit, the system may be approximated by a deterministic equilibrium solution stochastically perturbed by noise (representing “the weather”), and point out that for a dynamical system approaching a bifurcation, the smallest decay rate will vanish and the variance will increase.

Since the leading EOF is designed to capture the largest possible amount of variance, and because an increase in variance will accompany the vanishing rate, only the leading EOF of the Atlantic salinity field is studied; they name this method “degenerate fingerprinting”. By modeling the leading salinity EOF as an AR(1) process, they observe increasing lag-1 autocorrelation leading up to an AMOC shutdown.

Nes and Scheffer (2007) investigate six models of ecological systems, each represented by ordinary differential equations (ODEs). As the models approach a threshold, they observe critical slowing down in all models. They perform their analysis in one of two ways, depending on the system: either (for one-dimensional systems) by linearization of the equations, whereafter the real part of the dominant eigenvalue is used as an approximation of the recovery rate; or (for  $N$ -dimensional systems,  $N > 1$ ) by perturbing the system and investigating the resulting time series.

Nes and Scheffer (2007) point out that changes in – and not the absolute values of – the rate of recovery should be considered as the main object of interest, since two different systems may have vastly different natural rates of recovery.

Livina and Lenton (2007) study GISP2 paleo temperature data obtained from oxygen isotope ratios (Alley 2000) in the interval from 50 ka b2k to the present. They start by calculating the DFA exponent  $\alpha$  from a set of time series simulated with AR models, and proceed to determine an empirical relationship – a piecewise polynomial function – between  $\alpha$  and the lag-1 autocorrelation coefficient, thus yielding the DFA *indicator*  $\zeta$  (note that  $\zeta$  is called the “DFA propagator” in Livina and Lenton (2007)). When analyzing the GISP2 paleo temperature data they find a steady increase in  $\zeta$  from  $\sim 30$  ka b2k to  $\sim 12$  ka b2k which they interpret as anticipation of the warming at the end of the YD.

Dakos et al. (2008) use a range of climate proxies from past abrupt climatic changes and compute the lag-1 autocorrelation coefficient in sliding windows leading up to the transitions; this is done by fitting an AR(1) model in each window. They do not consider variance in the time series. Critical slowing down is found in all cases considered; most robustly for the end of Greenhouse Earth (34 Ma ago), the end of Glaciation I (17 ka b2k) (Dakos et al. 2008, supporting information) and the end of the YD. More moderate signs of critical slowing down was observed leading up to BA. The proxies considered for BA are GISP2 paleo temperature derived from oxygen isotopes (Alley 2000; Alley 2004) and for YD, grey scale data from a Cariaco Basin sediment core. Grey scale, or sediment reflectance, is proxy for surface productivity and wind strength (Hughen et al. 2000).

Dakos et al. (2008) point out that their analysis does not suggest any underlying mechanism, but do suggest that positive feedbacks in the system play a role.

Ditlevsen and Johnsen (2010) analyze the double well model capable of undergoing stochastic and bifurcation induced transitions, the latter resulting from slow variation of a control parameter. They show that variance *and* lag-1 autocorrelation will increase in time from the model in the bifurcation case; increases in both indicators should thus be detected simultaneously in data in order to conclude that a tipping point is reached. They analyze  $\delta^{18}\text{O}$  from NGRIP and find no EWS prior to DO events.

Kuehn (2011) demonstrates that *ensembles* of events should be considered whenever possible, as analyzing a single time series may give spurious results (cf. Kuehn (2011, Fig. 14) and Figure 4.1 in the present work).

Dakos et al. (2012b) show how the effect of noise on the state variable  $X_t$  has different effects than noise on a parameter  $p$ . In the latter case they take  $p$  to be a random variable with mean  $p^*$ . For a system described by a stochastic differential equation (SDE)  $dX_t = f(X_t, p)dt + \sigma dW_t$ , the effect is shown by expanding around a steady state  $(x^*, p^*)$  such that  $f(x^*, p^*) = 0$ . They derive analytical expressions for autocorrelation and variance in both cases (noise on  $X_t$ , noise on  $p$ ), and show that – depending on the form of  $\partial f/\partial p$  – situations are possible where variance will *decrease* gradually before the a bifurcation; immediately before the bifurcation, however, variance will still increase. Conversely, the expression for autocorrelation is the same in both cases.

The effect is illustrated in a model of logistic growth of a biomass under harvesting. Furthermore, Dakos et al. (2012b) demonstrate that a “slow” system – where the slowness may be the result of an approach to a bifurcation – subject to fast parameter variations will see a decrease in variance, simply be-

cause the system has insufficient time to adjust to the fast fluctuations. Again, the autocorrelation is unaffected by this effect.

Lenton et al. (2012a) investigate GRIP, GISP2 and NGRIP  $\delta^{18}\text{O}$  and  $[\text{Ca}^{2+}]$ . The time series are investigated from  $\sim 22.9$  to  $\sim 11.7$  ka b2k, a time span that includes the LGM, the BA warming and the warming at the end of the YD. They compute the variance, the lag-1 autocorrelation and the DFA indicator  $\zeta$  introduced by Livina and Lenton (2007).

They observe signs of critical slowing down in some of the series, but ultimately ascribe these results to inadequate detrending. As mentioned, Dakos et al. (2008) reported critical slowing down during leading up to the BA warming – no further evidence to support this is found in either GISP2  $[\text{Ca}^{2+}]$ , or GRIP and NGRIP  $\delta^{18}\text{O}$  when considering autocorrelation or  $\zeta$ . Similarly,

“[...] results from Greenland ice cores do not provide convincing support for the hypothesis that the climate approached a bifurcation at the end of the Younger Dryas” (Lenton et al. 2012a).

Lenton et al. (2012b) analyze GISP2  $\delta^{18}\text{O}$  and Cariaco Basin grey scale data, as well as Antarctic ice core data and model output from AMOC simulations. Comparing the result of autocorrelation and the DFA indicator  $\zeta$ , robust early warnings are found before the end of the YD; conversely, only a weak trend is found before the BA transition.

Following the now established trend of analyzing NGRIP  $\delta^{18}\text{O}$  data, Cimatoribus et al. (2013) first perform a phase space reconstruction by delay embedding of the time series (eg. Kantz and Schreiber (2000)) and show that the time series before 22 ka b2k exhibits a bimodal distribution; after 22 ka b2k the distribution is unimodal. Additionally, they analyze an ensemble of 15 DO events and compute the variance and lag-1 autocorrelation as well as the DFA *exponent*  $\alpha$ . Averaging these quantities over the whole ensemble shows a “moderate but significant” increase for all three indicators.

A fresh approach is taken by Nikolaou et al. (2014) who investigate GISP2 and NGRIP  $\delta^{18}\text{O}$  data using “*a time series segmentation algorithm combining a clustering technique and a genetic algorithm*”. This method starts with a random segmentation, or partitioning, of the time series. Six different statistics (variance, skewness, kurtosis, slope of linear fit, mean squared error of the linear fit and lag-1 autocorrelation coefficient) are computed for each segment, allowing the segments to be represented as points in a 6-dimensional feature space. The clustering algorithm partitions the segments into clusters, and the *fitness function*  $F$  is evaluated; Nikolaou et al. (2014) use the fitness function  $F = \left(1/N \sum_{i=1}^N (d_i)^2\right)^{-1}$  where  $N$  is the number of segments and  $d_i$  is the distance in feature space from the segment to the nearest cluster centroid. The genetic algorithm (GA) now is allowed to alter the time series segmentation (eg. cutting the time series in different places) with the objective of maximizing  $F$ .

Using this method – that assumes no prior knowledge of the transitions – Nikolaou et al. (2014) detect EWS  $> 70\%$  of the times (the GA is run several times with different random seeds) for half of the 12 considered DO events, and less robustly for the remaining 6 DO events. The main distinguishing features of the segments showing EWS are found to be increased variance, autocorrelation and non-linearity (as measured by the deviation from the linear fit).

Rypdal (2016) investigate  $\delta^{18}\text{O}$  from NGRIP and reports two findings. The first is an increase in mean ensemble variance leading up to transitions from GS to GI, thus supporting the findings of Cimatoribus et al. (2013). The second result is obtained by using the continuous wavelet transform (CWT). Rypdal (2016) focuses on the wavelet coefficients corresponding to high-frequency fluctuations; by considering the standard deviation of this set of coefficients computed in sliding windows, EWS are found for a number of DO events.

### 1.3.3 *B-Tipping, N-Tipping & R-Tipping*

Above we have considered two types of critical transitions, namely those caused by a bifurcation and those caused by a noise induced transition. Although this topic is not investigated further here we mention another type of tipping mechanism, namely *R-tipping* (Ashwin et al. 2012) where the tipping mechanism depends on the *rate* of change of a parameter.

Luke and Cox (2011) investigate the ominously sounding “compost-bomb instability” in a model of soil carbon and atmospheric temperature. Soil carbon in the form of peat deposits are broken down by microbes in a process that depends on the soil temperature: a higher soil temperature increases the microbial carbon breakdown; the soil temperature in turn depends on the atmospheric temperature. Further, the microbial breakdown of carbon itself produces heat and so the system contains a positive feedback (Luke and Cox 2011, Figure 1). The study concludes that there is a critical rate  $r_c$  of global temperature rise above which the carbon-microbe system may run away leading to the compost-bomb instability. This release of carbon into the atmosphere in the form of  $\text{CO}_2$  may then further increase global warming (Luke and Cox 2011; Wieczorek et al. 2011).

Wieczorek et al. (2011) put these findings on a rigorous footing and analytically derive the critical rate  $r_c$ . Ashwin et al. (2012) introduces the following terminology for the three different types of tipping points encountered so far:

- *B-tipping* where a changing parameter causes a bifurcation,
- *N-tipping* where external noise pushes the system over a tipping threshold, and
- *R-tipping* where the rate of change of a control parameter becomes too large for the system to “track” (Ashwin et al. 2012) the stable solution.

Furthermore, Ashwin et al. (2012) investigate a zero-dimensional global energy balance model and show that – for different parameter ranges – the system exhibits all three types of tipping mechanisms (Ashwin et al. 2012, Figure 7 and Table 1).

The study ends by posing as an open question whether EWS for a system undergoing *R-tipping* may be found, as *R-tipping* does not imply a change in stability of the system (Ashwin et al. 2012, p. 1182). This question about EWS for *R-tipping* systems is investigated by Ritchie and Sieber (2016) who study a one-dimensional system and conclude that in the small noise limit, both increasing variance and lag-1 autocorrelation can be expected.

Study	Subject	Data	Methods	EWS found?
Rypdal (2016)	DO events & YD	NGRIP $\delta^{18}\text{O}$	CWT & Var	Increasing $\text{Var}^*$ , high-frequency fluctuations <sup>†</sup>
Nikolaou et al. (2014)	DO events	GISP2 & NGRIP $\delta^{18}\text{O}$	Time series segmentation, GA	$\text{Var}^\dagger$ , $\text{AC}^\dagger$
Cimatoribus et al. (2013)	DO events	NGRIP $\delta^{18}\text{O}$	Var, AC, DFA exponent $\alpha$	Deviation from linear <sup>†</sup> Increasing $\text{Var}^*$ , $\text{AC}^*$ and $\alpha^*$
Lenton et al. (2012b)	Several, including BA & YD	BA: GISP2 $\delta^{18}\text{O}$ YD: Cariaco greyscale	Var, AC DFA indicator $\zeta$	BA: inconclusive YD: Increasing $\text{AC}^\dagger$ and $\zeta^\dagger$
Lenton et al. (2012a)	LGM, BA, YD	GRIP, GISP2 & NGRIP $\delta^{18}\text{O}$ & $[\text{Ca}^{2+}]$	Var, AC & DFA indicator	No (partly inconclusive)
Ditlevsen and Johnsen (2010)	DO events	NGRIP $\delta^{18}\text{O}$	Var, AC	No
Dakos et al. (2008)	Several, including BA & YD	BA: GISP2 temperature YD: Cariaco greyscale	AC	Increasing $\text{AC}^\dagger$
Livina and Lenton (2007)	End of YD	GISP2 temperature	DFA indicator $\zeta$	Increasing $\zeta^\dagger$

**Table 1.1 | Previous studies of early warnings.** See text in Section 1.3.2 for a detailed description of the studies. **AC:** autocorrelation, **BA:** Bølling-Allerød, **CWT:** continuous wavelet transform, **DFA:** detrended fluctuation analysis, **DO:** Dansgaard-Oeschger, **EWS:** early warning signals, **GA:** genetic algorithm, **LGM:** Last Glacial Maximum, **Var:** variance, **YD:** Younger Dryas. **GRIP, GISP2 & NGRIP:** ice cores, see Figure 1.1. \*: EWS found in ensembles. †: EWS found in individual time series (not necessarily all time series considered).

### 1.3.4 Further Research

Excellent reviews tipping point research can be found in Scheffer et al. (2009), Thompson and Sieber (2010), Thompson and Sieber (2011), Lenton (2011), Scheffer et al. (2012), Dakos et al. (2012a), and Thomas (2016).

Notably absent from the discussion of paleoclimatic time series analysis presented here is spectral analysis (eg. Yiou et al. (1997) and Ditlevsen et al. (2005)), the topic of potential analysis (eg. Kwasniok and Lohmann (2009), Livina et al. (2010), and Livina et al. (2012)) and the application of nonlinear oscillators as conceptual climate models (eg. Crucifix (2012), Kwasniok and Lohmann (2012), and Ashwin and Ditlevsen (2015)).

## 1.4 Applications of the Transfer Operator

The transfer operator approach to analyzing dynamical systems is probabilistic (Dellnitz et al. 2009) rather than geometric (eg. in terms of using bifurcation diagrams). The transfer operator  $\mathcal{L}_\tau$  acts on probability distributions that are defined on the on the state space  $\Omega$  of the dynamical system under investigation.

We present four studies below that share similarities.  $\mathcal{L}_\tau : L^1 \rightarrow L^1$  is approximated by a transition matrix  $P_{ij}(\tau)$ .  $P_{ij}(\tau)$  in turn is calculated by partitioning  $\Omega$  into  $N$  boxes  $\{B_i\}_{i=1}^N$ . After observing trajectories  $x(t)$  of the system, the  $ij$ 'th entry of  $P_{ij}(\tau)$  is thus the observed probability of  $x(t)$  occupying the box  $B_i$  and  $x(t + \tau)$  occupying the box  $B_j$ . We investigate this in greater detail in Chapter 2 – here we give a few examples of applications.

The aim of Dellnitz et al. (2009) is to identify the Ross and Weddell gyres – large scale observable structures in the Southern Ocean – in data output from an ocean model. One of the model outputs is the monthly averaged velocity field  $\mathbf{v}(\mathbf{x}; t)$  as a function of month  $t$ . By using  $\mathbf{v}(\mathbf{x}; t)$  to integrate a large number of trajectories, Dellnitz et al. (2009) search for *almost-invariant sets*, sets of the state space that change very little under the flow; these sets are successfully identified with the Ross and Weddell gyres.

Chekroun et al. (2014) simulate the ENSO with an intermediate complexity model forced by seasonal variations while varying a central model parameter. In particular, they study the spectral gap  $\gamma = 1 - |\lambda_2|$  where  $\lambda_2$  is the subdominant eigenvalue (second largest in absolute magnitude) of  $P_{ij}(\tau)$ .  $\gamma$  can be related to the memory of the system (see Section 2.7.2); Chekroun et al. (2014) find that regimes with small gaps correspond to regimes of long memory, where autocorrelation decays slowly.

A key contribution of Chekroun et al. (2014) is a theorem relating transition probabilities in the state space  $\Omega \in \mathbb{R}^n$  to transition probabilities in a reduced state space  $Y \in \mathbb{R}^m$  with  $m < n$  through a continuous observation function  $h : \Omega \rightarrow Y$  (Section 2.8.1).

The theorem by Chekroun et al. (2014) is exploited by Tantet et al. (2015a) who investigate output from an atmospheric model. In this model, circulation patterns alternate between two regimes, *zonal* and *blocking*. The system is observed through the first and third leading EOFs; thus the EOF decomposition constitutes the observation function  $h$ .

After a clear theoretical exposition Tantet et al. (2015a) use the transfer operator to show the presence of time scale separation in the system, uncovering meta-stable regimes corresponding to the two system states. Finally, the

transition matrices  $P_{ij}(\tau)$  are used to construct an early warning system for transitions between the two regimes.

We end this section by mentioning Tantet et al. (2015b) who use a climate model capable of switching from a present day-like state to a Snowball Earth state. The critical parameter in this model is the solar constant  $S$  with units  $W/m^2$ . For large values of  $S$  the Snowball Earth state vanishes, and for small  $S$ -values the warm state vanishes. For intermediate  $S$ -values the two states coexist, resulting in a hysteresis loop.

Tantet et al. (2015b) start the model in present day conditions and decrease  $S$ . They approximate  $\mathcal{L}_\tau$  by  $P_{ij}(\tau)$  from two model outputs, namely fraction of sea ice cover in the Northern Hemisphere and mean surface temperature in a belt around the Equator. Leading up to a transition from the warm state to the snowball state they observe critical slowing down through a decreasing spectral gap.

Crucially, as their model is chaotic Tantet et al. (2015b) do not attribute the slowing down to an approaching bifurcation, but rather to an “attractor crisis” – the attractor corresponding to the warm state is destroyed after the crisis.

## 1.5 Outline

Chapter 2 presents the analytical framework. In Sections 2.1 to 2.4 we recall some tools from time series analysis with a focus on autoregressive processes and the Ornstein-Uhlenbeck (OU) process, as these lay the groundwork for the study of EWS and the work presented in Mikkelsen et al. (2017). The transfer operator and methods of its approximation are introduced in Sections 2.5 to 2.11.

Chapter 3 list some types of bifurcations commonly studied in the context of tipping points. We motivate and introduce the double well potential model and derive expressions for the observed variance and autocorrelation when approaching a bifurcation.

In Chapter 4 we apply the methods from Chapter 2 to the model from Chapter 3 and verify that – for the conceptual model – we can detect EWS by using the transfer operator framework.

Chapter 5 is concerned with analysis of data from the NGRIP ice core. We introduce and interpret the proxies  $\delta^{18}O$ ,  $[Ca^{2+}]$ ,  $[Na^+]$  and  $[NH_4^+]$  in Section 5.1 and detail our methodology in Section 5.2. We analyze the NGRIP data in Sections 5.3 and 5.4.

In Chapter 6 we summarize Mikkelsen et al. (2017) and give a suggestion for future work building on the results we have obtained; Chapter 7 provides a general conclusion and discussion of the work presented in this thesis. As abbreviations are prolific in this work, Appendix A lists the ones we use most often; Appendix B lists the computational tools we have used and developed, and points the more intrepid reader to [Bitbucket](#) where the code can be obtained.

Finally the article Mikkelsen et al. (2017) is appended in Appendix D and supplementing information in Appendix E; Appendix C contains the wording of the co-author statements that are required by the University of Copenhagen.



## 2 Time Series Analysis and Modeling

### 2.1 Time Series From Dynamical Systems

A continuous dynamical system  $S_t : \Omega \times \mathbb{R} \rightarrow \Omega$  on a state space  $\Omega$  is a rule that for all  $t \in \mathbb{R}$  maps  $\Omega$  on to itself; furthermore, (Lasota and Mackey 1994, Chapter 7):

- $S_0(z) = z \forall z \in \Omega$ ,
- $S_s(S_t(z)) = S_{s+t}(z) \forall z \in \Omega, \forall t, s \in \mathbb{R}$ ,
- The mapping  $(t, z) \mapsto S_t(z)$  is continuous.

For applications arising in physics the rule  $S_t$  will often be a system of ordinary differential equations on a finite dimensional state space (Kantz and Schreiber 2000), and we may think of  $t$  as *time* and write

$$\frac{dz}{dt} := \dot{z} = f(z). \quad (2.1.1)$$

Let  $z_0 = z(t=0)$  and  $z_t = S_t(z_0)$ . In this way  $S_t$  is the flow generated by Equation (2.1.1) (Kantz and Schreiber 2000) such that

$$\frac{d}{dt} S_t(z) = f(z(t)). \quad (2.1.2)$$

If we during an experiment observe the system Equation (2.1.1) at times  $t_n = n\Delta t, n = 0, 1, \dots$  through some observation function  $h$  we end up with a time series (Kantz and Schreiber 2000, p. 35)

$$\begin{aligned} x_0 &= x(0) = h(z(0)) \\ x_1 &= x(\Delta t) = h(z(\Delta t)) \\ &\dots \end{aligned} \quad (2.1.3)$$

Measurements of a physical system will invariably contain uncertainties (Taylor 1982); maybe our system itself may also contain elements that we choose to model as noise because they are uninteresting for our purposes (Ditlevsen 2004); even carrying out computer simulations will contain round-off error that can be thought of as noise (Ruelle 1986b). In all these cases our time series  $\{x_n\}, n = 0, 1, \dots$  can be thought of as realizations of a stochastic process  $\{X_n\}, n = 0, 1, \dots$  (Madsen 2008; Kantz and Schreiber 2000).

Let  $X$  be a discrete stochastic variable and  $P(X = x)$  the probability that  $X$  assumes the value  $x$ . For discrete  $X$  the expectation of is  $X$

$$E[X] = \sum_x xP(X = x); \quad (2.1.4)$$

for a continuous variable with continuous density function  $f_X$  the expectation is

$$E[X] = \int_{-\infty}^{\infty} xf_X(x) dx, \quad (2.1.5)$$

and in both cases

$$\text{Var}[X] = E[(X - E[X])^2] = E[X^2] - (E[X])^2 \quad (2.1.6)$$

defines the variance of  $X$ .

## 2.2 Autoregressive Processes

When modeling a time series  $\{x_n\}$  it is convenient to introduce backward shift operator  $B$  defined as follows (Box et al. 2008; Madsen 2008):

$$\begin{aligned} Bx_n &= x_{n-1}, \\ B^2x_n &= x_{n-2}, \\ &\dots \end{aligned} \quad (2.2.1)$$

so

$$(1 - B)x_n = x_n - x_{n-1}. \quad (2.2.2)$$

Let  $\{\epsilon_n\}$  denote a series of independent, Gaussian distributed random variables with mean  $\mu$  and variance  $\sigma^2$ , ie.  $\epsilon_n \sim \mathcal{N}(\mu, \sigma^2)$ . AR of order  $p$ , or AR( $p$ ) processes, have the form

$$X_n = \phi_1 X_{n-1} + \dots + \phi_p X_{n-p} + \epsilon_n. \quad (2.2.3)$$

Using the backward shift operator this can be written as

$$(1 - \phi_1 B - \dots - \phi_p B^p) X_n = \epsilon_n \quad (2.2.4)$$

or

$$\phi(B)X_n = \epsilon_n \quad (2.2.5)$$

where  $\phi$  is seen as a polynomial in  $B$ . An AR model is stable if all the complex roots of  $\phi(B)$  lie outside the unit circle; thus the AR(1) model is stable if  $|\phi_1| < 1$  (Box et al. 2008, p. 10). Next we define a moving average (MA) model of order  $q$ ,

$$X_n = \epsilon_n + \theta_1 \epsilon_{n-1} + \dots + \theta_q \epsilon_{n-q} \quad (2.2.6)$$

or using the backward shift operator,

$$\begin{aligned} X_n &= \theta(B)\epsilon_n \\ &= (1 + \theta_1 B + \dots + \theta_q B^q) \epsilon_n. \end{aligned} \quad (2.2.7)$$

For completeness we mention integrated models of order  $d$  as

$$(1 - B)^d X_n = \epsilon_n. \quad (2.2.8)$$

Combining this leads to the ARIMA( $p, d, q$ ) model (Madsen 2008):

$$\phi(B)(1 - B)^d X_n = \theta(B)\epsilon_n. \quad (2.2.9)$$

Note that the process

$$(1 - B)X_n = \epsilon_n \quad (2.2.10)$$

or

$$X_n = X_{n-1} + \epsilon_n \quad (2.2.11)$$

is the random walk (Madsen 2008, p. 131) which has non-constant variance (Box et al. 2008, p. 119) and so is non-stationary.

Large physical system such as climate models contain “fast” and “slow” subsystems (Ditlevsen 2004). It was shown by Hasselmann (1976) that this type of time scale separation naturally leads to modeling the system as an AR(1)-process (Mudelsee 2010) or, equivalently, the Ornstein-Uhlenbeck (OU) process.

## 2.3 Stochastic Differential Equations

Since SDEs and stochastic processes will play a substantial role in this work we will here review some basic concepts pertaining to analytical and numerical solutions. For extensive reviews of analytical tools see eg. Gardiner (2009) and Øksendal (2013) and for numerical solutions eg. Kloeden and Platen (1995) and Higham (2001).

### 2.3.1 The Wiener Process

The Wiener process – or Brownian motion –  $\{W_t, t \geq 0\}$  has continuous sample paths with stationary, independent increments satisfying the following properties (Dijkstra 2013, p. 40):

$$\begin{aligned} W_0 &= 0, \\ W_{t+s} - W_t &\sim \mathcal{N}(0, s), \quad s > 0, \\ W_t &\sim \mathcal{N}(0, t). \end{aligned} \quad (2.3.1)$$

### 2.3.2 Itô Processes

Stochastic calculus arises from the desire to integrate processes of the form (Øksendal 2013)

$$\frac{dX}{dt} = f(x) + \text{”noise”}. \quad (2.3.2)$$

A possibility is to write Equation (2.3.2) in the form

$$dX_t = u(X_t, t)dt + v(X_t, t)dW_t \quad (2.3.3)$$

or, equivalently,

$$X_t = X_0 + \int_0^t u(X_s, s)ds + \int_0^t v(X_s, s)dW_s \quad (2.3.4)$$

where  $W_t$  represents the Wiener process. One way to interpret the last term in Equation (2.3.4) is as an Itô integral, which is the interpretation we will use. Equation (2.3.4) is then also called an Itô process. Chapters 3 and 4 in Øksendal (2013) contain a thorough introduction to this material as well as to the alternative Stratonovich calculus for SDEs which we will not explore further here.

### 2.3.3 Itô's Lemma

To solve integrals like Equation (2.3.4) the following can be very useful:

**Theorem 2.1** (Itô's lemma, (Øksendal 2013)). If  $X_t$  is an Itô process and  $g(x, t) \in C^2$ , then  $Y_t = g(X_t, t)$  is also an Itô process and

$$dY_t = \frac{\partial g}{\partial t}(X_t, t)dt + \frac{\partial g}{\partial x}(X_t, t)dX_t + \frac{1}{2} \frac{\partial^2 g}{\partial x^2}(X_t, t) \cdot (dX_t)^2. \quad (2.3.5)$$

Furthermore, the terms in  $(dX_t)^2$  are calculated according to the rules

$$\begin{aligned} dt \cdot dt &= dW_t \cdot dt = 0, \\ (dW_t)^2 &= dt. \end{aligned} \quad (2.3.6)$$

△

**Theorem 2.2** (The Itô Isometry, (Øksendal 2013)). Let

$$f : \Omega \times [0, \infty) \rightarrow \mathbb{R} \quad (2.3.7)$$

where  $\Omega$  is the state space and let  $f$  satisfy certain measurability conditions (Øksendal 2013, p. 25); furthermore we demand that

$$\mathbb{E} \left[ \int_S^T f^2(X_t, t) dt \right] < \infty. \quad (2.3.8)$$

Then

$$\mathbb{E} \left[ \left( \int_S^T f(X_t, t) dW_t \right)^2 \right] = \mathbb{E} \left[ \int_S^T f^2(X_t, t) dt \right]. \quad (2.3.9)$$

△

The following properties of the Itô integral will be needed in Example 2.3; for the same class of functions as in Theorem 2.2 the following hold for  $0 \leq S < U < T$  (Øksendal 2013, Theorem 3.2.1, i) & iii):

$$\int_S^T f dW_t = \int_S^U f dW_t + \int_U^T f dW_t, \quad (2.3.10)$$

and

$$\mathbb{E} \left[ \int_S^T f dW_t \right] = 0. \quad (2.3.11)$$

We will make extensive use of the Ornstein-Uhlenbeck process in Chapters 3 and 4 where we investigate the increase in variance and autocorrelation before a tipping point. The following example is rather lengthy but represents a solid foundation from which to understand these results.

**Example 2.3** (Mean, variance and autocorrelation of the Ornstein-Uhlenbeck process, (Horsthemke and Lefever 2006; Ditlevsen 2008; Gardiner 2009)). Let  $X_t$  be the OU process. Then  $dX_t$  satisfies

$$dX_t = -\alpha X_t dt + \sigma dW_t \quad (2.3.12)$$

with initial condition  $X_{t=0} = X_0 = 0$ . To solve Equation (2.3.12) using Itô's lemma we use the standard  $y = g(x, t) = xe^{\alpha t}$  and note that  $dY_t$  is given by Equation (2.3.5):

$$dY_t = X_t \cdot \alpha e^{\alpha t} dt + e^{\alpha t} \cdot dX_t. \quad (2.3.13)$$

We plug in our expression for  $dX_t$ :

$$\begin{aligned} dY_t &= X_t \cdot \alpha e^{\alpha t} dt + e^{\alpha t} (-\alpha X_t dt + \sigma dW_t) \\ &= e^{\alpha t} (\alpha X_t dt - \alpha X_t dt + \sigma dW_t) \\ &= \sigma e^{\alpha t} dW_t. \end{aligned} \quad (2.3.14)$$

Now we have an expression for  $Y_t$ ; according to Equation (2.3.4)

$$Y_t = Y_0 + \sigma \int_0^t e^{\alpha s} dW_s. \quad (2.3.15)$$

We substitute  $X_t$ ; since  $Y_t = X_t e^{\alpha t}$  we have  $X_t = Y_t e^{-\alpha t}$

$$\begin{aligned} X_t &= e^{-\alpha t} \left( Y_0 + \sigma \int_0^t e^{\alpha s} dW_s \right) \\ &= e^{-\alpha t} X_0 + \sigma \int_0^t e^{-\alpha(t-s)} dW_s. \end{aligned} \quad (2.3.16)$$

We evaluate the expectation of Equation (2.3.16)

$$\begin{aligned} \mathbb{E}[X_t] &= \mathbb{E}[e^{-\alpha t} X_0] + \mathbb{E} \left[ \sigma \int_0^t e^{-\alpha(t-s)} dW_s \right] \\ &= e^{-\alpha t} X_0 = 0. \end{aligned} \quad (2.3.17)$$

where we used Equation (2.3.11). Next we evaluate the variance of Equation (2.3.16):

$$\begin{aligned} \text{Var}[X_t] &= \mathbb{E}[(X_t - \mathbb{E}[X_t])^2] \\ &= \mathbb{E} \left[ \sigma^2 \left( \int_0^t e^{-\alpha(t-s)} dW_s \right)^2 \right]. \end{aligned} \quad (2.3.18)$$

By Theorem 2.2

$$\left( \int_0^t e^{-\alpha(t-s)} dW_s \right)^2 = \int_0^t e^{-2\alpha(t-s)} ds \quad (2.3.19)$$

so Equation (2.3.18) reads

$$\text{Var}[X_t] = \sigma^2 \int_0^t e^{-2\alpha(t-s)} ds = \sigma^2 \frac{1 - e^{-2\alpha t}}{2\alpha}, \quad (2.3.20)$$

or, for large times  $t$

$$\text{Var}[X_t] \approx \frac{\sigma^2}{2\alpha}. \quad (2.3.21)$$

For the autocovariance  $\text{E}[X_{t_1}X_{t_2}]$  we use Equation (2.3.16): such that

$$\begin{aligned} \text{E}[X_{t_1}X_{t_2}] &= \text{E}\left[\sigma \int_0^{t_1} e^{-\alpha(t_1-u)} dW_u \times \sigma \int_0^{t_2} e^{-\alpha(t_2-v)} dW_v\right] \\ &= \sigma^2 e^{-\alpha(t_1+t_2)} \text{E}\left[\int_0^{t_1} e^{\alpha u} dW_u \times \int_0^{t_2} e^{\alpha v} dW_v\right]. \end{aligned} \quad (2.3.22)$$

The integrals in Equation (2.3.22) are then split into two parts (Horsthemke and Lefever 2006, pp. 49–53). Assume that  $t_1 < t_2$ :

$$\begin{aligned} \text{E}[X_{t_1}X_{t_2}] &= \sigma^2 e^{-\alpha(t_1+t_2)} \text{E}\left[\int_0^{t_1} e^{\alpha u} dW_u \times \int_0^{t_1} e^{\alpha v} dW_v\right] \\ &\quad + \sigma^2 e^{-\alpha(t_1+t_2)} \text{E}\left[\int_0^{t_1} e^{\alpha u} dW_u \times \int_{t_1}^{t_2} e^{\alpha v} dW_v\right] \\ &= \sigma^2 e^{-\alpha(t_1+t_2)} \text{E}\left[\left(\int_0^{t_1} e^{\alpha u} dW_u\right)^2\right] \\ &\quad + \sigma^2 e^{-\alpha(t_1+t_2)} \text{E}\left[\int_0^{t_1} e^{\alpha u} dW_u\right] \times \text{E}\left[\int_{t_1}^{t_2} e^{\alpha v} dW_v\right] \\ &= \sigma^2 e^{-\alpha(t_1+t_2)} \int_0^{t_1} (e^{\alpha u})^2 du + 0. \end{aligned} \quad (2.3.23)$$

We have split the expectation of the two integrals in the fourth line since the increments at times  $t < t_1$  and  $t > t_1$  are uncorrelated (Section 2.3.1), and applied Equation (2.3.11); the last line uses the Itô isometry (Theorem 2.2). We evaluate the last integral in Equation (2.3.23); since the choice  $t_1 < t_2$  was arbitrary:

$$\text{E}[X_{t_1}X_{t_2}] = \frac{\sigma^2}{2\alpha} e^{-\alpha(t_1+t_2)} \left(e^{2\alpha \min(t_1, t_2)} - 1\right), \quad (2.3.24)$$

or

$$\text{E}[X_{t_1}X_{t_2}] = \frac{\sigma^2}{2\alpha} \left(e^{-\alpha|t_1-t_2|} - e^{-\alpha(t_1+t_2)}\right). \quad (2.3.25)$$

Let  $\tau > 0$  be a fixed time interval and consider  $\text{E}[X_t X_{t+\tau}]$ . We get for large times  $t$

$$\text{E}[X_t X_{t+\tau}] \approx \frac{\sigma^2}{2\alpha} e^{-\alpha\tau} \quad (2.3.26)$$

and, dividing the autocovariance with the variance (Equation (2.3.21)) we obtain the autocorrelation  $C(\tau)$  (Madsen 2008, p. 130)

$$C(\tau) \approx e^{-\alpha\tau}. \quad (2.3.27)$$

△

### 2.3.4 The Euler-Maryuama Scheme

Let  $\dot{x}$  be given by a function  $f(x) = \dot{x}$ . We wish to solve this numerically at times  $t_0, t_1, \dots, t_k, \dots$  to obtain approximate solutions  $x_k$  at times  $t_k$ . The Euler scheme or Euler's method for solving ordinary differential equations is (Heath 2005)

$$x_{k+1} = x_k + f(x_k, t_k)\Delta t_k \quad (2.3.28)$$

where  $\Delta t_k = t_{k+1} - t_k$  is some small time step. This method uses the definition of the differential directly and is thus very illustrative; however for some cases it may be insufficient (Hairer et al. 2008; Hairer and Wanner 2010).

Assume we instead of  $\frac{dx}{dt} = f(x)$  have an SDE of the form Equation (2.3.3)

$$dX_t = u(X_t, t)dt + v(X_t, t)dW_t \quad (2.3.29)$$

and wish to approximate a solution  $X_k$ . Euler's method shows us how to solve the deterministic part coming from  $u(X_t, t)$  - if we add a stochastic term to Equation (2.3.28) we get

$$X_{k+1} = u(X_k, t_k)\Delta t_k + v(X_k, t_k)\Delta W_k. \quad (2.3.30)$$

The question is, how large should  $\Delta W_k$  be? Well, this is given by Equation (2.3.1) that tells us that the variance of  $W(t + \Delta t) - W(t)$  is proportional to  $\Delta t$  - it follows that if we for every time step  $k$  draw a random Gaussian variate  $N_k \sim \mathcal{N}(0, 1)$  we can write Equation (2.3.30) as

$$X_{k+1} = u(X_k, t_k)\Delta t_k + v(X_k, t_k)\sqrt{\Delta t}N_k; \quad (2.3.31)$$

Equation (2.3.31) is known as the Euler-Maryuama (EM) method (Higham 2001).

There exists an abundance of schemes for solving SDEs numerically (Kloeden and Platen 1995). We will use the EM method due to its simplicity and its widespread use in literature (eg. Kuehn (2011), Kuehn (2012), Kwasiok and Lohmann (2012), Cimatoribus et al. (2013), and Mitsui and Crucifix (2016)) for solving problems such as the ones presented in Chapter 4.

## 2.4 Detrending

In Chapter 4 we will analyze time series from a a system undergoing a bifurcation. This timeseries will be seen by inspection to have an obvious trend. Livina et al. (2011) suggest removing such obvious trends before performing analyses while Kuehn (2012) shows that linear detrending yields satisfactory results when analysing data from the Stommel (1961) box model with stochastic forcing (Cessi 1994); further Box et al. (2008, pp. 285–286) explore the possibility of linearly detrending data with a deterministic linear trend before fitting an AR(1)-model.

Detrending is challenging however (Dakos et al. 2008). Rypdal (2016) points out that simply detrending data may leave low-frequency variability in the data that obscures the high-frequency early warning signals.

When estimating autocorrelation and variance in Chapter 4 I will use linear detrending based on the mentioned results from Kuehn (2012).

## 2.5 The Transfer Operator

The remainder of this chapter is devoted to introducing the transfer operator or Perron-Frobenius (PF) operator and illustrate how this can be used to study the evolution of densities in state space, specifically the decay of correlations between observables.

This subject is rich and contains a large number of results that we do not hope to cover completely; we merely aim to justify the use of the PF operator for time series analysis. We provide a summary of this topic and its application to time series analysis in Section 2.11.

### 2.5.1 Semidynamical Systems

We define a semi-dynamical system  $\{S_t\}_{t \geq 0}$  as a family of maps  $S_t : \Omega \rightarrow \Omega$ ,  $t \in \mathbb{R}_+$  acting on points  $x \in \Omega$  (Lasota and Mackey 1994, Chapter 7):

1.  $S_0(x) = x$ ,
2.  $S_t(S_s(x)) = S_{t+s}(x)$  for  $t, s \in \mathbb{R}^+$ ,
3. The mapping  $(t, x) \rightarrow S_t(x)$  from  $\mathbb{R}_+ \times \Omega$  into  $\Omega$  is continuous.

For a dynamical system  $\{T_t\}_{t \in \mathbb{R}}$  invertibility naturally follows: simply let  $t > 0$  and observe that  $T_{-t}(T_t(x)) = T_{t-t}(x) = T_0(x) = x$ . On the other hand a semidynamical system is not invertible (Lasota and Mackey 1994, p. 195) since  $t$  is restricted to lie in  $\mathbb{R}_+$ .

A semidynamical system  $\{S_t\}_{t \geq 0}$  however may still arise from a system of ordinary differential equations  $\dot{x} = f(x)$  simply by restricting our attention to  $S_t(x_0) = x(t)$  for nonnegative times  $t \geq 0$  with  $x_0 = x(t=0)$  (Lasota and Mackey 1994, p. 210). The reason for this seemingly artificial restricting our attention to semidynamical systems should become clear in Section 2.6.3 where a result from the theory of semigroups is introduced.

I find that some of the results presented in the remainder of this chapter are best described in continuous time (represented by  $s, t, \tau$ ) and some in discrete time (represented by  $i, n, k$ ). We will distinguish flows  $S_t$  (continuous time  $t$ ) from maps  $S^n$  (discrete time  $n$ ) using subscript for the former and superscript for the latter. I hope that this is not too great a concern to the reader; for any fixed time  $t$  the definitions of the Koopman and Perron-Frobenius operator are the same in continuous and discrete time, and the interpretations of eg. mixing (Definition 2.7) and ergodicity (Definition 2.8) are interpreted the same way (Lasota and Mackey 1994, Chapter 7).

### 2.5.2 The Perron-Frobenius and Koopman Operators

Let  $\Omega$  be a given set,  $\Sigma$  a  $\sigma$ -algebra on  $\Omega$  and  $\mu$  a measure so that  $(\Omega, \Sigma, \mu)$  is a measure space. Further let  $L^1$  denote the space of integrable function,  $L^\infty$  the space of essentially bounded functions and for  $f \in L^1(\Omega)$ ,  $g \in L^\infty(\Omega)$ ,  $f, g : \Omega \rightarrow \mathbb{R}$  let

$$\langle f, g \rangle = \int_{\Omega} f(x)g(x) \mu(dx) = \int_{\Omega} fg \, d\mu \quad (2.5.1)$$

define the scalar product of  $f$  and  $g$ .

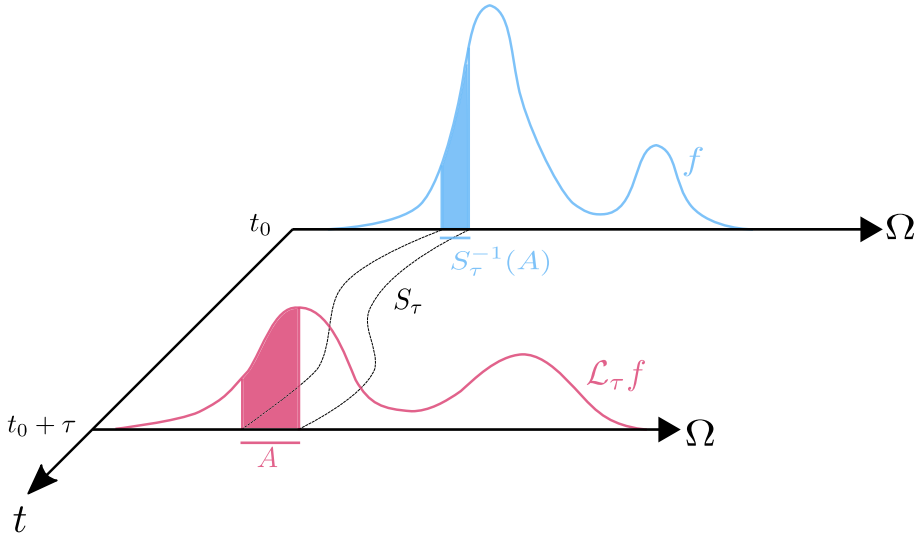


**Figure 2.1 | Illustration of the action of the Perron-Frobenius operator.** The observable  $f$  is defined on the same space  $\Omega$  as the flow  $S_\tau$ .  $S_\tau$  transforms a set  $A$ , and  $\mathcal{L}_\tau$  propagates  $f$  correspondingly (Equation (2.5.2)). Compare with Figure 2.2.

The PF operator  $\mathcal{L}_\tau : L^1 \rightarrow L^1$  corresponding to  $S_\tau$  is defined as (Lasota and Mackey 1994, Chapter 7):

$$\int_{S_\tau^{-1}(A)} f(x) d\mu = \int_A \mathcal{L}_\tau f(x) d\mu. \quad (2.5.2)$$

The Koopman operator  $\mathcal{U}_\tau : L^\infty \rightarrow L^\infty$  is defined as (Lasota and Mackey 1994, Chapter 7)

$$\mathcal{U}_\tau g(x) = g(S_\tau(x)). \quad (2.5.3)$$

or

$$\mathcal{U}_\tau g = g \circ S_\tau. \quad (2.5.4)$$

$\mathcal{L}_\tau$  and  $\mathcal{U}_\tau$  are adjoint:

$$\langle \mathcal{L}_\tau f, g \rangle = \langle f, \mathcal{U}_\tau g \rangle \quad \text{for } f \in L^1, g \in L^\infty. \quad (2.5.5)$$

Illustrations of the action of  $\mathcal{L}_\tau$  and  $\mathcal{U}_\tau$  are shown in Figures 2.1 and 2.2, both inspired by Mezic (2015).

In the context of Equation (2.5.5),  $f$  and  $g$  are often called *observables* in the literature (Ruelle 1986b; Young 2002; Froyland 2008; Chekroun et al. 2011; Tantet et al. 2015b; Butterley 2016). This is simply to be interpreted as some physical observable output of the system (Gaspard and Tasaki 2001; Mezic 2013; Susuki and Mezic 2015).

### 2.5.3 The Liouville Equation and the Transfer Operator

The transfer operator  $\mathcal{L}$  is intimately connected to the Liouville equation. Consider a vector field defined on a state space  $\Omega \subseteq \mathbb{R}^n$

$$\dot{\mathbf{x}} = \mathbf{F}(\mathbf{x}) \quad (2.5.6)$$

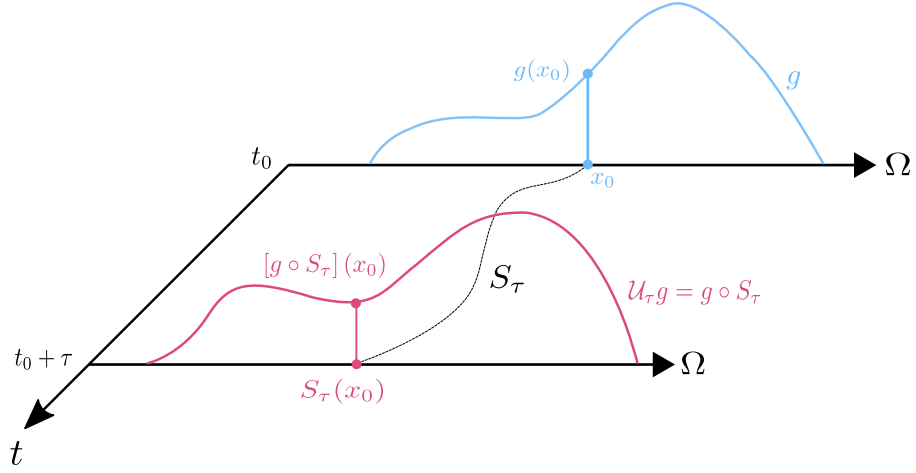


**Figure 2.2 | Illustration of the action of the Koopman operator.** The Koopman operator  $\mathcal{U}_\tau$  corresponding to the flow  $S_\tau$  propagates the observable  $g$  (Equation (2.5.3)). Compare with Figure 2.1

where  $\mathbf{x} \in \Omega$ . We consider the action of the vector field (Equation (2.5.6)) on an initial density  $\rho_0(\mathbf{x}, t = 0)$ ; for this initial density  $\rho_0$ , the Liouville equation specifies the evolution of densities (see for example Gaspard et al. (1995) or Nicolis (1995, Chapters 2 & 3)):

$$\partial_t \rho(\mathbf{x}, t) = -\nabla \cdot [\mathbf{F} \rho(\mathbf{x}, t)] := \hat{L} \rho(\mathbf{x}, t). \quad (2.5.7)$$

The solution  $\rho_\tau = \rho(\mathbf{x}, t = \tau)$  to Equation (2.5.7) is (Gaspard et al. 1995):

$$\rho_\tau = e^{\tau \hat{L}} \rho_0. \quad (2.5.8)$$

The Liouville operator  $\hat{L}$  is the *generator* of the transfer operator  $\mathcal{L}_\tau$  (Gaspard and Tasaki 2001)

$$\mathcal{L}_\tau = e^{\tau \hat{L}}. \quad (2.5.9)$$

#### 2.5.4 Discrete Spectrum of the Liouville Operator

For the sake of simplicity let us for now assume that  $\hat{L}$  has only discrete eigenvalues and that  $\{s_n\}$  form the set of eigenvalues corresponding to the eigenvectors  $\{\psi_n\}$ , and correspondingly that  $\{s_n^*\}$  are the eigenvalues of the adjoint  $\hat{L}^\dagger$  corresponding to the eigenvectors  $\{\tilde{\psi}_n\}$ :

$$\begin{aligned} \hat{L} \psi_n(\mathbf{x}) &= s_n \psi_n(\mathbf{x}), \\ \hat{L}^\dagger \tilde{\psi}_n(\mathbf{x}) &= s_n^* \tilde{\psi}_n(\mathbf{x}). \end{aligned} \quad (2.5.10)$$

Under certain conditions (Gaspard et al. 1995) we can assume that  $\{\psi_n\}$  and  $\{\tilde{\psi}_n\}$  are biorthogonal and complete

$$\begin{aligned}\langle \tilde{\psi}_n, \psi_m \rangle &= \delta_{m,n}, \\ \sum_n \psi_n(\mathbf{x}) \tilde{\psi}_n(\mathbf{y}) &= \delta(\mathbf{x} - \mathbf{y}).\end{aligned}\quad (2.5.11)$$

We now expand  $\rho(\mathbf{x}, t)$  using Equation (2.5.11) (Gaspard et al. 1995)

$$\rho(\mathbf{x}, t) = \sum_n c_n(t) \psi_n(\mathbf{x}) \quad (2.5.12)$$

and substitute Equation (2.5.12) into the evolution Equation (2.5.7):

$$\begin{aligned}\frac{\partial}{\partial t} \rho(\mathbf{x}, t) &= \frac{\partial}{\partial t} \sum_n c_n(t) \psi_n(\mathbf{x}) \\ &= \hat{L} \sum_n c_n(t) \psi_n(\mathbf{x}) \\ &= \sum_n c_n(t) s_n \psi_n(\mathbf{x}).\end{aligned}\quad (2.5.13)$$

For any given  $n$  the equation for  $c_n(t)$

$$\frac{\partial}{\partial t} c_n(t) \psi_n(\mathbf{x}) = c_n(t) s_n \psi_n(\mathbf{x}) \quad (2.5.14)$$

has the solution

$$c_n(t) = c_n(0) e^{ts_n} \quad (2.5.15)$$

so Equation (2.5.12) becomes

$$\rho(\mathbf{x}, t) = \sum_n c_n(0) e^{ts_n} \psi_n(\mathbf{x}). \quad (2.5.16)$$

Let us calculate  $c_n(0)$  - we set  $t = 0$  in Equation (2.5.16) and take the inner product with  $\tilde{\psi}_n$ :

$$\begin{aligned}\langle \tilde{\psi}_n, \rho_0 \rangle &= \langle \tilde{\psi}_n, \sum_m c_m(0) \psi_m \rangle \\ &= \sum_m c_m(0) \langle \tilde{\psi}_n, \psi_m \rangle \\ &= \sum_m c_m(0) \delta_{m,n} \\ &= c_n(0),\end{aligned}\quad (2.5.17)$$

leading us to the final expression for  $\rho(\mathbf{x}, t)$

$$\rho(\mathbf{x}, t) = \sum_n \langle \tilde{\psi}_n, \rho_0 \rangle e^{ts_n} \psi_n(\mathbf{x}). \quad (2.5.18)$$

The eigenvectors  $\tilde{\psi}_n$  and  $\psi_n$  may be either functions or distributions<sup>1</sup> depending on the system considered, but in either case an expansion of the form

<sup>1</sup>See eg. Gowers et al. (2008, pp. 184–187) for a definition.

Equation (2.5.18) will hold (Gaspard et al. 1995). It has been shown that for Anosov flows<sup>2</sup> the eigenvectors corresponding to isolated eigenvalues are distributions (Froyland 2008; Blank et al. 2002), and the same is the case for a one-dimensional vector field undergoing a pitchfork bifurcation (Gaspard et al. 1995) and a two-dimensional vector field undergoing a Hopf bifurcation (Gaspard and Tasaki 2001). On the other hand, in the case where random perturbations are added to the system the eigenvectors appear as functions (Dellnitz and Junge 1999; Froyland 2008).

### 2.5.5 Stationary Densities & Physical Measures

**Definition 2.4** (Invariant measure, Lasota and Mackey (1994), definition 4.1.1). Let  $(\Omega, \Sigma, \mu)$  be a measure space and  $S : \Omega \rightarrow \Omega$  a transformation on  $\Omega$ . The measure  $\mu$  is invariant under  $S$  if

$$\mu(S^{-1}(A)) = \mu(A) \quad \forall A \in \Sigma. \quad (2.5.19)$$

△

**Theorem 2.5** (Invariant measure and fixed points of  $\mathcal{L}_\tau$ , Lasota and Mackey (1994) Theorem 4.1.1). Let  $(\Omega, \Sigma, \mu)$  be a measure space,  $S : \Omega \rightarrow \Omega$  a transformation on  $\Omega$  and  $\mathcal{L}_\tau$  the PF operator corresponding to  $S_\tau$ . Then the measure  $\mu_f$

$$\mu_f(A) = \int_A f(x) d\mu \quad (2.5.20)$$

is invariant under  $S$  if and only if  $f$  is a fixed point of  $\mathcal{L}_\tau$ ; that is iff

$$\mathcal{L}_\tau f = f. \quad (2.5.21)$$

△

If Equation (2.5.21) holds for a density  $f$  then  $f$  is a stationary density of the PF operator (Lasota and Mackey 1994, p. 41).

In the case where we are working with a dissipative dynamical system, volume in state space is in general not preserved (Strogatz 1994). In this case it is important to choose a physical measure for which spatial and temporal averages coincide (Tantet et al. 2015a):

**Definition 2.6** (Physical Measure, (Eckmann and Ruelle 1985; Young 2002)). Suppose  $S : \Omega \rightarrow \Omega$  is an arbitrary map and  $\mu$  an invariant probability measure.  $\mu$  is a physical measure if there is a set with positive Lebesgue measure  $A \subset \Omega$  such that for every continuous observable function  $f : \Omega \rightarrow \mathbb{R}$  and for all  $x \in A$

$$\lim_{N \rightarrow \infty} \frac{1}{N} \sum_{n=0}^{N-1} f(S^n(x)) = \int_{\Omega} f(x) d\mu. \quad (2.5.22)$$

△

---

<sup>2</sup>See eg. Young (2002).

Physical measures – more specifically Sinai-Ruelle-Bowen (SRB) measures – have been shown to exist for Anosov flows (Young 2002). To the author’s knowledge, SRB measures have not been shown to exist for dynamical systems in general. However, Gallavotti and Cohen (1995) propose the so-called chaotic hypothesis under which we can regard many practical systems as being “close enough” to Anosov – see Section 2.6.4. With two additional definitions we can say something about the uniqueness of the invariant distribution:

**Definition 2.7** (Lasota and Mackey (1994), definition 4.3.1). Let  $(\Omega, \Sigma, \mu)$  be a measure space; a transformation  $S : \Omega \rightarrow \Omega$  is called mixing if

$$\lim_{n \rightarrow \infty} \mu(A \cap S^{-n}(B)) = \mu(A)\mu(B) \quad \forall A, B \in \Sigma. \quad (2.5.23)$$

△

For a finite  $n$  consider the set

$$C = A \cap S^{-n}(B). \quad (2.5.24)$$

If  $x \in S^{-n}(B)$  then  $S^n(x)$  must lie in  $B$ . Thus the set  $C$  in Equation (2.5.24) can be written

$$C = \{x \mid x \in A \text{ and } S^n(x) \in B\}. \quad (2.5.25)$$

We can interpret the mixing condition Equation (2.5.23) as follows: for any point  $x \in \Omega$  the probability of  $x$  lying in  $A$  and  $S^n(x)$  lying in  $B$  is proportional to the product of the measures of  $A$  and  $B$  – that is at least if  $\mu(\Omega) = 1$ .

**Definition 2.8** (Lasota and Mackey (1994), definition 4.3.1). Let  $(\Omega, \Sigma, \mu)$  be a measure space and  $S : \Omega \rightarrow \Omega$  a nonsingular transformation.  $S$  is called ergodic if for every invariant set  $A \in \Sigma$  either  $\mu(A) = 0$  or  $\mu(\Omega \setminus A) = 0$ . △

The definition of ergodicity thus tells us that almost all sets  $A \in \Sigma$  will be visited by  $S^n(x)$  for almost every  $x \in \Omega$  – that is, pick an initial condition and, given enough iterations of the map  $S$  we will visit every set  $A \in \Sigma$  almost surely. A mixing  $S$  transformation is also ergodic (Lasota and Mackey 1994, p. 65) – and if  $S$  is ergodic there is at most one unique stationary density (Lasota and Mackey 1994, Theorem 4.2.2).

## 2.6 Relating the Spectra of the Liouville and Transfer Operators

### 2.6.1 Spectrum of the PF Operator

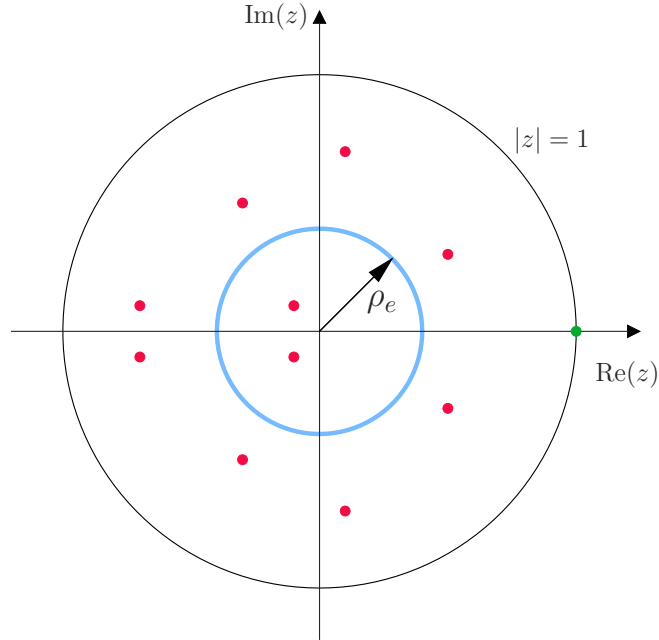


**Figure 2.3 | Illustration of the spectrum of the PF operator.** When acting on functions of bounded variation, eigenvalues of the PF operator with modulus larger than  $\rho_e$  are isolated and of finite multiplicity<sup>3</sup>(Dellnitz et al. 2000; Froyland et al. 2009).

Denote  $BV([0, 1])$  the space of functions of bounded variation on the interval  $[0, 1]$ . For the transfer operator restricted to the space  $BV([0, 1])$  it can be shown that the spectrum of the transfer operator  $\sigma(\mathcal{L})$  lies within the unit disc and 1 is an eigenvalue of  $\mathcal{L}$  (Keller 1984; Dellnitz et al. 2000; Froyland et al. 2009; Froyland et al. 2014).

In this setting the essential spectrum of the transfer operator is located within a disc of radius  $\rho_e$  called the essential spectral radius; spectral points outside  $\rho_e$  are eigenvalues of finite multiplicity (Dellnitz et al. 2000; Froyland et al. 2014) and will be referred to as *isolated eigenvalues* (Froyland 2007). The points in the spectrum of  $\mathcal{L}$  correspond (Dorfman 1999, p. 259), (Gaspard and Tasaki 2001) to the so-called *Ruelle-Pollicott resonances* (Pollicott 1985; Ruelle 1986a; Ruelle 1986b).

Below we will approximate  $\mathcal{L}$  with the matrix representation  $P_{ij}$  (see Section 2.8). In general, eigenvalues  $\lambda_k$  of  $P_{ij}$  will correspond to eigenvalues of

<sup>3</sup>We sketch the essential spectrum as a circle and not a disc due to a result from Blank et al. (2002), who show that the essential spectrum in some cases is contained in an *annulus*, and not a disc – as discussion of this result is out of the scope of this thesis.

$\mathcal{L}$  (Dellnitz et al. 2000). If we assume that a calculation of  $\rho_e$  is possible and that for a given eigenvalue  $\lambda_k$  of  $P_{ij}$  we have  $|\lambda_k| > \rho_e$ , then we will know that  $\lambda_k$  is an isolated eigenvalue (Dellnitz et al. 2000). If on the other hand  $|\lambda_k| \leq \rho_e$  we only know  $\lambda_k$  is an eigenvalue of  $\mathcal{L}$ , not whether it is isolated; further there may be isolated eigenvalues  $\lambda_k, |\lambda_k| \leq \rho_e$  that are not eigenvalues of  $P_{ij}$  (Dellnitz et al. 2000).

General proofs of existence for isolated eigenvalues other than the unit eigenvalue is an open problem (Froyland et al. 2014). However Dellnitz et al. (2000) conjecture that isolated eigenvalues may indeed be present in many “systems arising in applications” which is encouraging, given the many interesting and recent results discussed in Section 1.4.

Let  $\{\lambda_1, \lambda_2, \dots, \lambda_N\}$  denote the isolated eigenvalues of  $\mathcal{L}$  ordered in decreasing order so that eigenvalues of multiplicity larger than one occurs only once. By the arguments above we see that  $\lambda_1 = 1$ . We will be especially interested in the subdominant eigenvalue  $\lambda_2 = \max_{1 < i \leq N} |\lambda_i|$  since this is responsible for the rate of decay of correlations detailed in Section 2.7 (Baladi 2000; Dellnitz et al. 2000; Froyland 2008).

A sketch of the possible PF spectrum is shown in Figure 2.3. The unit eigenvalue is in green, isolated eigenvalues in red and  $z : |z| \leq \rho_e$  is shown in blue. Compare this to Figures 2.4 and 2.5 where we show Ulam approximations to the spectrum of the the PF operators for the Lorenz system and the Van der Pol oscillator, respectively.

### 2.6.2 One-parameter Semigroups

**Definition 2.9** ((Engel and Nagel 2000), definition I.5.1). A family of bounded linear operators  $\{T_t\}_{t \geq 0}$  on a Banach space  $\Omega$  is said to be a strongly continuous one-parameter semigroup if

$$\begin{aligned} T_{s+t} &= T_s T_t \quad \forall t, s \geq 0 \\ T_0 &= I \end{aligned} \tag{2.6.1}$$

and if the orbit maps

$$\xi_x : t \rightarrow \xi_x(t) := T_t(x) \tag{2.6.2}$$

are continuous from  $\mathbb{R}_+$  into  $\Omega$  for all  $x \in \Omega$ . △

### 2.6.3 The Spectral Mapping Theorem

We will need the Spectral Mapping Theorem (SMT) when relating the eigenvalues of the transfer operator  $\mathcal{L}_\tau$  to the eigenvalues of the generator  $\hat{L}$ . Denote  $P\sigma(\cdot)$  the point spectrum, or set of eigenvalues, of an operator.

**Theorem 2.10** (IV.1.6 and IV.3.7, Engel and Nagel (2000)). For the generator  $\mathcal{A}$  of a strongly continuous semigroup  $\{T_t\}_{t \geq 0}$  on a Banach space  $\Omega$  the following holds:

$$P\sigma(T_t) \setminus \{0\} = e^{tP\sigma(\mathcal{A})}. \tag{2.6.3}$$

△

### 2.6.4 The Chaotic Hypothesis

By introducing the appropriate Banach spaces, Butterley and Liverani (2007) show that – for Anosov systems – the semigroup of transfer operators  $\mathcal{L}_\tau$  is strongly continuous and that therefore the spectrum of the generator  $\hat{L}$  of  $\mathcal{L}_\tau$  is contained in  $\{z \mid \operatorname{Re}\{z\} \leq 0\}$  (Tantet et al. 2015a).

If we assume the *chaotic hypothesis* (Gallavotti and Cohen 1995):

“A reversible many particle system in a stationary state can be regarded as a transitive Anosov system for the purpose of computing the macroscopic properties of the system.”

we can consider our system as “close enough” to an Anosov system that the semigroup of transfer operators is a strongly continuous semigroup, and thus the spectral mapping theorem will hold (Tantet et al. 2015a).

## 2.7 Decay of Correlations

For  $f \in L^1$  and  $g \in L^\infty$  the following defines a *correlation function* between the observables  $f$  and  $g$  (Ruelle 1986b; Butterley and Liverani 2007; Tantet et al. 2015a):

$$C_{f,g}(\tau) = \int f \cdot g \circ S_\tau d\mu - \int f d\mu \int g d\mu. \quad (2.7.1)$$

For a mixing system, the correlation function Equation (2.7.1) will converge to zero,  $C_{f,g}(\tau) \rightarrow 0$  as  $\tau \rightarrow \infty$  (Lasota and Mackey 1994, Proposition 4.4.1 b). We write the first term on the right hand side of Equation (2.7.1) as

$$\int f \cdot g \circ S_\tau dx = \langle f, g \circ S_\tau \rangle; \quad (2.7.2)$$

using the definitions of the transfer and Koopman operators (Equations (2.5.4) and (2.5.5))

$$\langle f, g \circ S_\tau \rangle = \langle f, \mathcal{U}_\tau g \rangle = \langle \mathcal{L}_\tau f, g \rangle, \quad (2.7.3)$$

and by the relationship between the  $\hat{L}$  and  $\mathcal{L}_\tau$  (Equation (2.5.9))

$$\langle \mathcal{L}_\tau f, g \rangle = \langle e^{\tau \hat{L}} f, g \rangle. \quad (2.7.4)$$

Still only considering the discrete spectrum, as in Section 2.5.4 we assume bi-orthogonality and completeness such that

$$f = \sum_n \langle \tilde{\psi}_n, f \rangle \psi_n. \quad (2.7.5)$$

With the eigenrelations  $\hat{L}\psi_n = s_n\psi_n$ ,

$$e^{\tau \hat{L}} f = \sum_n \langle \tilde{\psi}_n, f \rangle e^{\tau s_n} \psi_n. \quad (2.7.6)$$

Equation (2.7.4) now reads

$$\langle \mathcal{L}_\tau f, g \rangle = \sum_n \langle \tilde{\psi}_n, f \rangle e^{\tau s_n} \langle g, \psi_n \rangle \quad (2.7.7)$$

and, crucially, by the SMT

$$\langle \mathcal{L}_\tau f, g \rangle = \sum_n \langle \tilde{\psi}_n, f \rangle \lambda_n \langle g, \psi_n \rangle \quad (2.7.8)$$

where  $\lambda_n$  are the eigenvalues of the transfer operator  $\mathcal{L}_\tau$ .

### 2.7.1 Projection of the Essential Spectrum

We now turn our attention to the essential spectrum of the transfer operator. It has been shown that for Anosov flows the spectral decomposition of Equation (2.7.1), including the essential spectrum, is given as (Tantet et al. 2015b; Butterley 2016):

$$\begin{aligned} C_{f,g}(\tau) &= \langle \mathcal{L}_\tau f, g \rangle - \int f d\mu \int g d\mu \\ &= \sum_{n=1}^M e^{\tau s_n} \langle \tilde{\psi}_n, f \rangle \langle g, \psi_n \rangle + \langle \Lambda_\tau f, g \rangle - \int f d\mu \int g d\mu \end{aligned} \quad (2.7.9)$$

where  $M$  is finite and the term  $\Lambda_\tau$  corresponds to the essential spectrum of  $\mathcal{L}_\tau$ . Butterley (2016) gives a bound on the contribution from the term  $\langle \Lambda_\tau, f \rangle$ . The essential spectrum governs local properties such as exponential separation of nearby trajectories (Dellnitz et al. 2000) – as mentioned in Section 2.6.1 we are interested in the decay of correlations caused by the isolated eigenvalues and will therefore not further consider the essential spectrum. If the system corresponding to  $\mathcal{L}_\tau$  is mixing, the first term in the sum in Equation (2.7.9) corresponding to  $s_1 = 0$  cancels out with the term  $\int f d\mu \int g d\mu$  (Tantet et al. 2015b). To see this, recall that for a mixing system we have (Lasota and Mackey (1994, Corollary 4.4.1), Chekroun et al. (2011) and Definition 2.7)

$$\langle \mathcal{L}_\tau f, g \rangle \xrightarrow{\tau \rightarrow \infty} \int f d\mu \int g d\mu. \quad (2.7.10)$$

By assuming the chaotic hypothesis we know  $\sigma(\hat{\mathcal{L}})$  is contained in  $\{z \mid \operatorname{Re}(z) \leq 0\}$  and further that  $\lambda_n = e^{\tau s_n}$  is an eigenvalue of  $\mathcal{L}_t$ . Since  $\operatorname{Re}(s_n) < 0$  for  $n = 2, 3, 4, \dots$  the correlations will decay exponentially and

$$\langle \tilde{\psi}_1, f \rangle \langle g, \psi_1 \rangle = \int f d\mu \int g d\mu. \quad (2.7.11)$$

### 2.7.2 The Spectral Gap and Decorrelation Time

The spectral gap  $1 - |\lambda_2|$  considered in Chekroun et al. (2014) can be related to the decorrelation time  $\tau_C$  defined as the time when the correlation function  $C_{f,g}(t)$  has decayed to  $1/e$ :

$$C_{f,g}(t) \sim e^{t/\tau_C}. \quad (2.7.12)$$

Consider Equation (2.7.9) and assume that the subdominant eigenvalue  $\lambda_2$  of  $\mathcal{L}_\tau$  is primarily responsible for the decay of correlation. Let  $\psi_2$  be the

eigenvector corresponding to  $\lambda_2$  and assume the spectral mapping theorem holds so  $\lambda_2 = e^{\tau s_2}$  (Tantet et al. 2015a):

$$\begin{aligned}\langle \mathcal{L}_\tau \psi_2, g \rangle &= \lambda_2 \langle \psi_2, g \rangle \\ &= e^{\tau s_2} \langle \psi_2, g \rangle \\ &= e^{\tau \operatorname{Re}(s_2)} e^{\tau \operatorname{Im}(s_2)} \langle \psi_2, g \rangle.\end{aligned}\tag{2.7.13}$$

To connect Equation (2.7.12) and Equation (2.7.13) we set

$$\tau_{C,2} = \frac{-1}{\operatorname{Re}(s_2)}.\tag{2.7.14}$$

The subscript “2” in Equation (2.7.14) is there to remind us that we only considered the effect of the subdominant eigenvalue  $\lambda_2$ . Since  $\lambda_2 = e^{\tau s_2}$  we see that  $s_2 = \ln(\lambda_2)/\tau$  and  $\operatorname{Re}(s_2) = \ln|\lambda_2|/\tau$ . We put this expression into Equation (2.7.14):

$$\tau_{C,2} = -\frac{\tau}{\ln|\lambda_2|}.\tag{2.7.15}$$

Since the spectral gap is  $\gamma = 1 - |\lambda_2|$  we get

$$\tau_{C,2} = -\frac{\tau}{\ln(1 - \gamma)}\tag{2.7.16}$$

or, in the case where decay of correlation is primarily caused by  $\lambda_2$ ,

$$\tau_C \approx -\frac{\tau}{\ln(1 - \gamma)}.\tag{2.7.17}$$

We keep in mind that Equation (2.7.17) is merely an approximation as we only considered the effect of the eigenvalue  $\lambda_2$ .

## 2.8 Ulam Approximation of the Transfer Operator

The transfer operator  $\mathcal{L}_\tau$  can be approximated by a method originally proposed by Ulam (1964, Section VI.4) and further described by eg. Froyland (1998), Dellnitz and Junge (1999), and Chekroun et al. (2014).

This method works by first dividing the state space  $\Omega$  into a set of boxes  $\{B_i\}_{i=1}^N$ . Then for a specific lag  $\tau$  we calculate the observed transition probabilities

$$P_{ij}(\tau) = \frac{\#\{x(t) \in B_i \wedge x(t + \tau) \in B_j\}}{\#\{x(t) \in B_i\}}\tag{2.8.1}$$

as an estimate of the true transition probabilities  $\mathbb{P}_{ij}(\tau)$ . We will sometimes for convenience abstain from referring explicitly to the lag  $\tau$  when there is no risk of confusion. Because  $P_{ij}$  is a stochastic matrix whose rows sum to 1, the following will characterize stationarity (Asmussen 2003):

$$\boldsymbol{\pi} P_{ij} = \boldsymbol{\pi}\tag{2.8.2}$$

that is,  $\boldsymbol{\pi}$  is the left eigenvector with eigenvalue 1.  $P_{ij}$  is the maximum likelihood estimate of  $\mathbb{P}_{ij}$  and converges to  $\mathbb{P}_{ij}$  as the number of boxes  $N \rightarrow \infty$ , with and error of order  $\mathcal{O}(N^{-1/2})$  (Chekroun et al. (2014) and references therein).

### 2.8.1 State Space Reduction

As mentioned in Section 1.4, a theorem by Chekroun et al. (2014) allows us to study trajectories on the reduced state space  $Y$  of a system instead of the full state space  $\Omega$ . This allowed Chekroun et al. (2014), Tantet et al. (2015a), and Tantet et al. (2015b) to study only a few outputs of a high-dimensional system. By the same argument, we will study only a few climate proxies in Chapter 5 with the hope of gaining knowledge of the climatic system.

Consider a system  $S$  acting on a state space  $\Omega \subset \mathbb{R}^n$  that has a unique physical measure  $\mu$ . Let  $h$  be a continuous observation function  $h : \Omega \rightarrow Y \in \mathbb{R}^m$  with  $m < n$ , and suppose we observe a trajectory  $x(t) \in \Omega$  such that  $h(x(t)) = y(t) \in Y$ . Chekroun et al. (2014) show that (Tantet et al. 2015a)

$$\mathbb{P}(y(t) \in B_i \wedge y(t+\tau) \in B_j) = \mathbb{P}(x(t) \in h^{-1}(B_i) \wedge x(t+\tau) \in h^{-1}(B_j)). \quad (2.8.3)$$

Thus the observation function  $h$  preserves transition probabilities.

### 2.8.2 Significance of the Lag Parameter $\tau$

It is challenging to give a precise interpretation of the meaning of the lag parameter  $\tau$  when estimating  $\mathcal{L}_\tau$  from data. In general, the choice of  $\tau$  should reflect the timescale of changes in the data we wish to examine – a large  $\tau$  will disregard fast fluctuations as noise (Tantet et al. 2015b).

Furthermore, using the theorem by Chekroun et al. (2014) (Section 2.8.1) comes with a price. The projection will in most cases introduce a memory effect such that the SMT cannot be expected to hold and the spectral gap  $\gamma$  will depend on the choice of lag  $\tau$  (Tantet et al. 2015a; Tantet et al. 2015b). Thus to verify our results we will calculate the spectral gap for a range of lags  $\tau_1, \tau_2, \dots$  in Chapters 4 and 5.

### 2.8.3 The Spectral Gap and Mixing Rate of Markov Matrices

The results considered in Section 2.6.1 concerning the spectrum of the PF operator and the results considered in Section 2.7 can also be understood in the context of Markov matrices. To see this we need a few definitions.

First, denote a matrix  $P$  with real entries  $p_{ij}$  as non-negative if the entries  $p_{ij} \geq 0$  for all  $i$  and  $j$ , and positive if  $p_{ij} > 0$  for all  $i$  and  $j$ ; similarly, denote a vector  $\pi$  as non-negative if  $\pi_i \geq 0$  for all  $i$ , or positive if  $\pi_i > 0$  for all  $i$ .

**Definition 2.11** (Irreducible Markov chain, Levin et al. (2008), p. 8). Let  $P$  be the transition matrix of a Markov chain on a finite state space  $\Omega$ . A Markov chain is called irreducible if it is possible to get from any state  $x \in \Omega$  to any other state  $y \in \Omega$ .  $\triangle$

For an irreducible Markov chain there exists a unique probability distribution  $\pi$  such that  $\pi P = \pi$  (Levin et al. 2008, p. 14). Next we introduce the Frobenius theorem (Leon 2006, p. 395), which tells us that if  $P$  is an irreducible, non-negative matrix then  $P$  has a positive real eigenvalue  $\lambda_1$ ; furthermore,

- $\lambda_1$  corresponds to a positive eigenvector  $\pi$ ,

- For any other eigenvalues  $\lambda$  of  $P$ , it holds that  $|\lambda| \leq \lambda_1$ . All eigenvalues  $\lambda_k : |\lambda_k| = \lambda_1$  are simple roots of the characteristic polynomial of  $P$  and of the form

$$\lambda_k = \lambda_1 e^{2\pi ki/m}, \quad k = 0, 1, \dots, m-1 \quad (2.8.4)$$

where  $m$  is the number of such eigenvalues.

If  $P$  is a Markov operator on a finite state space  $\Omega$  we know that 1 is always an eigenvalue of  $P$  (Davies 2007, p. 361) and that for all eigenvalues  $\lambda$  of  $P$  it will hold that  $|\lambda| \leq 1$  (Levin et al. 2008, p. 153) – thus the  $\lambda_1$  in Equation (2.8.4) is equal to 1 for Markov matrices.

**Definition 2.12** (Period of Markov chain, Levin et al. (2008) p. 8). Let  $\mathcal{T}(x) = \{n \geq 1 : P^n(x, x) > 0\}$  be the set of times where the chain can return to the state  $x$ . The period of the state  $x$  is the greatest common divisor of the set  $\mathcal{T}(x) := \gcd(\mathcal{T}(x))$ . If the chain represented by  $P$  is irreducible then  $\mathcal{T}(x) = \mathcal{T}(y) \quad \forall x, y \in \Omega$ . The chain is aperiodic if all states have period 1 – otherwise it is periodic.  $\triangle$

With these definitions in place, let  $P$  with entries  $p_{ij}$  be the transition matrix for a Markov chain on a finite state space  $\Omega$ , with stationary distribution  $\boldsymbol{\pi}$ . If  $P$  is irreducible and aperiodic then  $P$  is called *ergodic*, and (Asmussen 2003, Corollary I.3.7 and Theorem I.4.2) then

$$p_{ij}^n \rightarrow \pi_j, \quad n \rightarrow \infty \quad (2.8.5)$$

for all  $j$ ; ie  $P^n \rightarrow \mathbf{1}\boldsymbol{\pi}$ . If  $\lambda_2$  is the second largest eigenvalue of  $P$ ,  $\lambda_2 = \max\{z \in \text{sp}(P) : |z| < 1\}$ ; the convergence in Equation (2.8.5) happens on the order of (Asmussen 2003, Proposition I.6.2)

$$p_{ij}^n = \pi_j + \mathcal{O}(n^k \lambda_2^n), \quad n \rightarrow \infty \quad (2.8.6)$$

for some constant  $k$ .

Thus, from Equation (2.8.6), we can expect  $\lambda_2$  to encode valuable information about the system dynamics if the transition matrices  $P_{ij}(\tau)$  represent aperiodic and irreducible Markov chains. This also provides a convenient check of our methodology – we will check numerically if irreducibility and aperiodicity are fulfilled in the obtained matrices (eg. Section 2.10.1).

## 2.9 Estimating Errors on Markov Matrices

To estimate errors on matrices obtained with the methods in Section 2.8 we use the following bootstrap method also employed in Chekroun et al. (2014) and Tantet et al. (2015a). I find that this relatively simple and intuitive approach is too easily obscured by matrix notation so I will instead use a simple example.

Suppose the  $i$ th row of the unnormalized transition matrix  $\tilde{P}$  on a state space partitioned into boxes  $\{B_i\}_{i=1}^{10}$  is given by:

$$\tilde{P}_{i,\cdot} = (2, 0, 3, 0, 0, 4, 0, 1, 0, 0). \quad (2.9.1)$$

In this case we have recorded 2 transitions from state  $i$  to state 1, 0 transitions from state  $i$  to state 2 and so on. We normalize the row to obtain observed transition probabilities:

$$P_{i,\cdot} = (0.2, 0, 0.3, 0, 0, 0.4, 0, 0.1, 0, 0) \quad (2.9.2)$$

Since  $\sum_j \tilde{P}_{ij} = 10$  we now draw 10 times from a multinomial distribution with probabilities corresponding to Equation (2.9.2). The result will be the surrogate row  $\tilde{s}_{i,\cdot}$  and might look like

$$\tilde{s}_{i,\cdot} = (3, 0, 2, 0, 0, 5, 0, 0, 0, 0). \quad (2.9.3)$$

This process is repeated for every row, and the resulting matrix normalized so that a surrogate transition matrix  $P_{sg}$  is formed. We form a total of  $N_{sg}$  surrogate matrices ( $N_{sg}$  is specified in Chapters 4 and 5 when relevant) and calculate the spectral gap  $\gamma_i$  for each surrogate matrix. The set  $\{\gamma_i\}$  of spectral gaps is then ordered. Since this bootstrap method introduces a bias towards lower mixing rates (Tantet et al. 2015a) the mean of the set  $\{\gamma_i\}$  is adjusted so that it is centered on the original spectral gap  $\gamma$ . For a confidence level  $\beta$  the lower and upper bounds will be taken as the  $(\beta/2)$ th and  $(1 - \beta/2)$ th percentiles on the set of adjusted spectral gaps, respectively.

## 2.10 The Transfer Operator and Noise

Gaspard et al. (1995) consider two one-dimensional vector fields,

$$\dot{x} = px \quad (2.10.1)$$

and

$$\dot{x} = px - x^3, \quad (2.10.2)$$

the latter undergoing a pitchfork bifurcation (Chapter 3). Gaspard et al. (1995) find that far from the bifurcation the spectrum of the Liouville operator is discrete, whereas the spectrum is *continuous* close the bifurcation. As described in Section 2.5.3, the evolution of a density is described by the Liouville equation which we repeat here for convenience; if the vector field

$$F(x) = \dot{x} \quad (2.10.3)$$

is one-dimensional, the Liouville equation reads

$$\frac{\partial}{\partial t} \rho(x, t) = -\frac{\partial}{\partial x} [F(x)\rho(x, t)]. \quad (2.10.4)$$

If we add Gaussian white noise to the process Equation (2.10.3) as in Section 2.3.2

$$dXt = F(x)dt + \sigma dWt \quad (2.10.5)$$

the system is instead governed by the Fokker-Planck equation (Dijkstra 2013)

$$\frac{\partial}{\partial t} \rho(x, t) = -\frac{\partial}{\partial x} [F(x)\rho(x, t)] + \frac{1}{2} \frac{\partial^2}{\partial x^2} [\sigma^2 \rho(x, t)]. \quad (2.10.6)$$

For both systems considered in Gaspard et al. (1995) (that is, Equations (2.10.1) and (2.10.2)) the Fokker-Planck (FP) spectrum is calculated and found to converge to the Liouville spectrum in the noiseless limit.

Blank and Keller (1998) consider maps and show that in some cases the PF spectrum can be unstable in the presence of noise. First it is important to note that for the noise they consider, any limit point of eigenvalues of the PF

operator corresponding to the system with noise that lies *outside* the essential spectral radius correspond to the eigenvalues of the unperturbed PF operator (Blank and Keller 1998, Theorem 1.1). Blank and Keller (1998) consider examples of maps where either Ulam’s approximation or the noise may lead to poor results. However, as Froyland (2008) points out “there are no isolated eigenvalues for Ulam’s method to approximate” in the cases mentioned in Blank and Keller (1998).

### 2.10.1 Examples of Spectrums: Well-Known Dynamical Systems With Noise

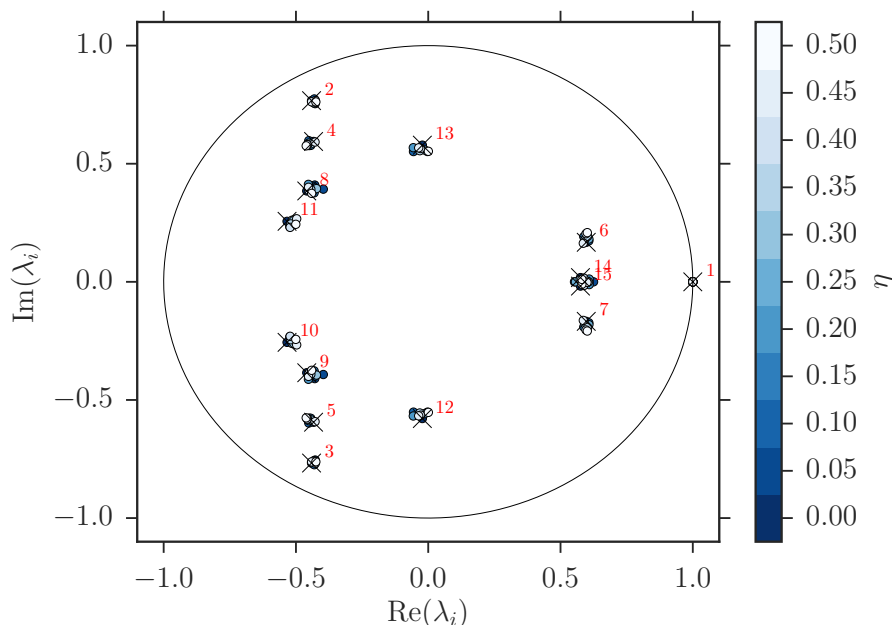


**Figure 2.4 | Eigenvalues of transition matrix for the Lorenz (1963) system.** Trajectory integrated without noise (crosses and darkest blue), and with random noise  $\sim \mathcal{N}(0, \eta^2 \Delta t)$  added at every time step. The 15 eigenvalues with largest absolute magnitude are shown, numbered in decreasing order. See Table 2.1 for parameters used.

Here we illustrate the effect of noise on the spectrum of  $\mathcal{L}_\tau$  – as approximated by the eigenvalues of  $P_{ij}(\tau)$  – by investigating the van der Pol (1927) oscillator and the Lorenz (1963) system, both classical examples of nonlinear systems (eg. Strogatz (1994), whence we obtain Equations (2.10.7) and (2.10.8)). We write the van der Pol oscillator in  $(x, y)$ -coordinates as

$$\begin{aligned} \dot{x} &= y, \\ \dot{y} &= -(x^2 - 1)y, \end{aligned} \tag{2.10.7}$$

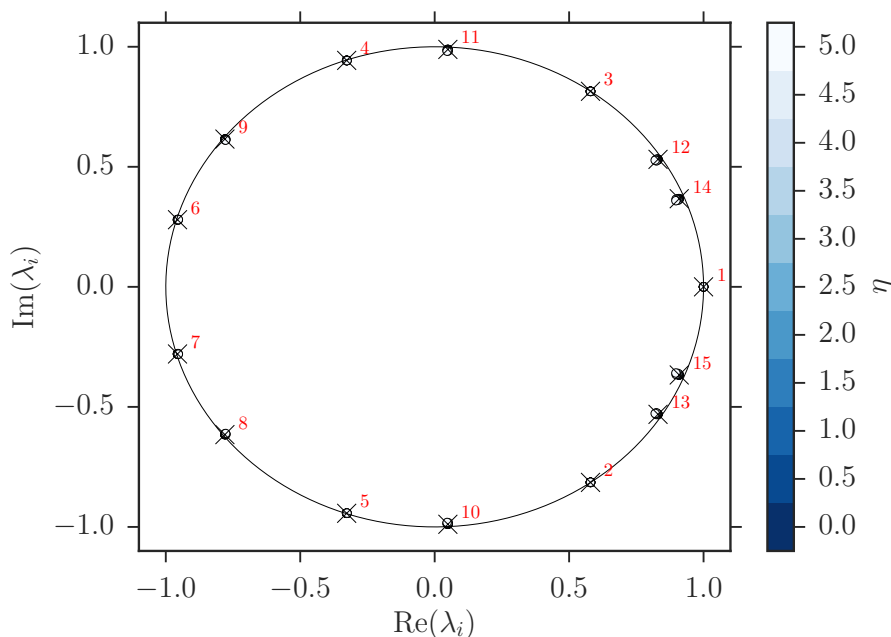


**Figure 2.5 | Eigenvalues of transition matrix for the van der Pol (1927) oscillator.** Interpretation as Figure 2.4. Note that considerably more noise is applied than for the Lorenz system. It is remarkable that all calculated eigenvalues are situated so close to the unit circle.

and use the “standard” parameters in the Lorenz system:

$$\begin{aligned}\dot{x} &= 10(y - x), \\ \dot{y} &= x(28 - z) - y, \\ \dot{z} &= xy - (8/3)z.\end{aligned}\tag{2.10.8}$$

Figures 2.4 and 2.5 (inspired by Ostruszka and Zyczkowski (2001)) show the 15 eigenvalues with largest absolute magnitude of  $P_{ij}(\tau)$  for the Lorenz system and the Van der Pol oscillator, respectively.

To make these figures, we integrate the systems with the Runge-Kutta (RK) method (Weber and Arfken 2003, p. 466) with and without noise, the magnitude of which is denoted by the (discrete) color bars; at each time step white noise with standard deviation  $\eta\sqrt{dt}$  is added. For the van der Pol system, we calculate  $P_{ij}(\tau)$  directly from the  $(x, y)$ -coordinates. For the Lorenz system we apply principal component analysis (PCA) (using the Python library `Scikit-learn`; Pedregosa et al. (2011)) and project the  $(x, y, z)$ -coordinates on to  $(p_1, p_2)$  from which  $P_{ij}(\tau)$  is calculated; the PCA projection thus constitutes the observation of the system,  $h : \Omega \rightarrow Y$  (Chekroun et al. 2014).

In each case, the two dimensional (reduced for the Lorenz system) state space is partitioned into  $50 \times 50$  boxes, spanning minimum and maximum values. Boxes never visited by the trajectories are discarded before calculating  $P_{ij}(\tau)$ .

We note that – in both cases – the eigenvalues of the systems integrated with and without noise coincide very well. This is the most important finding. It is remarkable that the eigenvalues of  $P_{ij}(\tau)$  calculated for the van der Pol system are all very close to the unit circle ( $|\lambda_i| > 0.98, i = 1 \dots 15$ ). For both the van der Pol and Lorenz systems, all transition matrices represented irreducible and aperiodic Markov chains<sup>4</sup>.

	Lorenz (1963)	van der Pol (1927)
$\mathbf{x}_0$	(1, 1, 1)	(0.5, 0)
$\Delta t$	0.01	0.01
$t_s$	0	0
$t_0$	500	500
$t_1$	2500	2500
$(N_r \times N_c)$	(50 × 50)	(50 × 50)
$\tau$	1	1

**Table 2.1 | Parameters used for Figures 2.4 and 2.5.** Both systems are integrated from  $t_s$  to  $t_1$  with at time step of  $\Delta t$  using the standard RK method (Weber and Arfken 2003), adding noise at every time step (see text). The initial condition is  $\mathbf{x}_0$ ; in order to discard transients we use data from  $t_0$  to  $t_1$  for calculating  $P_{ij}(\tau)$ .  $N_r$  and  $N_c$  denote the number of rows and columns, respectively, used for partitioning the 2-dimensional state spaces (reduced state space for the Lorenz system).

## 2.11 How to Apply the Transfer Operator

Here we provide a summary of Sections 2.5 to 2.10.

1. We observe a dynamical system  $S : \Omega \rightarrow \Omega$  operating on a space  $\Omega \subset \mathbb{R}^n$  through a continuous observable  $h : \Omega \rightarrow Y$  where  $Y \subset \mathbb{R}^m, m < n$  (Section 2.8.1).
2. We partition the reduced state space  $Y$  into “boxes”  $\{B_i\}_{i=1}^N$  and calculate the observed transition probabilities

$$P_{ij}(\tau) = \frac{\#\{x(t) \in B_i \wedge x(t + \tau) \in B_j\}}{\#\{x(t) \in B_i\}} \quad (2.11.1)$$

as an approximation of the true transition probabilities  $\mathbb{P}_{ij}(\tau)$  (Equation (2.8.1)).

3. The transition probabilities on the reduced state space  $Y$  are connected to the transition probabilities on the full state space  $\Omega$  by the observable  $h : \Omega \rightarrow Y$  (Chekroun et al. 2014) (Equation (2.8.3)).
4. The transition probabilities  $P_{ij}(\tau)$  are used as an approximation of the transfer operator  $\mathcal{L}_\tau$  (Section 2.8).

<sup>4</sup> We use the functions `is_aperiodic()` and `is_strongly_connected()` from the Python package `NetworkX` (Hagberg et al. (2008) – see also Appendix B) to determine this numerically.

5. By assuming the chaotic hypothesis we regard the dynamical system  $S$  as an Anosov system for the purpose of our calculations (Section 2.6.4).
6. For Anosov systems, Butterley and Liverani (2007) show that the semigroup of transfer operators  $\{\mathcal{L}_t\}_{t \geq 0}$  is strongly continuous (Section 2.6.4).
7. For a strongly continuous semigroup the spectral mapping theorem holds

$$P\sigma(\mathcal{L}_\tau) \setminus \{0\} = e^{P\sigma(\tau\hat{L})} \quad (2.11.2)$$

where  $P\sigma(\cdot)$  denotes the point spectrum of an operator (Section 2.6.3).

8. The spectral mapping theorem allows us – for strongly continuous semigroups – to relate the eigenvalues of the generator  $\hat{L}$  to the eigenvalues of the transfer operator  $\mathcal{L}_\tau$  (Section 2.6.3). This relation in turn yields information regarding the decay of correlations of two observables  $f$  and  $g$  (Section 2.7).
9. As the observable  $h : \Omega \rightarrow Y$  introduces memory effects (Section 2.8.2), we calculate the spectral gap  $\gamma = 1 - |\lambda_2|$  for a range of values of the lag parameter  $\tau$ .
10. By the arguments presented in Section 2.10 we expect that the spectral gap calculated from noisy data is “close to” the real spectral gap.



# 3 Bifurcations and Tipping Points

In this chapter we review and give an overview of some commonly considered one-parameter bifurcations. In Section 3.1 we recall what can be learned from the Jacobian of a dynamical system in the neighborhood of a fixed point. Section 3.2 list four bifurcations – the saddle-node, Hopf, pitchfork and transcritical bifurcations – that can give rise to critical transitions. We emphasize the saddle-node as this is relevant to the discussion in Section 3.3 and mention the remaining bifurcations for completeness. We analyze the double well model in Section 3.3 and show how time series generated with this model exhibit EWS in the case where transitions are caused by a saddle-node bifurcation resulting from slow parameter variations.

## 3.1 Linear Stability Analysis

Consider a smooth vector field  $\mathbf{f} : \mathbb{R}^n \rightarrow \mathbb{R}^n$

$$\dot{\mathbf{x}} = \mathbf{f}(\mathbf{x}) \tag{3.1.1}$$

that has a fixed point  $\mathbf{x}^*$  such that

$$\mathbf{f}(\mathbf{x}^*) = \mathbf{0}. \tag{3.1.2}$$

To examine the stability of  $\mathbf{f}(\mathbf{x})$  we expand  $\mathbf{f}$  around  $\mathbf{x}^*$  with the the Jacobian  $J(\mathbf{x}^*)$

$$\left[ \frac{\partial f_i}{\partial x_j} \Big|_{\mathbf{x}^*} \right]_{i,j=1,\dots,n} = J(\mathbf{x}^*). \tag{3.1.3}$$

Since  $d\mathbf{x}^*/dt = 0$  we obtain the linearized system for small  $\mathbf{y}$  as

$$\frac{d\mathbf{y}}{dt} = \mathbf{f}(\mathbf{x}^* + \mathbf{y}) \approx J(\mathbf{x}^*)\mathbf{y}; \tag{3.1.4}$$

when setting  $\mathbf{y}_0 = \mathbf{y}(t_0 = 0)$ , the linearized solution to Equation (3.1.4) is (Dijkstra 2013)

$$\mathbf{y}(t) \approx e^{tJ(\mathbf{x}^*)}\mathbf{y}_0. \tag{3.1.5}$$

Thus the eigenvalues of  $J(\mathbf{x}^*)$  determine the stability of solutions to Equation (3.1.1) close to  $\mathbf{x}^*$ . Specifically, let  $n_-, n_0, n_+$  the number of eigenvalues of  $J(\mathbf{x}^*)$  with negative, zero and positive real part, respectively. If  $n_0 = 0$  the fixed point is hyperbolic; for a hyperbolic fixed point, if  $n_- n_+ \neq 0$  the fixed point is a hyperbolic saddle; if  $n_0 = n_+ = 0$  then the fixed point is stable (Kuznetsov 1998, Theorem 1.5 and Definition 2.7).

### 3.2 Some One-Parameter Bifurcations

In this section we consider one-dimensional vector fields that depend on a parameter  $p$  so that  $\dot{x} = f(x; p)$ . We will examine four different bifurcations, each represented by their *normal form*, in the sense that any system exhibiting the same type of bifurcation at an equilibrium locally “looks like” the normal form in the neighborhood of that equilibrium.

In more detail, if a system undergoes one of these bifurcations at an equilibrium, then the state space and parameter space of that system are related to the state and parameter spaces of the normal form system by two simultaneous homeomorphisms, where the homomorphism of the parameter space preserves the direction of time; this is termed topological equivalence. We will not need greater detail in this thesis and refer the reader to Kuznetsov (1998, especially Section 2.4).

Kuehn (2011) examines one-parameter bifurcations and shows that the following give rise critical transitions:

- The saddle-node,
- The subcritical Hopf,
- The subcritical pitchfork, and
- The transcritical.

We focus our attention on the saddle-node and briefly examine the the remaining bifurcations.

#### 3.2.1 The Saddle-Node Bifurcation

The saddle-node bifurcation has the normal form (Strogatz 1994)

$$\dot{x} = p + x^2. \quad (3.2.1)$$

We apply the results from Section 3.1. The vector field  $f(x)$  in Equation (3.2.1) is

$$f(x; p) = \dot{x} = p + x^2 \quad (3.2.2)$$

so a fixed point  $x^*$  is given by

$$f(x^*; p) = 0 \Rightarrow x_{\pm}^* = \pm\sqrt{-p}. \quad (3.2.3)$$

We require the parameter  $p$  to be real so there are only fixed points for  $p \leq 0$ . The Jacobian of Equation (3.2.2) evaluated at a fixed point  $x^*$  is

$$\left. \frac{\partial f}{\partial x} \right|_{x^*} = 2x^* \quad (3.2.4)$$

and so  $x_-^*$  is stable while  $x_+^*$  is unstable. Next we examine what happens for a small perturbation  $y$  around the stable fixed point  $x_-^*$ . According to Equation (3.1.5)

$$y(t) \approx y(0)e^{2tx_-^*} = y(0)e^{-2t\sqrt{-p}}. \quad (3.2.5)$$

As the parameter  $p$  approaches 0, perturbations decay progressively slower – this is the phenomenon of *critical slowing down*<sup>1</sup> as defined in Nes and Scheffer (2007) and Scheffer et al. (2009) and mentioned in Chapter 1

When  $p$  approaches 0 from below,  $x_-^*$  and  $x_+^*$  collide in a *saddle-node* bifurcation leaving a half stable fixed point at the origin for  $p = 0$  (Figure 3.1). When  $p$  increases further, the fixed point disappears. When  $\partial f/\partial x|_{x^*} = 0$ , which happens when  $p = 0$  and thus  $x^* = 0$ , in general the linearization does not tell us anything about the stability of the fixed point (Strogatz 1994). The phase portrait of the saddle-node is shown in Figure 3.1.

In Figure 3.3 we show the bifurcation diagram of the saddle-node bifurcation as well as other bifurcations that give rise to critical transitions. This figure, along with Figure 3.4 shows the parameter value on the  $x$ -axis and the corresponding values of  $x^*$  (or  $r^*$  for the Hopf bifurcation) on the  $y$ -axis. Stable fixed points are shown as full lines while unstable fixed points are shown as dotted lines.

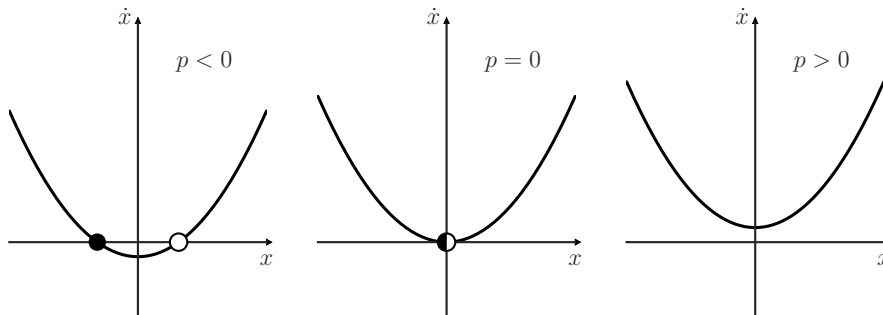


**Figure 3.1 | Phase portrait of the saddle-node bifurcation.** For  $p < 0$  there are two fixed points, one stable (filled) and one unstable (blank). At  $p = 0$  the fixed points collide in a saddle-node bifurcation, leaving a half stable fixed point at the origin; this disappears for  $p > 0$ . Compare with the bifurcation diagram in Figure 3.3a.

<sup>1</sup> We note that the definition is different in Strogatz (1994, p. 40) where critical slowing down is defined as *algebraic* rather than exponential decay.

### 3.2.2 The Hopf Bifurcation

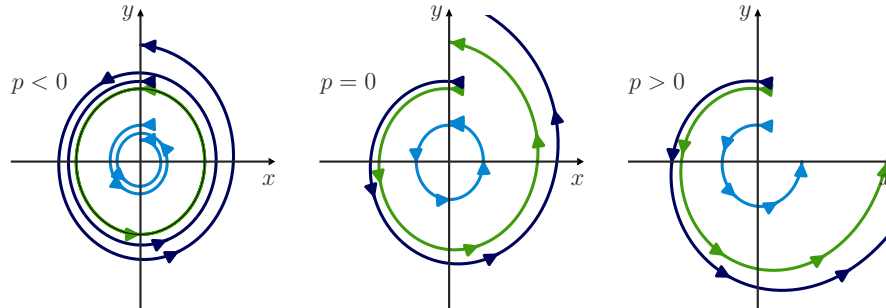


**Figure 3.2 | Sample trajectories of the subcritical Hopf bifurcation.** For  $p < 0$  the origin is stable and attracts trajectories with  $r < \sqrt{-p}$ , and there is an unstable limit cycle with  $r = \sqrt{-p}$  – the green curve is started here. The unstable limit cycle collides with the origin at  $p = 0$ , and  $r = 0$  becomes an unstable fixed point – compare with the bifurcation diagram in Figure 3.3b.

The Hopf bifurcation has the normal form (Kuznetsov 1998, Theorem 3.4)

$$\begin{pmatrix} \dot{x}_1 \\ \dot{x}_2 \end{pmatrix} = \begin{pmatrix} p & -1 \\ 1 & p \end{pmatrix} \begin{pmatrix} x_1 \\ x_2 \end{pmatrix} \pm (x_1^2 + x_2^2) \begin{pmatrix} x_1 \\ x_2 \end{pmatrix}, \quad (3.2.6)$$

where a plus sign in the last term gives rise to a subcritical Hopf and a minus sign a supercritical Hopf (Kuznetsov 2006). Equation (3.2.6) is easier to interpret in polar coordinates. Using a coordinate transformation from Perko (2001, Section 2.10) we arrive at (for  $r > 0$ ):

$$\begin{aligned} \dot{r} &= pr \pm r^3 \\ \dot{\theta} &= 1 \end{aligned} \quad (3.2.7)$$

where the plus and minus signs still represent the sub- and supercritical Hopf bifurcations, respectively.

### 3.2.3 The Transcritical and Pitchfork Bifurcations

Finally we mention the transcritical bifurcation

$$\dot{x} = px - x^2 \quad (3.2.8)$$

and the pitchfork bifurcation

$$\dot{x} = px + x^3 \quad (\text{subcritical}) \quad (3.2.9)$$

$$\dot{x} = px - x^3 \quad (\text{supercritical}). \quad (3.2.10)$$

Bifurcation diagrams for these are shown in Figures 3.3 and 3.4.

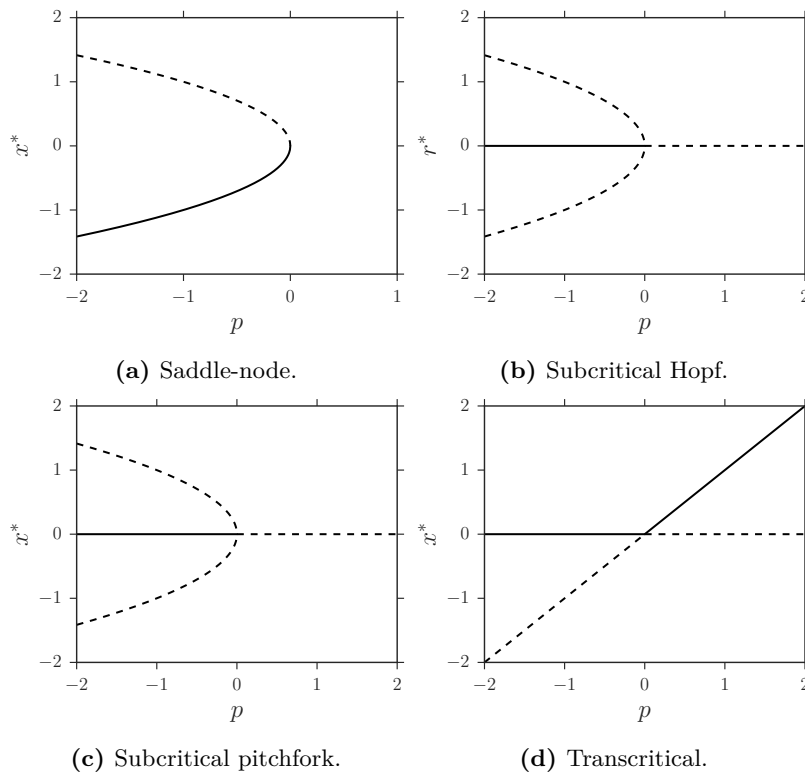


**Figure 3.3 | Bifurcation diagrams for some critical transitions.** Full lines represent stable fixed points, dotted lines unstable fixed points. These bifurcations give rise to critical transitions (Kuehn 2011). Note that the Hopf bifurcation in polar coordinates in **b**) is analogous to the pitchfork bifurcation in **c**). For the transcritical bifurcation in **d**), note that  $\dot{x} < 0$  for  $p > 0$  and  $x < 0$ , so trajectories initiated here will escape.

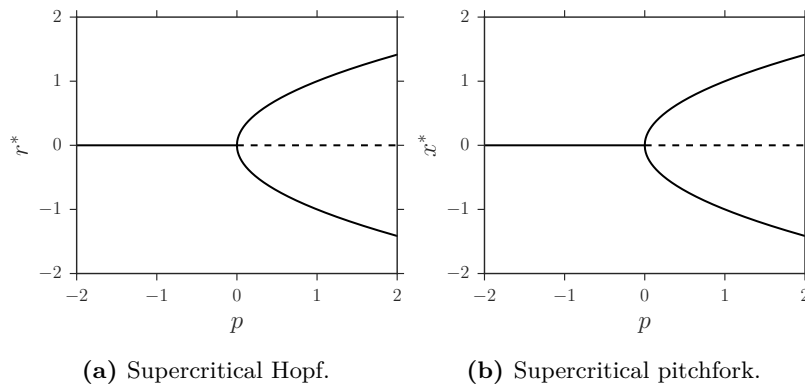


**Figure 3.4 | Bifurcation diagrams for some non-critical transitions.** Interpretation as Figure 3.3. When comparing these bifurcation diagrams with those shown in Figure 3.3 it is intuitively clear that the supercritical bifurcations – despite their names – do not give rise to critical transitions, as there are close stable fixed points on both sides of  $p = 0$ .

### 3.3 Bifurcations and Noise – Early Warning Signals

In this section we will analyze the double-well potential model presented in Section 1.3.1. In particular we show the increase in variance and lag-1 autocorrelation of a time series obtained from the model when it undergoes a bifurcation. The analysis presented here follows Ditlevsen and Johnsen (2010), and we add to their analysis by quantifying some of their results.

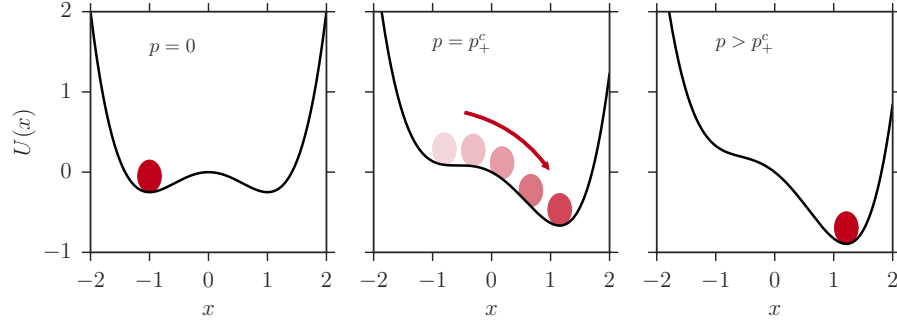


**Figure 3.5 | Sketch of the climate pseudo-potential.** A sketch of the climate pseudo-potential, Equation (3.3.1) for varying values of  $p$  where the system state is represented by the red disc initially positioned in  $x_-^*$ . The value of the bifurcation parameter  $p$  is increasing panel-wise from left to right. In the leftmost panel there are two fixed points  $x_-^*$  and  $x_+^*$  as well as the unstable fixed point  $x_u^*$  (see text). As the value of  $p$  is increased  $x_-^*$  and  $x_u^*$  collide and annihilate leaving only the distant attractor  $x_+^*$ . This chain of events constitutes a critical transition (Kuehn 2011).

The basic feature of the double-well potential model is a climate pseudo-potential of the form

$$U(x; p) = \frac{x^4}{4} - \frac{x^2}{2} - px; \quad (3.3.1)$$

Equation (3.3.1) gives rise to an SDE

$$dX_t = -\partial_x U(x; p)dt + \sigma dW_t \quad (3.3.2)$$

which is known as a Langevin equation (Gardiner 2009, p. 77). Equation (3.3.2) models a particle moving in a potential subject to random forcing.

The term “double-well” is immediately made clear when plotting Equation (3.3.1) as is done in Figure 3.5. The one-dimensional vector field generated by Equations (3.3.1) and (3.3.2) is

$$-\partial_x U(x; p) = -x^3 + x + p. \quad (3.3.3)$$

For varying values of  $p$  Equation (3.3.3) may have up to three fixed points as is visualized in the bifurcation diagram shown in Figure 3.6. Here, as previously, full lines indicate a stable fixed point and dotted lines an unstable one.

Denote – if they exist –  $x_-^*$  the stable fixed point for negative  $x$ -values,  $x_+^*$  the stable fixed point for positive  $x$ -values and  $x_u^*$  the remaining unstable fixed point. For  $p = 0$  in Equation (3.3.3) the fixed points are at  $(x_-^*, x_u^*, x_+^*) =$

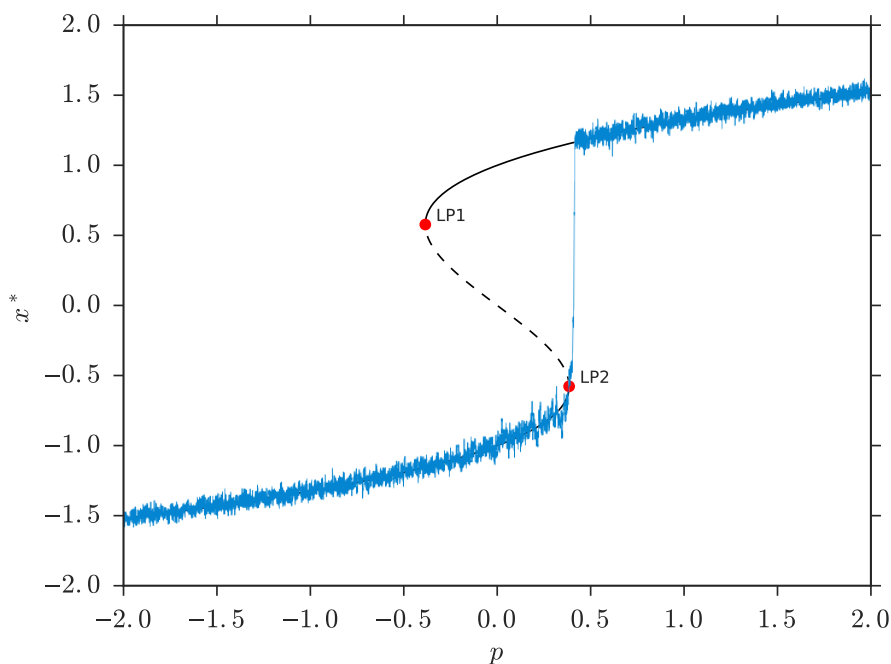


**Figure 3.6 | Time series from bifurcating system.** Bifurcation diagram of the vector field generated by the double-well potential via Equation (3.3.3) – stable fixed points correspond to the bottom(s) of the potential well in Figure 3.5. A full line denotes a stable fixed point  $x^*(p)$ , a dashed line an unstable fixed point. The  $p$ -coordinates of the points marked LP1 and LP2 are at  $p_{\pm}^c = \pm 2\sqrt{3}/9$ , respectively. Bifurcation diagram made by numerical continuation with PyDSTool (Clewley et al. 2007; Clewley 2012). The blue curve is a time series with varying  $p$  generated by numerically integrating Equation (3.3.2) with the EM method.

$(-1, 0, 1)$ . The model potentially undergoes two bifurcations at critical values of the parameter  $p$ ,  $p_{\pm}^c = \pm 2\sqrt{3}/9$  (Ditlevsen and Johnsen 2010).

When decreasing the value of  $p$  from 0 to  $p_-^c = -2\sqrt{3}/9$  we observe from Figure 3.6 that  $x_+^*$  and  $x_u^*$  collide and annihilate, leaving only  $x_-^*$  – the opposite situation happens when  $p$  is increase from 0 to  $p_+^c$  where  $x_-^*$  and  $x_u^*$  collide and annihilate. Both cases are instances of a saddle-node bifurcation (Berglund and Gentz 2006). Note that with the chosen notation,  $x_-^*$  disappears when  $p$  reaches  $p_+^c$  from *below* and vice versa.

It was claimed in Section 1.3.1 that variance and lag-1 autocorrelation increase before a bifurcation. To see how this is the case for the double-well system we consider a particle situated at the bottom of the potential well subjected to random forcing as in Equation (3.3.2). For small fluctuations we can regard the potential as parabolic (Ditlevsen and Johnsen 2010), namely by performing a Taylor expansion of Equation (3.3.3) and only keeping terms up to order  $x^2$ . Without loss of generality we can consider the case where the potential minimum is located at  $x = 0$ . Following Ditlevsen and Johnsen (2010) we will denote the parabolic potential approximation around a potential

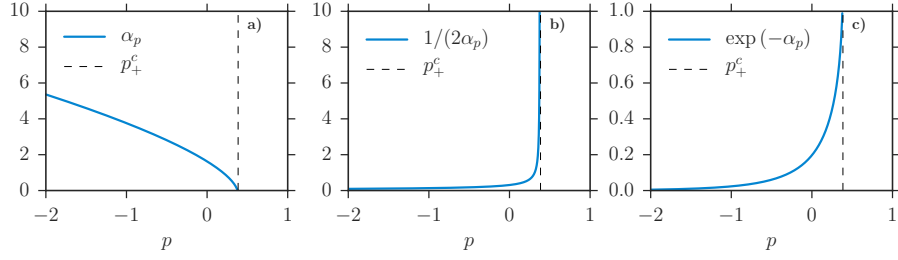


**Figure 3.7 | Theoretical bifurcation statistics.** **a)** Drift parameter, **b)** variance and **c)** autocorrelation for the quadratic potential approximation (Equation (3.3.5)) of the Langevin equation for the double-well potential model (Equation (3.3.1)). Results are obtained by a numerical Taylor expansion of  $U(x; p)$  around  $x_-(p)$  followed by application of Equations (3.3.6) and (3.3.7) with  $\sigma^2 = 1$  and  $\tau = 1$ .

minimum as  $U_p(x)$  so that

$$U_p(x) = \alpha_p \cdot x^2/2 \quad (3.3.4)$$

and such that the corresponding Langevin Equation (3.3.2) becomes

$$\begin{aligned} dX_t &= -\partial_x U_p(x) dt + \sigma dW_t \\ &= -\alpha_p X_t dt + \sigma dW_t. \end{aligned} \quad (3.3.5)$$

In Example 2.3 we calculated the variance and autocorrelation of the Ornstein-Uhlenbeck process and obtained Equations (2.3.21) and (2.3.27). These are repeated here for the readers convenience:

$$\text{Var}[X_t] \approx \frac{\sigma^2}{2\alpha}, \quad (3.3.6)$$

and

$$C(\tau) \approx e^{-\alpha\tau}. \quad (3.3.7)$$

When the bottom of the potential well “flattens” as happens before a bifurcation (see Figure 3.5) the value of  $\alpha_p$  will decrease from a positive value towards zero. For fixed values of  $\sigma$  and  $\tau$ , respectively, in Equations (3.3.6) and (3.3.7) we see that the potential flattening will cause an increase in variance and autocorrelation.

This statement is confirmed in Figure 3.7 where we show results of numerically performing a Taylor expansion of  $U_p(x)$  around  $x_-(p)$  for  $p \in [-2, p_+^c = 2\sqrt{3}/9]$ . We use  $\sigma^2 = 1$  and  $\tau = 1$  in Equations (3.3.6) and (3.3.7). Figure 3.7 a) shows the drift parameter  $\alpha_p$  as  $p_+^c$  is approached, clearly capturing the flattening of the potential minimum. Panels b) and c) show the variance and autocorrelation, respectively, and it is clear that both values increase.

We note that  $\sim 0.33\%$  of the values of  $\alpha_p$  in Figure 3.7 and the corresponding values of autocorrelation and variance closest to  $p_+^c$  were discarded on numerical grounds.

## 4 A Conceptual Model of Dansgaard-Oeschger Events

In this chapter we analyze time series generated with the double well model by calculating the spectral gap  $\gamma$  in sliding windows, yielding a series  $\gamma(t)$ . We plot  $\gamma(t)$  in the right endpoint of the window such that for a window of size  $W_s$ ,  $\gamma(t)$  is calculated from data in the interval  $(t - W_s, t)$ .

In addition to the 1-dimensional model presented in Section 3.3, we will make a simple extension to two dimensions in Section 4.1. This is done to show that transfer operator (TO) methods can be used on time series with two variables. In Section 4.2 we compare the results of computing  $\gamma(t)$  with the classical early warning indicators, variance and lag-1 autocorrelation.

When approximating  $\mathcal{L}_\tau$  by Markov matrices  $P_{ij}(\tau)$  there are several parameters that have to be chosen (Table 4.3). We end this chapter by varying these parameters and analyzing the results in Section 4.3.

### 4.1 1D and 2D Double Well Models

The one-dimensional double well (DW) model was introduced in Section 3.3 as Equations (3.3.1) and (3.3.2) that are repeated here for convenience. The climate pseudo-potential is

$$U(x; p(t)) = \frac{x^4}{4} - \frac{x^2}{2} - p(t)x; \quad (4.1.1)$$

and by using  $-\partial_x U(x; p(t))$  as the drift term in an SDE

$$dX_t = [-X_t^3 + X_t + p(t)] dt + \sigma dW_t. \quad (4.1.2)$$

I will refer to Equation (4.1.2) as the “1D double well”. The extension to two dimensions – the 2D double well – is constructed by adding a parabolic potential in the  $y$ -direction:

$$U(x, y; p(t)) = \frac{x^4}{4} - \frac{x^2}{2} - p(t)x + \frac{y^2}{2}. \quad (4.1.3)$$

Taking  $-\partial_x U(x, y; p(t))$  and  $-\partial_y U(x, y; p(t))$  as drift terms in an SDE as above leads to the system

$$\begin{aligned} dX_t &= -[-X_t^3 + X_t + p(t)] dt + \sigma_X dW_t, \\ dY_t &= -Y_t dt + \sigma_Y dW_t. \end{aligned} \quad (4.1.4)$$

Note that the bifurcation parameter  $p$  only enters in the equation for  $dX_t$  in Equation (4.1.4).

The parameters we use for integrating Equation (4.1.2) are shown in Table 4.1, and parameters used for integrating Equation (4.1.4) are shown in Table 4.2. For the 1-dimensional model, the noise level  $\sigma = 0.1$  for the bifurcation induced transition and  $\sigma = 0.25$  for the stochastic transition are the same as in Ditlevsen and Johnsen (2010). The noise level was increased slightly for the 2-dimensional model undergoing a stochastic transition in order to observe transitions in a reasonable timeframe.

Both systems are integrated with the EM method and down-sampled to  $\Delta t = 0.1$ , a step size comparable with the time step size in the ice core data we analyze in Chapter 5. The time series are then re-arranged so that the transition happens at  $t = 1500$ . We perform a linear detrending of the series in the interval  $0 \leq t \leq 1500$  and calculate variance, lag-1 autocorrelation and the spectral gap  $\gamma(t)$  for the detrended series up to time  $t = 1495$ . We mention that the Python package `statsmodels` is used for calculating the autocorrelation here and in the following (see Appendix B).

	Bifurcation	Stochastic Jump
$p(t)$	$t \cdot (2\sqrt{3}/9)/2000$	0
$\sigma$	0.1	0.25
$x_0$	-1	-1
EM time step $h$	0.001	0.001
Sampling time $\Delta t$	0.1*)	0.1*)

**Table 4.1 | 1D double well simulation parameters.** The simulations are shown in Figure 4.1 a) (bifurcation) and b) (stochastic jump). The time series are re-arranged so that the transitions happen at  $t = 1500$ . \*) Sampling time  $\Delta t = 0.1$  unless otherwise noted (see Figure 4.8).

## 4.2 Analysis of Data From the Double Well Models

### 4.2.1 1D Double Well Model

In Figure 4.1 a) and b) we show time series from the 1D double well model. In panel a) the model undergoes a bifurcation induced transition while panel b) shows stochastic transitions. There are 25 individual time series in each case.

The clear increases in both variance and lag-1 autocorrelation evident in panels c) and e) are absent in panels d) and f) as expected. The individual series are shown in grey while the ensemble means are in red.

Figure 4.1 also shows that it is unwise to trust an early warning indicator based on a *single* time series  $x(t)$ . One rebellious realization seen in panel a) (purple) causes a large increase in both variance and autocorrelation.

In Figure 4.2 the spectral gap  $\gamma(t)$  is computed for the same time series as shown in Figure 4.1 a) and b). The increase in lag-1 autocorrelation seen in Figure 4.1 c) corresponds to the decrease in  $\gamma(t)$  seen in the left panel of Figure 4.2; a decrease in  $\gamma(t)$  is expected to be accompanied by an increase in

	Bifurcation	Stochastic Jump
$p(t)$	$t \cdot (2\sqrt{3}/9)/2200$	0
$\sigma_X$	0.1	0.3
$\sigma_Y$	0.1	0.3
$X_0$	-1	-1
$Y_0$	0	0
EM time step $h$	0.001	0.001
Sampling time $\Delta t$	0.1	0.1

**Table 4.2 | 2D double well simulation parameters.** These parameters are used for integrating Equation (4.1.4), and the simulations are shown in Figure 4.4 a) for the bifurcation case and b) for the stochastic case. Again we re-arrange the data so the transitions happen at  $t = 1500$ . Note that the noise is slightly increased in the stochastic jump case compared to the one-dimensional case ( $\sigma_X = \sigma_Y = 0.3$  here vs  $\sigma = 0.25$  in Table 4.1). A slightly longer time series was generated in the two-dimensional case ( $t_{\text{bif}} = 2200$  here vs.  $t_{\text{bif}} = 2000$  in Table 4.1) prior to re-arranging the time series, since the spread in “jumping time” was larger in the two-dimensional case.

Standard Values	
Window size $W_s$	200
Grid size, 1D	50 rows
Grid size, 2D	$15 \times 15$ (rows $\times$ columns)
Lag time $\tau$ in $\mathcal{L}_\tau$	1

**Table 4.3 | Standard spectral gap calculation parameters.** We show the results of varying these parameters in the one-dimensional case in Section 4.3.

autocorrelation (Chekroun et al. 2014). This decrease in  $\gamma(t)$  is absent for the time series resulting from a stochastic transition.

Note that there are several sudden drops in the values of  $\gamma(t)$  in Figure 4.2. This happens when the transition matrices  $P_{ij}(\tau)$  computed in each window do not represent irreducible Markov chains, as shown in Figure 4.3. In this figure we show all the series  $\gamma(t)$  in Figure 4.2 where  $\gamma(t)$  drops to zero.

We determine, for the transition matrix in each window, whether it is irreducible or not. This is done using the function `is_strongly_connected()`<sup>1</sup> from the Python library `NetworkX` (Hagberg et al. (2008) – see also see Appendix B).

The occurrence of reducible Markov chains requires a careful application of the TO methods. When summarizing the results concerning mixing rate of Markov matrices in Section 2.8.3 we assumed that the Markov matrix in question was irreducible. For this reason we check how many of the transition matrices in each window used to compute  $\gamma(t)$  satisfy this assumption – the

<sup>1</sup> When using this function, the transition matrix is considered as a directed graph. A strongly connected graph then corresponds to a transition matrix representing an irreducible Markov chain as follows: for an irreducible Markov chain (strongly connected graph) it is possible to get from any state (node) to any other state (node).

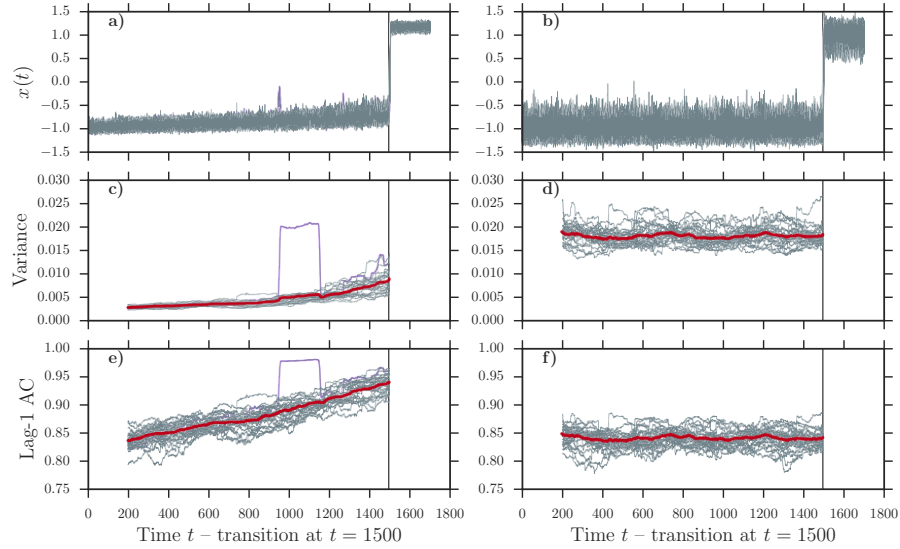


**Figure 4.1 | Time series, observed variance and lag-1 autocorrelation for the 1D double well model.** 25 time series  $x(t)$  generated by integrating Equation (4.1.2) with parameters as described in Table 4.1 for the case of **a)** a bifurcation and **b)** a stochastic transition. **c), e)**: rolling variance and lag-1 autocorrelation (grey) and mean values (red) calculated from the time series in **a)** after linear detrending. The window size is 200 time units, corresponding to 2000 data points. The values are calculated up to  $t = 1495$ , just before the transition. Both the variance and lag-1 AC are seen to increase when approaching the bifurcation. **d), f)**: as c) and e) but for the stochastic transition. There is no increase in either indicator before the transition.

results are shown in Table 4.4.

Data	# Points ( $\gamma$ )	% Irreducible	% Aperiodic
Figure 4.2, bifurcation	32525	98.4%	99.1%
Figure 4.2, stochastic	32525	98.0%	98.9%
Figure 4.5, bifurcation	13010	93.9%	96.2%
Figure 4.5, stochastic	13010	87.9%	93.5%

**Table 4.4 | Percentage of transition matrices representing irreducible / aperiodic Markov chains.** Values are shown for the resulting transition matrices in each sliding window where  $\gamma(t)$  is shown in Figures 4.2 and 4.5. Aperiodic transition matrices were also identified using NetworkX, with the function `is_aperiodic()` (Hagberg et al. (2008) and Appendix B).

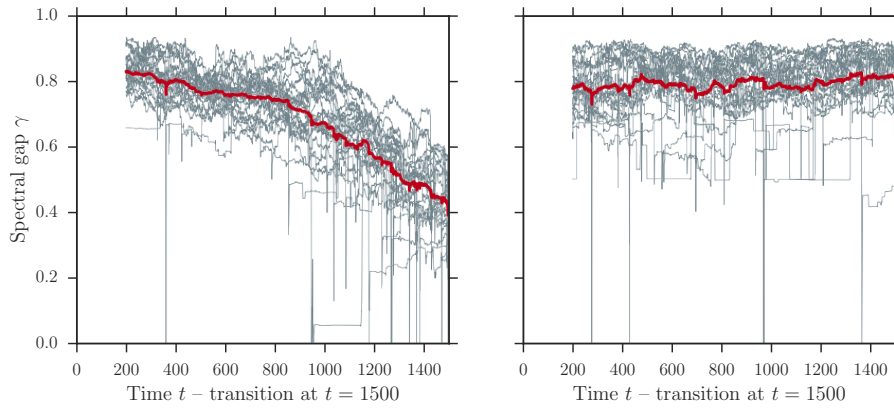


**Figure 4.2 | Spectral gap for the 1D double well model.** The parameters for calculating  $\gamma(t)$  are as in Table 4.3. Grey curves are individual  $\gamma(t)$  series, red curves are ensemble means. **Left:** spectral gap  $\gamma(t)$  calculated for the data in Figure 4.1 a) (bifurcation). There is a clear decrease in  $\gamma(t)$  corresponding to a slower decay of the ACF.  $\gamma(t)$  is calculated up to  $t = 1495$  (vertical lines). **Right:** as the left figure but for time series from the stochastic transitions in Figure 4.1 b). Note the sudden drops in  $\gamma(t)$  seen in both series. Since  $\gamma = 1 - |\lambda_2|$ , these drops correspond to the appearance (and disappearance) of a subdominant eigenvalue with magnitude close to unity.

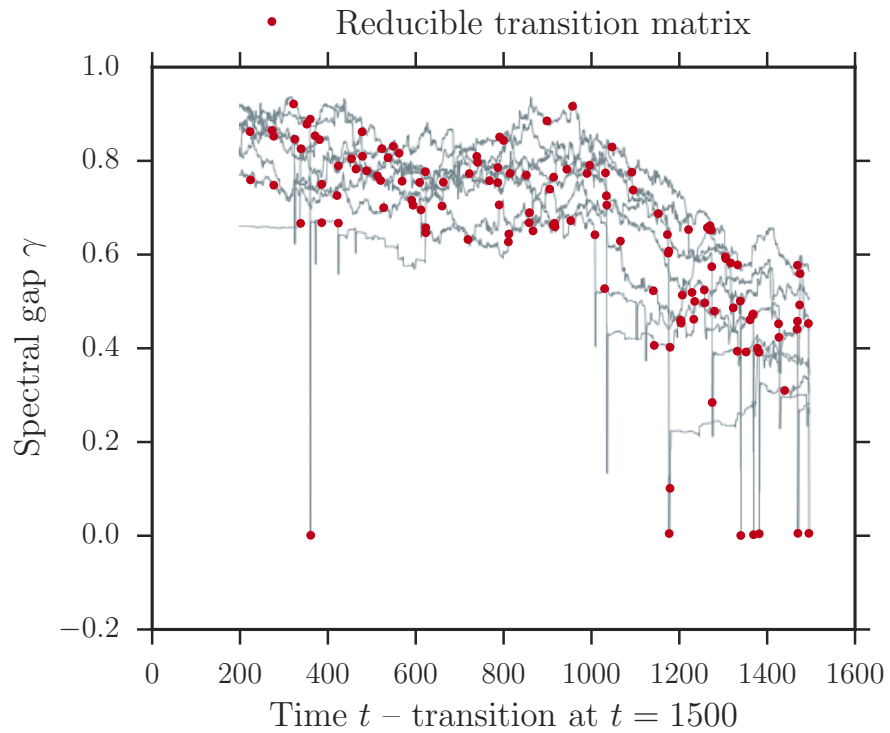


**Figure 4.3 | Fluctuations in calculated values of the spectral gap.** The grey lines are the subset of the curves shown in Figure 4.2 where the values of  $\gamma(t)$  suddenly drops. This happens because the transition matrices  $P_{ij}(\tau)$  calculated to approximate  $\mathcal{L}_\tau$  and in turn  $\gamma(t)$  at these instances are reducible; they may thus have more than one unity eigenvalue. The red dots show where reducible transition matrices occur. For all the values of  $\gamma(t)$  shown in Figure 4.2 ( $25 \times 1301 = 32525$  values, both for the stochastic case and the bifurcation case) this happens less than 2% of the time (Table 4.4).

### 4.2.2 2D Double Well Model

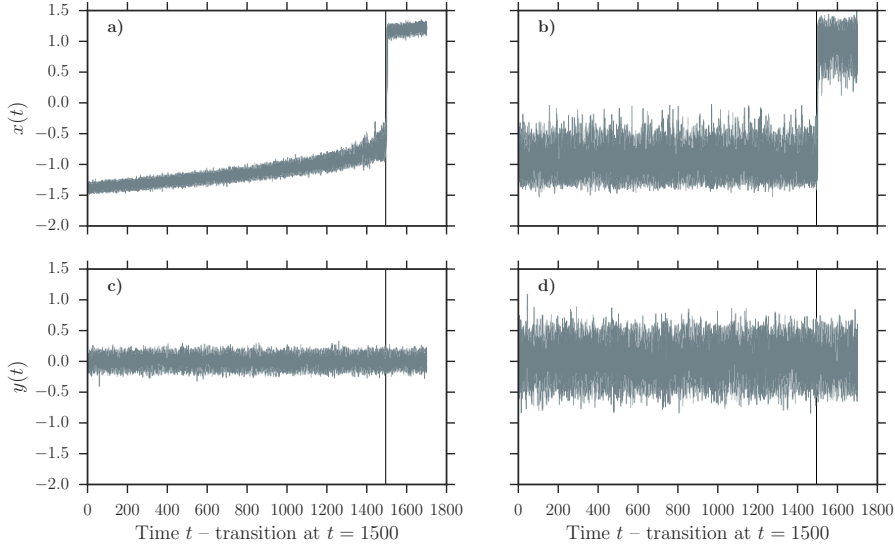


**Figure 4.4 | Time series from the 2D double well model.** Time series  $x(t)$  and  $y(t)$  generated by integrating Equation (4.1.4) with the EM method using the parameters in Table 4.1. **a), c)**: 10 realizations of the model undergoing a bifurcation. **b), d)**: same as a) and c) but for the model exhibiting a stochastic jump. Note that  $x(t)$  and  $y(t)$  are independent so the bifurcations evident in  $x(t)$  in a) are not seen in  $y(t)$  in c).

Figure 4.4 show data generated with the 2D double well model (Equation (4.1.3)) using the parameters in Table 4.2. In this case there are 10 individual time series of  $(x(t), y(t))$  in both the stochastic and bifurcation cases. Rolling variance, lag-1 autocorrelation and spectral gap obtained from the time series are shown in Figure 4.5. Variance and autocorrelation are calculated separately for  $x(t)$  and  $y(t)$  while both time series were used simultaneously for computing  $\gamma(t)$ . There is a clear decrease in  $\gamma(t)$  before the approach to the bifurcation in Figure 4.5 e) while there is no increase in the stochastic case.

The results in Figure 4.5 indicate that computing the spectral gap is useful to distinguish between the two transition types, also in the case of two variables.

### 4.2.3 Decorrelation time and spectral gap for the 1-dimensional double well

In Section 2.7.2 we derived an approximate relation between the spectral gap  $\gamma$  and the decorrelation time  $\tau_C$ ; we repeat that result here for convenience:

$$\tau_C \approx -\frac{\tau}{\ln(1 - \gamma)}. \quad (4.2.1)$$

It is illustrative to compare this to the decorrelation time obtained by more familiar means. While it seems most natural to obtain  $\tau_C$  from the ACF and

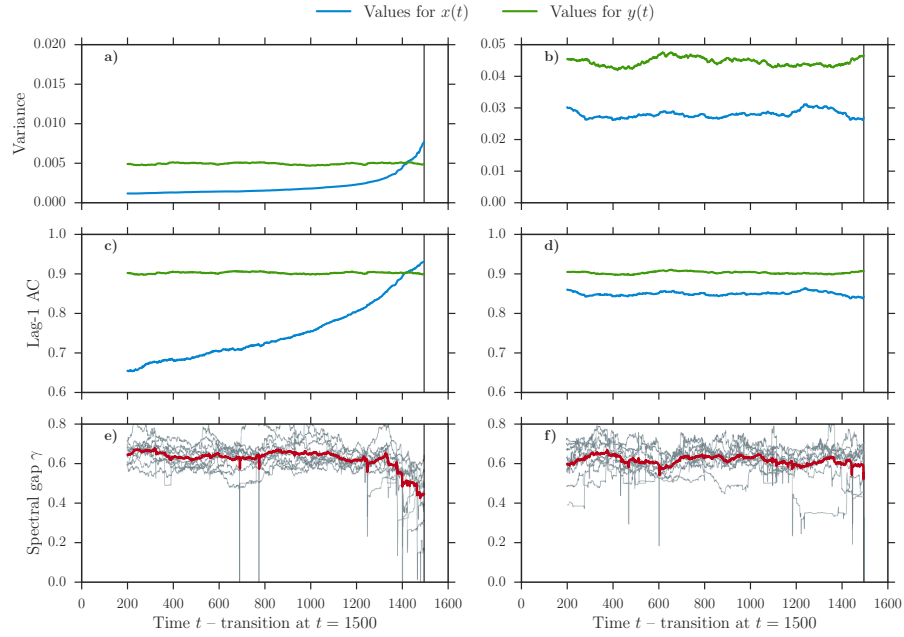


**Figure 4.5 | Variance, lag-1 AC and spectral gap for the 2D double-well model.** All values are calculated up to  $t = 1495$  with a window size of 200 time units corresponding to 2000 data points. **a), b)** variance and **c), d)** lag-1 AC for the bifurcation time series (left column) and the stochastic time series (right column). Variance and lag-1 AC are calculated separately for  $x(t)$  (blue) and  $y(t)$  (green). They are only early warning signals in the series for  $x(t)$  in **a)** and **c)**. **e)**: the spectral gap for the bifurcation series is seen to decrease before the transition. **f)**: there is no early warning before the stochastic transition.

eg. finding the lag  $k$  where the ACF crosses  $1/e$ , this has proven numerically unreliable. Instead we fit an AR(1)-model

$$X_k = \phi X_{k-1} + \epsilon_k \quad (4.2.2)$$

to the data and estimate  $\tau_C$  from this. Equation (4.2.2) has ACF for  $k \geq 0$  (Box et al. 2008)

$$R(k) = \phi^k = e^{k \ln \phi}, \quad (4.2.3)$$

giving a decorrelation time  $\tau_C = -1/\ln(\phi)$ . The results are shown in Figure 4.6; full lines show mean  $\tau_C$  for 100 time series using the two different methods, and the shaded regions show  $\pm$  one standard deviation. The agreement is reasonable, although the  $\tau_C$  values computed from the spectral gap does have larger variability.

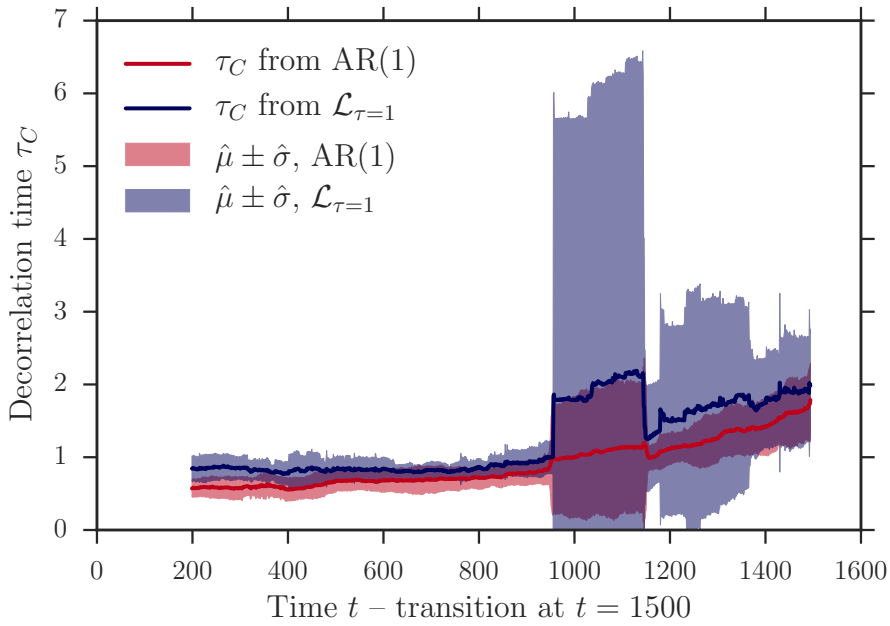


**Figure 4.6 | Decorrelation time from spectral gap and AR(1) model.** The red curve denotes the decorrelation time calculated by fitting an AR(1)-model in windows of 200 time units to 100 separate time series from the 1D double well undergoing a bifurcation. Shaded regions denote  $\pm$  one standard deviation. The blue curve is the result of computing the spectral gap and using Equation (4.2.1). Before performing the calculation, values of  $\gamma(t) < 0.01$  (less than 0.1% of 32525 values) were dropped for numerical reasons. In this case the time series were down-sampled to  $\Delta t = 1$  to use identical data for both methods. It is clear that the variability is larger for the  $\tau_C$  estimated by the TO method.

### 4.3 Parameter Variation for the Spectral Gap Computations

Figures 4.7 to 4.10 all concern the data presented in Figure 4.1 a) and b). We will vary the parameters for calculating  $\gamma(t)$  presented in Table 4.3 one by one and investigate the results.

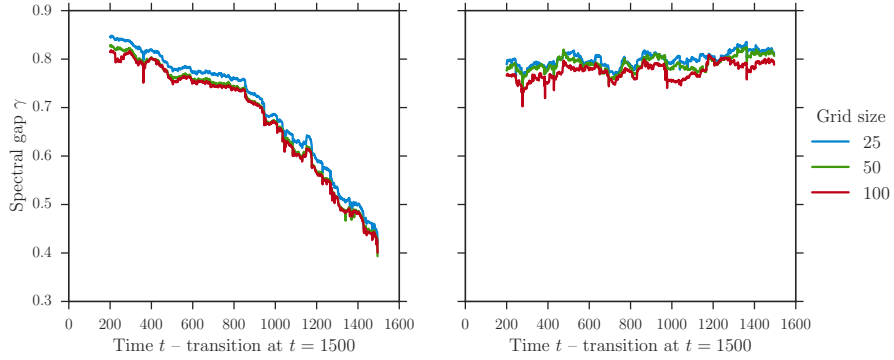


**Figure 4.7 | Mean spectral gap  $\gamma(t)$  for 25 1D double well time series with varying grid size** Results of varying the grid size in the calculation of  $\gamma(t)$  for the data shown in Figure 4.1 a) and b). Only the mean values of  $\gamma(t)$  are shown for clarity. It is seen that varying the grid size does not appreciably change the results presented in Figure 4.2.

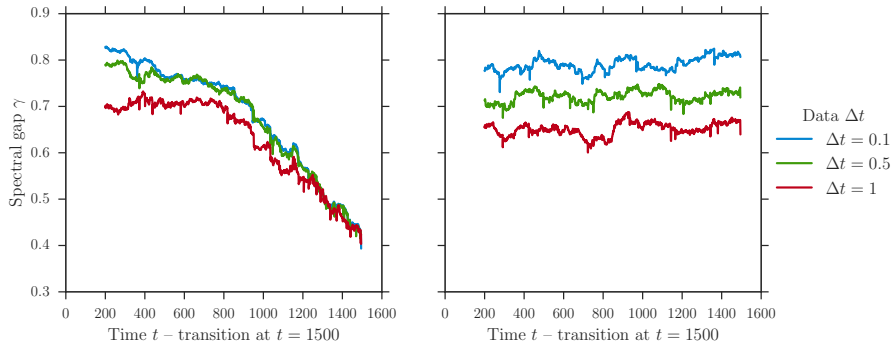


**Figure 4.8 | Mean spectral gap  $\gamma(t)$  for 25 1D double well time series with varying data  $\Delta t$ .** The original data is on a time scale with  $\Delta t = 0.1$  and is here down sampled to  $\Delta t = 0.5$  and  $\Delta t = 1$ , respectively. For larger  $\Delta t$  the computed values of  $\gamma(t)$  are lower, corresponding to quicker decay of the ACF. We interpret this as due to a larger amount of small scale variation being resolved for a finer temporal resolution. Comparing the two figures, it is clear that we still see the approach to the transition in the bifurcating case on the left.

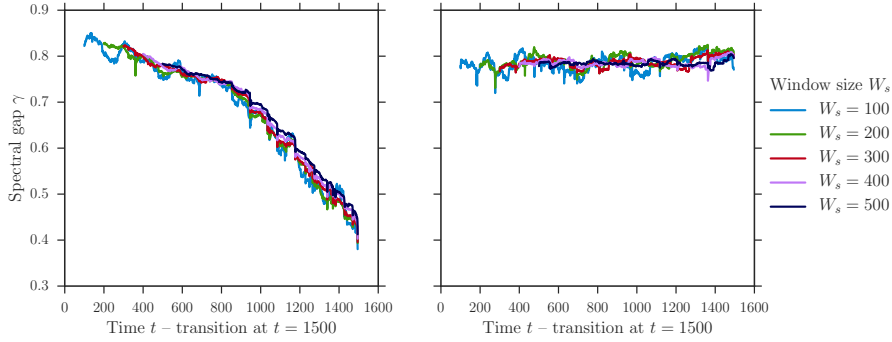


**Figure 4.9 | Mean spectral gap  $\gamma(t)$  for 25 1D double well time series with varying window size.** For the rather large variations in window size presented here the results are practically similar, indicating that the choice of window size is not likely to have a large influence on the results.

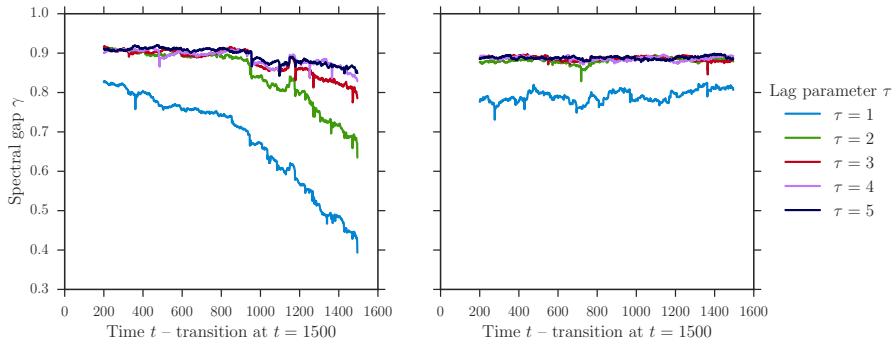


**Figure 4.10 | Mean spectral gap  $\gamma(t)$  for 25 1D double well time series with varying lag  $\tau$ .** A much larger effect on the spectral gap computations are seen in the choice of the lag  $\tau$ . This is expected from the discussion in Section 2.8.2, as a longer lag  $\tau$  disregards the fast fluctuations in the data. Most importantly, the fact that the general structure is seen for several values of  $\tau$  is encouraging.



# 5 Ice Core Data Analysis

We begin this chapter by summarizing the interpretation of the three climate proxies  $[\text{Ca}^{2+}]$ ,  $[\text{Na}^+]$  and  $[\text{NH}_4^+]$ , denoting the concentration of calcium, sodium and ammonium ions in the ice core, respectively. As variations in  $\delta^{18}\text{O}$  led to the discovery of the DO events, this climate proxy is also introduced. We will however not use this variable in the following time series analysis since it has a significantly lower temporal resolution.

In Section 5.2 we introduce a mapping from ice core depth to age. Creating a time scale for the data will consist of two steps. First we map ice core depth to ice age (and thus data age), and second we interpolate the resulting time series to equidistant time steps. Next we address the question of which parts of the time series to analyze. Since we are concerned with possible changes in dynamics leading up to DO events we naturally focus on these. However, some parts of the time series contain too many missing values and will have to be excluded.

In Section 5.3 the results of analyzing the data using the TO framework are described. On an ensemble level we find no evidence of a change in dynamics before DO events using this method. The justification for computing the TO in sliding windows is assessed in Section 5.4 by varying the parameters used and determining the fraction of the transition matrices representing irreducible Markov chains. We give a brief discussion of the results in Section 5.5.

## 5.1 Climate Proxies

$[\text{Ca}^{2+}]$ ,  $[\text{Na}^+]$  and  $[\text{NH}_4^+]$  are commonly studied when attempting to reconstruct past climate from ice core records (eg. Legrand and Mayewski (1997)).  $[\text{Ca}^{2+}]$  and  $[\text{Na}^+]$  reflect changes in atmospheric circulation happening under DO events that affect continental (calcium) and marine (sodium) conditions, while  $[\text{NH}_4^+]$  records changes in vegetation patterns (Legrand and Mayewski 1997).

For each climatic state the ion concentrations have approximately log-normal distribution (Steffensen et al. 2008; Gfeller et al. 2014; Rasmussen et al. 2014) and are studied on a natural log scale as in Lenton et al. (2012a). Data from the Last Glacial period is shown in Figure 5.1.

### 5.1.1 $\delta^{18}\text{O}$

On Earth there are three naturally occurring stable isotopes of oxygen ( $^{16}\text{O}$ ,  $^{17}\text{O}$  and  $^{18}\text{O}$ ) and two naturally occurring stable isotopes of hydrogen (H and

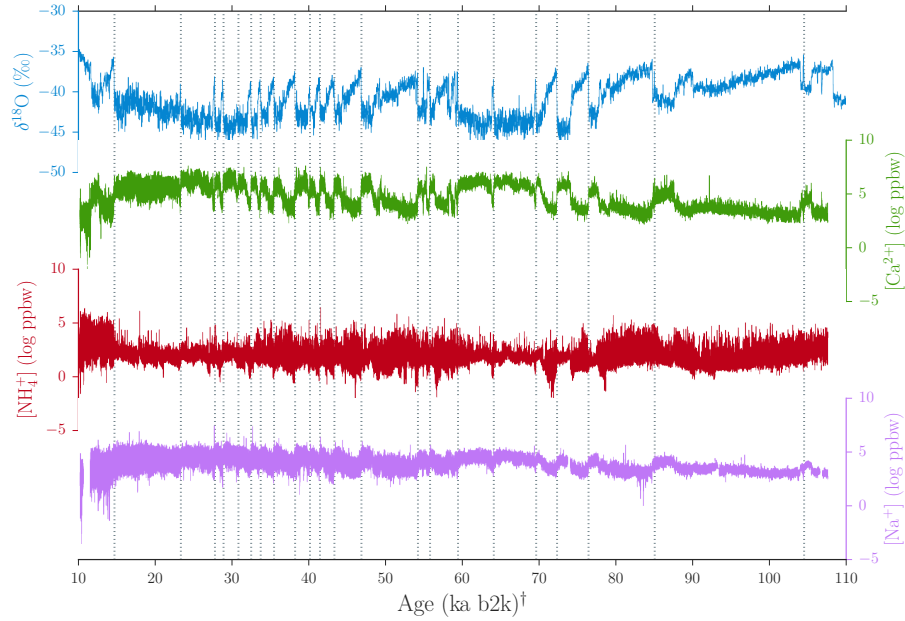


**Figure 5.1 | Greenland ice core data from the Last Glacial.** This period occurred from  $\sim 11.6$  to  $\sim 116$  ka b2k (IPCC 2013). The data is from the NGRIP ice core (NGRIP 2004).  $\delta^{18}\text{O}$  (in ‰, see Equation (5.1.1)) has a temporal resolution of 20 years while  $[\text{Ca}^{2+}]$ ,  $[\text{Na}^+]$  and  $[\text{NH}_4^+]$  have spatial resolutions of 1mm. The latter results in varying temporal resolution (see Section 5.2.3). Note the log scale for the ion data that shows the (natural) logarithm of concentration in parts per billion, weight (ppbw). The vertical lines mark 22 DO events initially selected for analysis (see Section 5.2.4).  $\dagger$ Greenland Ice Core Chronology 2005, model extended (GICC05modelext) age scale (Wolff et al. 2010).

D). This results in 9 different *isotopologues*; the two most common are  $\text{H}_2^{16}\text{O}$  (99.73098%) and  $\text{H}_2^{18}\text{O}$  (0.199978%) (Galewsky et al. 2016).

$\delta^{18}\text{O}$  is a measure of the content of  $^{18}\text{O}$  relative to  $^{16}\text{O}$  in water. This has units of permille (‰) and is defined as (Galewsky et al. 2016)

$$\delta^{18}\text{O} = \frac{(^{18}\text{O}/^{16}\text{O})_{\text{sample}} - (^{18}\text{O}/^{16}\text{O})_{\text{standard}}}{(^{18}\text{O}/^{16}\text{O})_{\text{standard}}} \times 1000. \quad (5.1.1)$$

The term “standard” in Equation (5.1.1) refers to Vienna standard mean ocean water (V-SMOW) where  $(^{18}\text{O}/^{16}\text{O})_{\text{V-SMOW}} = 2.0052 \times 10^{-3}$  (Galewsky et al. 2016).

Imagine that we follow a parcel of water vapor that has evaporated from the ocean and travels northward. As the water vapor cools some vapor will condense. Since the vapor pressure of  $\text{H}_2^{16}\text{O}$  is slightly higher than that of  $\text{H}_2^{18}\text{O}$  this condensation process will favor  $\text{H}_2^{18}\text{O}$ , leading to *isotopic fractionation*; the water vapor reaching the poles will thus be depleted in  $^{18}\text{O}$  (Brook 2013). The further north and further up the water travels before it condenses, the lower  $\delta^{18}\text{O}$ -value – this explains that  $\delta^{18}\text{O}$  in Greenland snow decreases

with increasing altitude, increasing northern latitude and decreasing surface temperature (Johnsen et al. 1989).

Dansgaard (1964) showed the relationship between local annual mean surface air temperature and local annual mean  $\delta^{18}\text{O}$  levels, with colder temperatures leading to decreasing values of  $\delta^{18}\text{O}$ . This makes  $\delta^{18}\text{O}$  useful as a proxy for site temperature at the time of snow deposition (Steffensen et al. 2008; Vinther and Johnsen 2013; Rasmussen et al. 2014). The relationship between  $\delta^{18}\text{O}$  and site temperature is approximately linear (Dansgaard 1964; Johnsen et al. 1989; Brook 2013). In order not to over-simplify the picture we mention that other processes are involved as well. In the upper part of the ice core there is diffusion of water vapor causing the  $\delta^{18}\text{O}$ -signal to be smeared out (Vinther and Johnsen 2013). Also present in Greenland ice cores  $\delta^{18}\text{O}$  is an annual signal that persists for most of the Holocene, enabling the identification of individual years in the ice cores. This signal does not continue into the last glacial due to low accumulation rates (Vinther and Johnsen 2013).

### 5.1.2 Calcium

Calcium in Greenland ice cores comes mainly from terrestrial dust (Hutterli et al. 2007; Rasmussen et al. 2014) with the primary source being Asian deserts (Steffensen et al. 2008).  $[\text{Ca}^{2+}]$  measured in Greenland ice is thus a proxy for atmospheric availability of the dust itself as well as the conditions that move the dust from Asia to Greenland (Steffensen et al. 2008). The availability of dust is mediated by soil moisture, whereas higher wind speed will increase the transport. Both conditions likely contributed to higher Greenland  $[\text{Ca}^{2+}]$  during the Last Glacial as compared to today (Kreutz and Koffman 2013).

Since changes in  $\delta^{18}\text{O}$  and  $[\text{Ca}^{2+}]$  are close in time they are thought to be linked to the same atmospheric changes (Steffensen et al. 2008; Rasmussen et al. 2014). It has been shown that the logarithm of  $[\text{Ca}^{2+}]$  in Greenland ice is anti-correlated with  $\delta^{18}\text{O}$  (Yiou et al. 1997, Eq. 5).

Furthermore,  $[\text{Ca}^{2+}]$  in Greenland ice cores exhibit seasonal variation with peaks in spring (Legrand and Mayewski 1997). On a GS-to-GI scale,  $[\text{Ca}^{2+}]$  time series show “an excellent signal-to-noise ratio” (Rasmussen et al. 2014) with large changes in magnitude between GS and GI, leading to its widespread use in the study of the dynamics of DO-cycles (eg. Ditlevsen (1999), Steffensen et al. (2008), and Livina et al. (2010)).

### 5.1.3 Sodium

Concentration of sea salts decrease during DO-events (Wolff et al. 2010) and in general  $[\text{Na}^+]$  is higher during glacial than interglacial conditions (Kreutz and Koffman 2013). Sodium ions comes primarily from sea salt and changes less than  $[\text{Ca}^{2+}]$  at DO events (eg. Steffensen et al. (2008)), also evident in Figure 5.7.

The causes leading to increased  $[\text{Na}^+]$  during winter and glacial conditions are not yet entirely understood, but both atmospheric conditions as well as sea ice extent are expected to play a role (Steffensen et al. 2008; Kreutz and Koffman 2013). In Greenland (and Antarctic) ice cores,  $[\text{Na}^+]$  increases in winter due to increased storminess over the oceans and correspondingly larger transport (Legrand and Mayewski 1997).

In colder climate conditions, even though the ice sheets had a greater extent and thus to a larger degree separated the ice sheets from the ocean, there is an increase in  $[\text{Na}^+]$ , possibly due to a more effective transport (Legrand and Mayewski 1997).

#### 5.1.4 Ammonium

Ammonium originates from soil and vegetation emissions, but also forest fires (Brook 2013; Wolff et al. 2010).  $[\text{NH}_4^+]$  is higher in ice from GSs than from GIs (Wolff et al. 2010). Ice volume as well as orbital parameters influence  $[\text{NH}_4^+]$  in Greenland ice cores due to the effect on biological activity, and thus emission (Brook 2013). In terms of clear interpretation and signal to noise ratio  $[\text{NH}_4^+]$  may be the weakest of the three variables presented.

No seasonal cycle is observed in Antarctic  $[\text{NH}_4^+]$  but a strong summer maximum is seen in Greenland due to the latter’s proximity to major continents (Legrand and Mayewski 1997).

## 5.2 Data and Methods

### 5.2.1 NGRIP CFA Data

We will analyze  $[\text{Ca}^{2+}]$ ,  $[\text{Na}^+]$  and  $[\text{NH}_4^+]$  from the NGRIP ice cores (NGRIP 2004). The data is obtained by continuous flow analysis (CFA) and contains measurements as a function of depth in 1 mm intervals (Ruth et al. 2003; Bigler 2004). CFA enables high resolution and deals effectively with possible contamination of the ice core, since – during the continuous melting – the outside is discarded, and only the inner part of the core is used. For an overview of this method, see eg. Röthlisberger et al. (2000), Ruth et al. (2003), and Breton et al. (2012).

An example of the raw data along with an interpolated age scale (to be described in Section 5.2.3) is shown in Table 5.1.

NGRIP Depth (m)	Age (ka b2k)	$[\text{Ca}^{2+}]$ (ppbw)
2450.000	62443.750	471.3892
2450.001	62443.875	457.8362
2450.002	62444.000	446.3019
2450.003	62444.125	437.5937
2450.004	62444.250	428.4819
2450.005	62444.375	420.1682
2450.006	62444.500	419.3330

**Table 5.1 | Example NGRIP CFA data.** The table shows NGRIP CFA data depth (left) and the result of linearly interpolating the age between GICC05modelext age points (Section 5.2.3). On the right we show an example of the  $[\text{Ca}^{2+}]$  data. Only the middle column is a result of the present study – the two outer columns show raw data. It is important to note that the interpolated age does *not* allow an interpretation along the lines of “62440.250 ka b2k  $\approx$  month of March, 60440 years B.C.” – the timing is too uncertain for any interpretation like this (Section 5.2.8).

### 5.2.2 GICC05modelext Time Scale

The CFA data is measured as a function of depth. To map from ice core depth to data age we will use the Greenland Ice Core Chronology 2005 (GICC05) time scale<sup>1</sup> available from CIC (2010). This scale is based on annual layer counting and extends to 60 ka b2k (Vinther et al. 2006; Rasmussen et al. 2006; Andersen et al. 2006; Svensson et al. 2008), and the model extension GICC05modelext to 122 ka b2k (Wolff et al. 2010).

The GICC05modelext time scale contains age before year 2000 (b2k) in 20 year intervals and the corresponding depth – an example of data can be seen in Table 5.2. When using the GICC05modelext time scale we will refer to it with a dagger, as in “Age (ka b2k)<sup>†</sup>”.

NGRIP Depth (m)	Age (ka b2k) <sup>†</sup>	MCE (years)
2373.37	56.42	2425.0
2373.63	56.44	2427.0
2373.91	56.46	2429.0
2374.16	56.48	2430.0
2374.41	56.50	2430.0
2374.67	56.52	2431.0
2374.94	56.54	2432.0

**Table 5.2 | NGRIP depth and GICC05modelext time scale (raw data).** There is a depth point for every 20 years. Until 60 ka b2k, the age is assigned by annual layer counting and by matching the data to volcanic events. Maximum counting error (MCE) measures counting uncertainty in the sense that an uncertain year is counted as  $0.5 \pm 0.5$  years (Rasmussen et al. (2006) – see also Section 5.2.8). <sup>†</sup>GICC05modelext time scale.

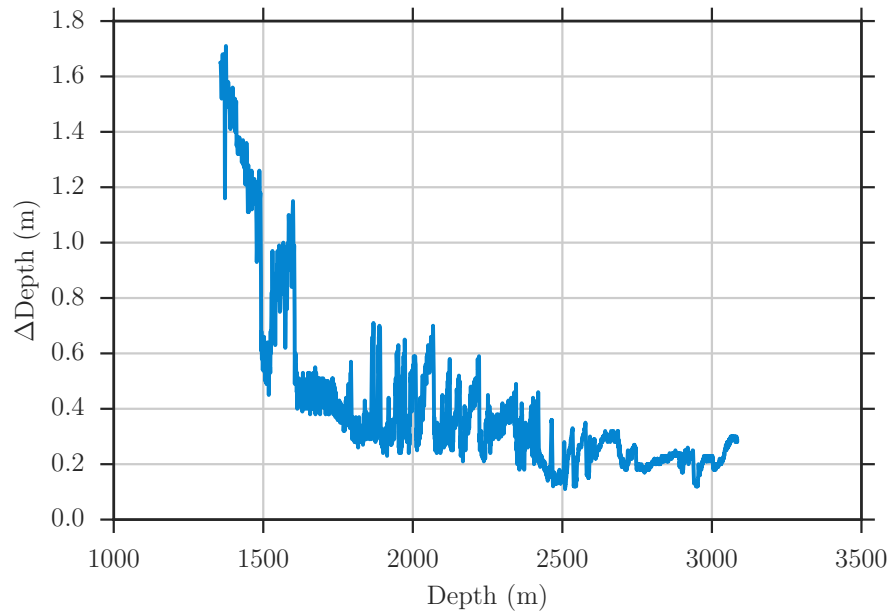
If snow remains on the ice sheet, older snow will be compressed over the course of time as new snow falls on top. In general, this means that a piece of ice core corresponding to 20 years of accumulation will be shorter the older it is. This is evident in Figure 5.2 where the depth differences between consecutive data points in the GICC05modelext series are shown.

Figure 5.2 also shows how many CFA data points there will be for every (depth, age) point in the GICC05modelext time scale. If, for example,  $\Delta$ Depth between two (depth, age) points is 1m we will have 1000 CFA data points between the two endpoints, since the CFA data has a resolution of 1mm. The corresponding age for each CFA data point will be the result of linear interpolation between the two GICC05modelext endpoints.

### 5.2.3 Interpolation, pt. I - Mapping Depth to Age

The first step is to match the CFA data depth to depth in the GICC05modelext time scale. This is accomplished by piecewise linear interpolation between the (depth, age) data points in GICC05modelext using Python’s `numpy.interp()` (Walt et al. 2011) – see Table 5.1 and Figure 5.3 for examples.

<sup>1</sup> For an overview of the work leading to the GICC05 time scale, see CIC (2016).



**Figure 5.2 |  $\Delta\text{Depth}$  in the GICC05modelext time scale.** The CFA data has a spatial resolution of 1mm and it is our objective to put this on the GICC05modelext time scale. This figure shows the spatial resolution of the GICC05modelext scale where an age estimate is available for each data point in 20 year intervals.

#### 5.2.4 Selection of Greenland Interstadials for Analysis

In order to detect any potential changes in the system dynamics we require a time series of reasonable length *before* the transition. We use the list of GI and GS periods and the corresponding nomenclature from Rasmussen et al. (2014) and initially select events by requiring that 1) there should be at least 500 years of data prior to the event to analyze and 2) each GI should be directly preceded by a GS so that the chosen events correspond to transitions from GS to GI, ie. a DO event. The resulting list of events is presented in Table 5.3. We see that the shortest time series obtained is actually 640 years long, corresponding to the time between GS-10 and GI-9.

#### 5.2.5 Interpolation, pt. II - Equidistant Time Steps

In order to simplify time series analysis we interpolate the data to equidistant time steps. It is desirable to have a time scale that is as highly resolved as possible while avoiding “upsampling” of the data, i.e. sampling the data at a finer resolution than what is available. Upsampling potentially introduces a dependence between consecutive data points that may be absent in the original data (Mudelsee 2010, pp. 22–24). As we saw in Figure 5.2, ice from the lower part of the ice core is compressed. Thus 1mm of ice (as is the measuring interval in the CFA data) will correspond to longer and longer time spans.

To choose a reasonable time step  $\Delta t$  we investigate the time difference

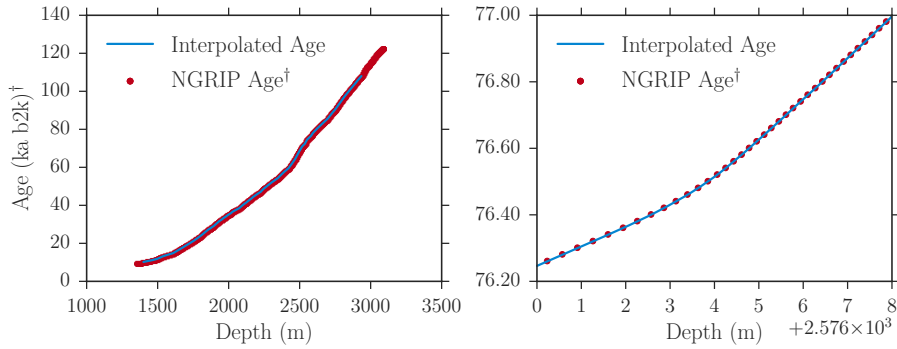


**Figure 5.3 | Interpolated CFA data age.** The data age is a result of piecewise linear interpolation of the GICC05modelext time scale to the 1mm intervals contained in the CFA data. **Left:** Interpolated age for the entire CFA dataset. **Right:** Example of a subset of the age scale. †GICC05modelext time scale.

in the data for each event. This is shown in Figure 5.4 where the values of  $\Delta t$  in the time series from the transitions in Table 5.3 are shown. The left panel of Figure 5.4 shows cumulative histograms of  $\Delta t$  where all time series with  $\max(\Delta t) > 0.1$  years are shown in color. Note that the time scale has been flipped as compared to Figure 5.1; the time scale  $t$  in the right panel of Figure 5.4 shows time progressing from left to right with the series aligned so that all events happen at  $t = 640$ . It is evident that a value of  $\Delta t = 0.2$  years is coarse enough to avoid upsampling in all cases, while choosing  $\Delta t = 0.1$  years is feasible for some events.

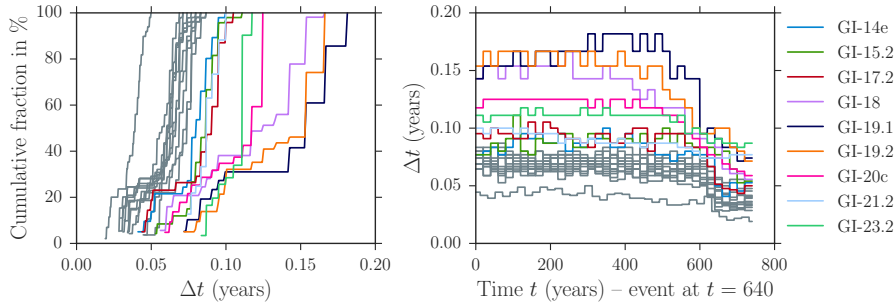


**Figure 5.4 | Interpolated  $\Delta t$  in data.** **Left:** Cumulative histogram of  $\Delta t$  of the interpolated data age scale for data 640 years prior and 100 years after the events in Table 5.3. Grey curves have maximum  $\Delta t < 0.1$  years, colored curves maximum  $\Delta t < 0.2$  years. **Right:**  $\Delta t$  as a function of time for the same events as on the left.

Period	Age (ka b2k) <sup>†</sup>	Previous Period	$\Delta$ Age (years) <sup>†</sup>	Notes
GI-1e	14.692	GS-2.1a	2788	a), b)
GI-2.2	23.340	GS-3	4200	b)
GI-3	27.780	GS-4	820	a), b)
GI-4	28.900	GS-5.1	1700	b)
GI-5.1	30.840	GS-5.2	1200	b)
GI-5.2	32.500	GS-6	860	a), b)
GI-6	33.740	GS-7	1000	b)
GI-7c	35.480	GS-8	1100	b)
GI-8c	38.220	GS-9	1680	b)
GI-9	40.160	GS-10	640	b)
GI-10	41.460	GS-11	780	b)
GI-11	43.340	GS-12	940	a), b)
GI-12c	46.860	GS-13	1480	a), b)
GI-14e	54.220	GS-15.1	680	a)
GI-15.2	55.800	GS-16.1	700	a)
GI-17.2	59.440	GS-18	4400	a)
GI-18	64.100	GS-19.1	5300	a)
GI-19.1	69.620	GS-19.2	760	a)
GI-19.2	72.340	GS-20	1760	a)
GI-20c	76.440	GS-21.1	1320	a)
GI-21.2	85.060	GS-22	2540	a)
GI-23.2	104.520	GS-24.1	920	a)

**Table 5.3 | List of Dansgaard-Oeschger events.** The naming and dating of onsets of periods are from Rasmussen et al. (2014). The interpretation is as follows: a transition from stadial GS-2.1a to interstadial GI-1e occurred at 14.692 ka b2k. Prior to that transition Greenland had experienced stadial conditions for 2788 years. Timing uncertainty is  $\pm 20$  years (corresponding to one data point in the GICC05modelext time scale) for all transitions except GI-1e ( $\pm 4$  years) and GI-5.1 ( $\pm 40$ – $60$  years) (Rasmussen et al. 2014, Table 2). Notes; **a)**: Any section of consecutive missing values is shorter than 10 years (see Figure 5.6). **b)**: interpolation to  $\Delta t = 0.1$  years feasible without upsampling (see Figure 5.4). <sup>†</sup>GICC05modelext time scale.

### 5.2.6 Missing Values

The time series presented in Section 5.2.5 were interpolated to  $\Delta t = 0.1$  years and  $\Delta t = 0.2$  years. We will have to consider that the data contains missing values or not a numbers (NaNs), and the most straightforward way to treat this is a further linear interpolation of the missing values. An example of this approach using toy data is shown in Figure 5.5. It is evident that this approach to handling missing data will only work if the amount of missing values in the data is not too high.

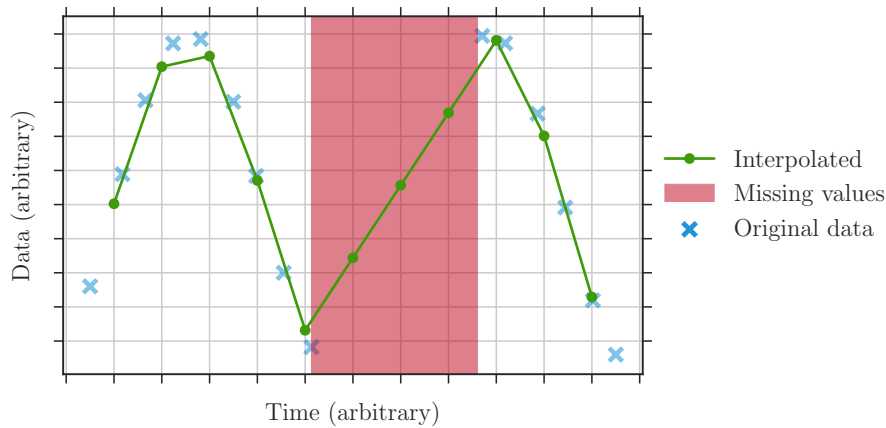


**Figure 5.5 | Illustration of the interpolation procedure.** The original data is on a non-equidistant time scale and has missing values. The resulting interpolated data has no missing values and the time spacing is equidistant; however, this method is only reasonable if the number of missing values is low.

Figure 5.6 shows the cumulative fraction of NaNs in the  $[\text{Ca}^{2+}]$ ,  $[\text{Na}^+]$  and  $[\text{NH}_4^+]$  time series for all the events listed in Table 5.3. The highlighted time series represent time series where the length of the intervals containing consecutive NaNs are larger than 10 years.

It is especially evident that several of the  $[\text{Na}^+]$  time series contain large intervals with consecutive missing values. This is possibly a consequence of different measurement techniques for  $[\text{Na}^+]$  (absorption spectrometry) on the one hand and  $[\text{Ca}^{2+}]$ ,  $[\text{NH}_4^+]$  (fluorescence spectrometry) on the other (Röthlisberger et al. 2000).

The events highlighted in the middle and lower panel of Figure 5.6 will thus be excluded from our analysis in order to avoid artifacts from the interpolation procedure. Events *not* highlighted in Figure 5.6 are marked a) in Table 5.3 and will form our dataset in the remainder of this chapter, unless otherwise specified.

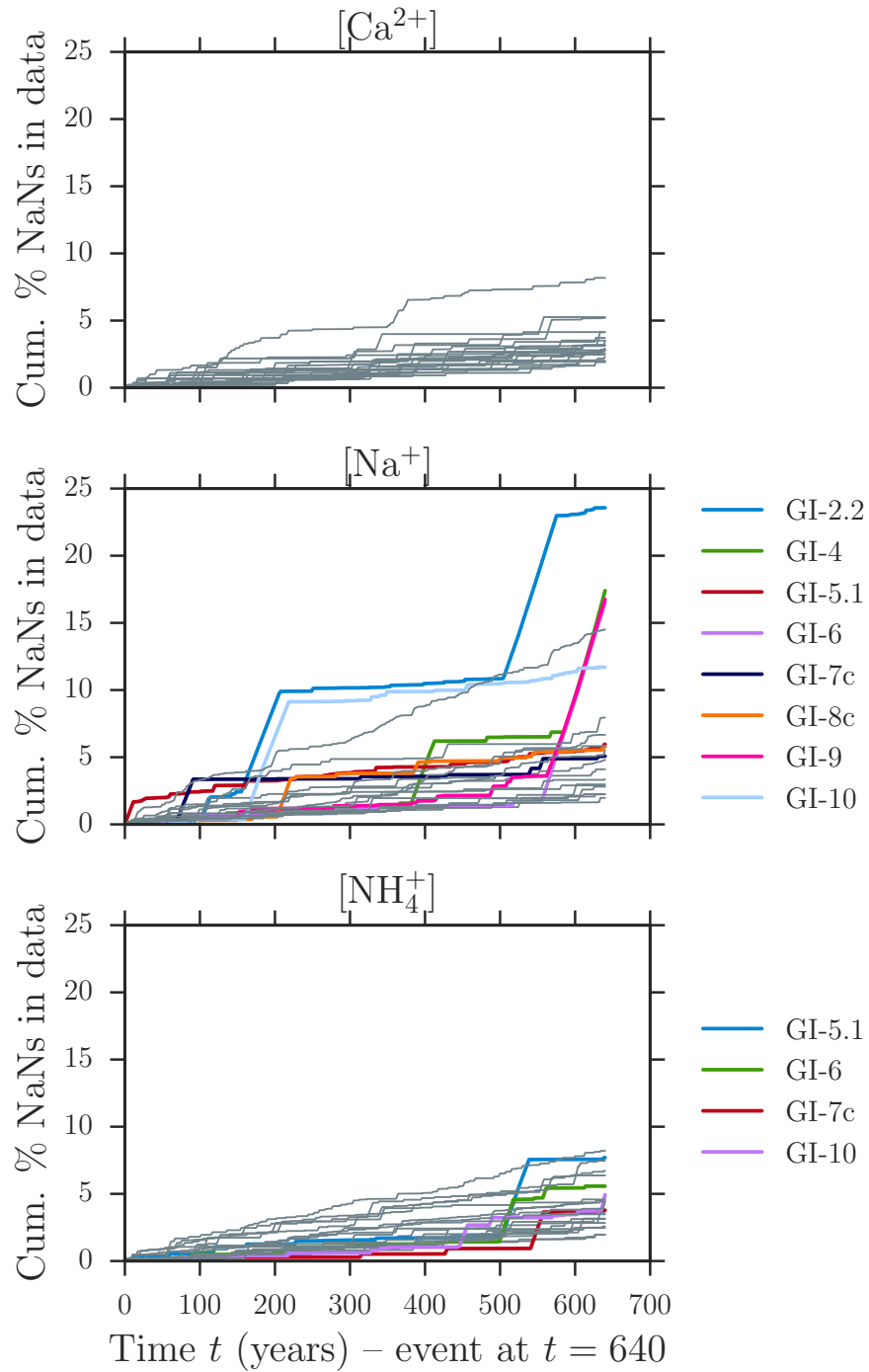


**Figure 5.6 | Consecutive missing values.** Colored curves denote data series with more than 10 years of consecutive missing data. 10 years corresponds to 5% of a window size of 200 years.

### 5.2.7 Example Data

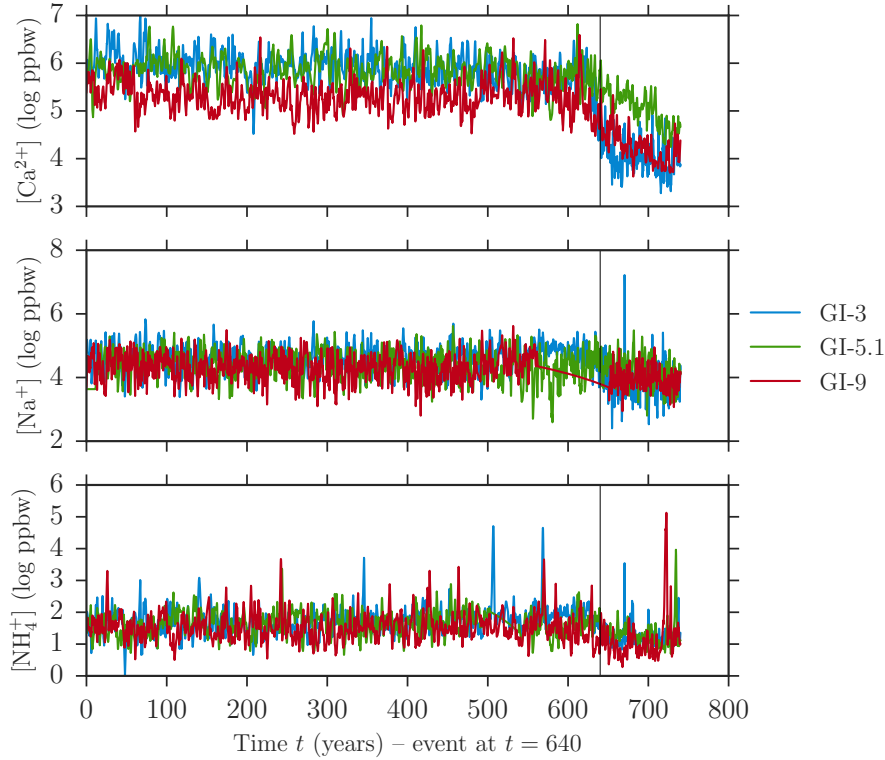


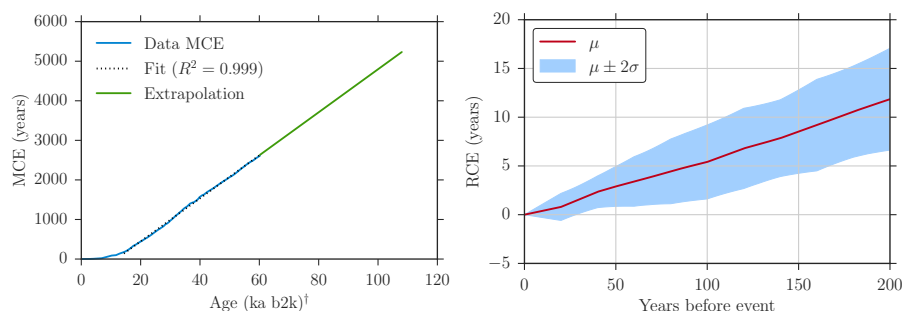
**Figure 5.7 | Example NGRIP data.** Data  $\Delta t = 0.2$  years. GI-3 is an example of a “nice” time series with only a few missing values. As noted in Table 5.3 the timing of GI-5.1 has a larger uncertainty ( $\pm 40$ -60 years) than most of the other events ( $\pm 20$  years). The  $[\text{Ca}^{2+}]$  time series in the top panel illustrates this larger uncertainty. GI-9 has a large fraction of consecutive missing  $[\text{Na}^+]$  values around the event. The middle panel shows the result of linearly interpolating missing  $[\text{Na}^+]$  values – clearly the gap is too large to justify this approach, leading to the exclusion of GI-9.

### 5.2.8 Timing Uncertainty – Maximum and Relative Counting Error (MCE & RCE)

There are three sources of timing or dating uncertainty we will have to take into account:

1. the uncertainty in timing the events themselves,
2. the MCE,
3. the uncertainty in the CFA system used to obtain the data.

Our objective will be to obtain a “data timing uncertainty”  $\delta t$  with the following interpretation: if we observe a change in the system dynamics at  $\delta t$  before the



(a) MCE in the NGRIP data (see Table 5.2) and linear extrapolation.

(b) Mean relative counting error (see Equation (5.2.2)) before DO events.

**Figure 5.8 | Maximum and mean relative counting error.** **Left:** The MCE is given up to 60.2 ka b2k (at a depth of 2428.78 m). The MCE is approximately linear from 14.35 ka b2k onwards and we use the corresponding values for the fit. **Right:** Mean  $\mu$  and  $\pm$  two standard deviations of relative counting error (RCE) up to 200 years before the DO events shown in Table 5.3. <sup>†</sup>GICC05modelext time scale.

events or earlier, we can be confident that we are not merely observing artifacts introduced by timing error.

First we take into account the uncertainty in timing the events. The 22 DO events listed in Table 5.3 have an uncertainty of  $\pm 20$  years, except for GI-5.1 that has an uncertainty of  $\pm 40$ – $60$  years and GI-1e that has an uncertainty of  $\pm 4$  years. GI-5.1 was excluded based on the discussion in Section 5.2.6. For this reason we take the event timing uncertainty to be  $\pm 20$  years for all the events, or

$$\delta_{\text{event}} = 20. \quad (5.2.1)$$

As we saw in Table 5.2 the GICC05 time scale comes with an uncertainty. Every uncertain year is counted as  $0.5 \pm 0.5$  years, so  $N$  uncertain layers will lead to an MCE of  $N \times 0.5$  (Andersen et al. 2006). The MCE is given up to 60.2 ka b2k. To assign an age uncertainty to data older than this we will extrapolate the MCE to cover all the data. This is shown in Figure 5.8a. As a linear function fits the MCE very well, this will be used for extrapolation.

For a time  $t_b$  years prior to an event we define the relative counting error (RCE) as the difference between the MCE  $t_b$  years *before* the event and the MCE *at* the event:

$$\text{RCE}_{\text{event}}(t_b) = \text{MCE}(\text{age}_{\text{event}} + t_b) - \text{MCE}(\text{age}_{\text{event}}) \quad (5.2.2)$$

The RCE is computed for all 22 events listed in Table 5.3. The mean  $\mu$  and  $\mu \pm 2\sigma$  where  $\sigma$  is the standard deviation of the resulting RCE are shown in Figure 5.8b. As we must observe a change minimum 20 years before an event (see Equation (5.2.1)) we are interested in the RCE 20 years prior to events. A reasonable choice would be to take the mean RCE plus two standard deviations as a  $\delta\text{RCE}$  (see Figure 5.8):

$$\delta\text{RCE} = \mu_{\text{RCE}}(20) + 2\sigma_{\text{RCE}}(20) = 2.2. \quad (5.2.3)$$

The CFA system can be expected to have an uncertainty of  $\pm 1$  cm (Röthlisberger et al. 2000). The maximum age difference for a depth difference of 1 cm in the CFA data (before interpolating to equidistant  $\Delta t$ ) is 1.82 years leading to

$$\delta\text{CFA} = 1.82. \quad (5.2.4)$$

There is no reason to assume that  $\delta\text{CFA}$  is correlated with  $\delta\text{event}$  or  $\delta\text{RCE}$ . If we assume that  $\delta\text{event}$  and  $\delta\text{RCE}$  are correlated then (see eg. Taylor (1982))

$$\delta t = \sqrt{(\delta\text{CFA})^2 + (\delta\text{event} + \delta\text{RCE})^2} = 22.3; \quad (5.2.5)$$

if we assume  $\delta\text{event}$  or  $\delta\text{RCE}$  are uncorrelated

$$\delta t = \sqrt{(\delta\text{CFA})^2 + (\delta\text{event})^2 + (\delta\text{RCE})^2} = 20.2 \quad (5.2.6)$$

A conservative approach is to take the value from Equation (5.2.5) and round it up to 23 years. Thus if we observe a change in the system dynamics at least  $\delta t = 23$  years before the events we can be confident that we in fact are observing a change in system dynamics rather than an artifact of dating error.

### 5.3 Analysis Using the Transfer Operator

First we present results of analyzing time series from the 14 events marked a) in Table 5.3 separately for  $[\text{Ca}^{2+}]$ ,  $[\text{Na}^+]$  and  $[\text{NH}_4^+]$ . Next we perform analyses using two variables; first using  $[\text{Ca}^{2+}]$  and  $[\text{Na}^+]$  and then using  $[\text{Ca}^{2+}]$  and  $[\text{NH}_4^+]$ . The reason for including  $[\text{Ca}^{2+}]$  in both analyses is that  $[\text{Ca}^{2+}]$  exhibits the strongest climate signal (cf. Section 5.1).

The analyses are carried out using time series interpolated to  $\Delta t = 0.2$  years, and we use a window size of 200 years. For the one variable analyses we divide the data space into 50 boxes and approximate the transfer operator  $\mathcal{L}_\tau$  with lag  $\tau = 1$  year. For the two-variable analyses, the grid resolution is  $15 \times 15$  and was chosen to reduce the fraction of transition matrices that represent reducible Markov chains, as in Chapter 4. Choosing a resolution of  $15 \times 15$  results in about 90% irreducible Markov chains – this is summarized in Table 5.4.

In Section 5.4 we explore the effect of varying the lag  $\tau$ , the number of boxes, the window size and the temporal resolution of the data  $\Delta t$ .

#### 5.3.1 One Variable Analyses

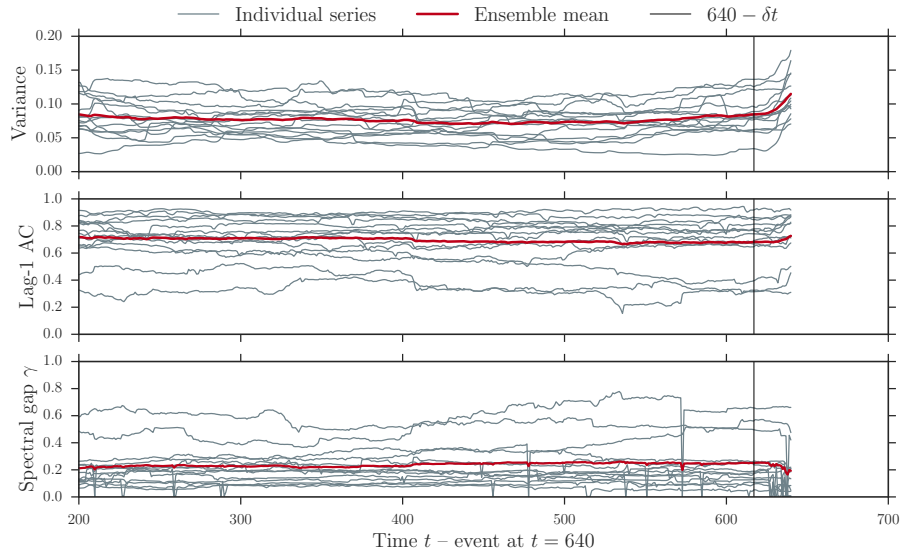


**Figure 5.9 | Spectral gap, variance and lag-1 autocorrelation for 14  $[\text{Ca}^{2+}]$  time series.** Grey curves show the computed quantities for the individual events, red curves show the ensemble means. Apart from a slight increase in variance there is no increase in either indicator. Data  $\Delta t$  is 0.2 years, and the window size is 200 years. As computed values are plotted at the right endpoint of the interval the first values appear at  $t = 200$ . The vertical black line shows  $t_{\text{event}} - \delta t$  that is,  $t = 627$ .

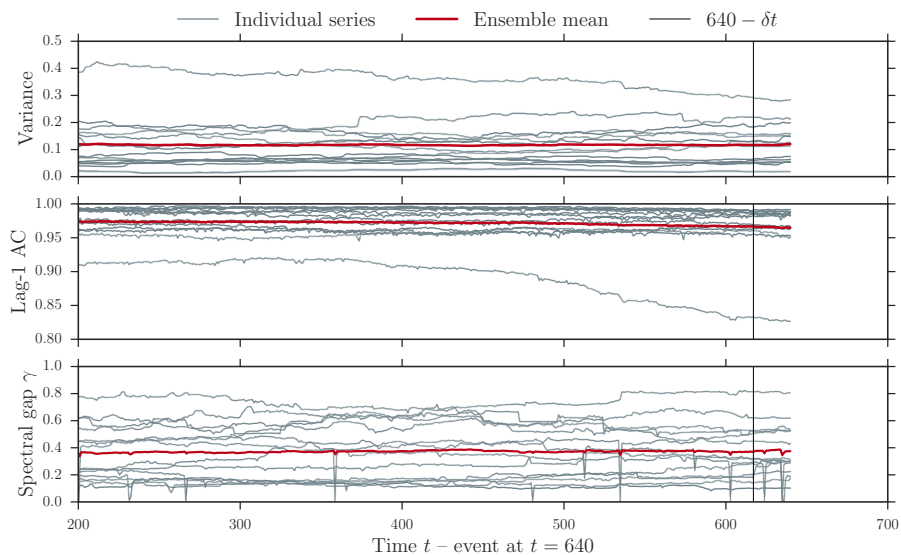


**Figure 5.10 | Spectral gap, variance and lag-1 autocorrelation for 14  $[\text{Na}^+]$  time series.** Interpretation as Figure 5.9. All three indicators are practically constant. The outlier in the two upper panels is GI-1e.

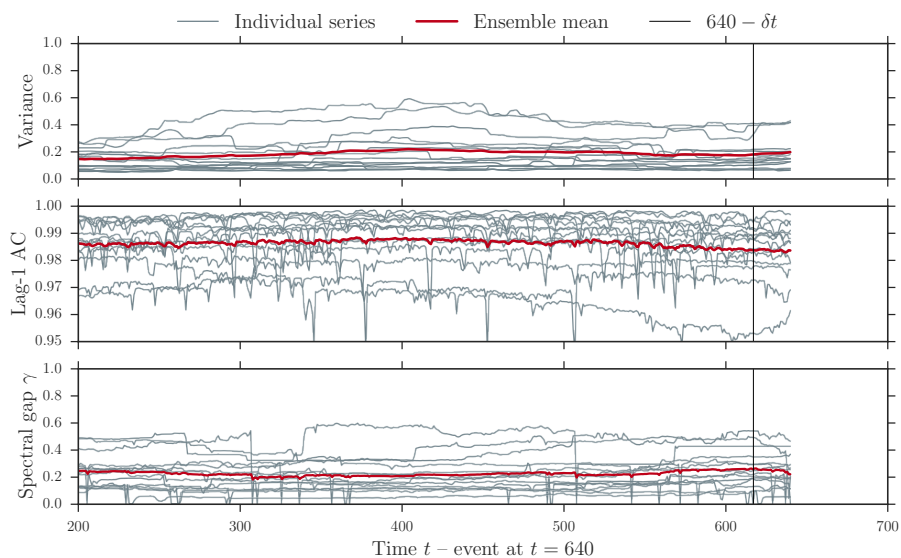


**Figure 5.11 | Spectral gap, variance and lag-1 autocorrelation for 14  $[\text{NH}_4^+]$  time series.** Interpretation is as Figures 5.9 and 5.10. The picture is generally the same; no obvious change is observed in either indicator.

### 5.3.2 Two Variable Analyses

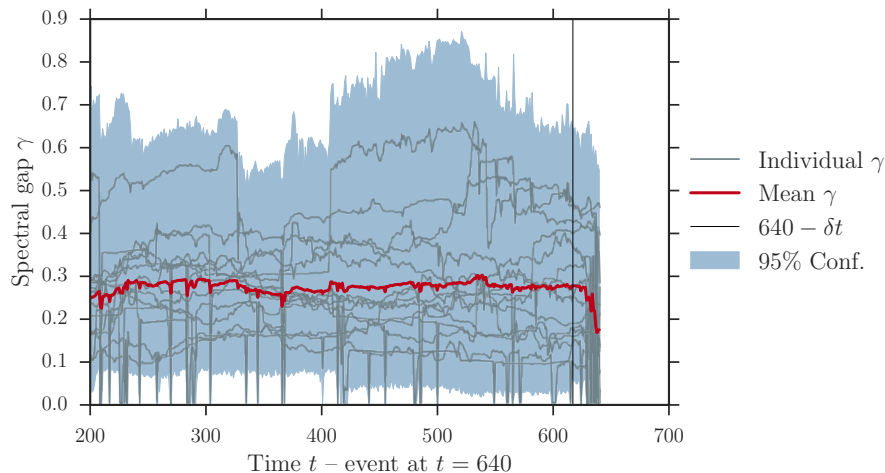


**Figure 5.12 | Spectral gap from 14  $[\text{Ca}^{2+}]$  and  $[\text{Na}^+]$  time series combined.** The TO is calculated on a  $15 \times 15$  grid in windows of size 200 years. Data  $\Delta t$  is 0.2 years. The confidence intervals were calculated for each series using 200 surrogate transition matrices. The blue shaded area shows the maximum and minimum 95% confidence interval taken over all the 14 time series. There is a small decrease in mean  $\gamma$  around  $t = 520$  years. However this decrease in  $\gamma$  represents a drop from about 0.24 to 0.2, and values of  $\gamma \approx 0.2$  are also seen in the beginning of the series.

### 5.3.3 Fraction of Transition Matrices Representing Irreducible Markov Chains

Figure	# Points ( $\gamma$ )	% Irreducible	% Aperiodic
Figure 5.9	6174	95.3%	97.7%
Figure 5.10	6174	97.7%	98.8%
Figure 5.11	6174	95.8%	97.9%
Figure 5.12	6174	89.8%	94.9%
Figure 5.13	6174	87.6%	93.5%

**Table 5.4 | Percentage of transition matrices representing irreducible and aperiodic Markov chains.** As we saw in Chapter 4 the occurrence of transition matrices representing reducible transition matrices may affect the reliability of the results.

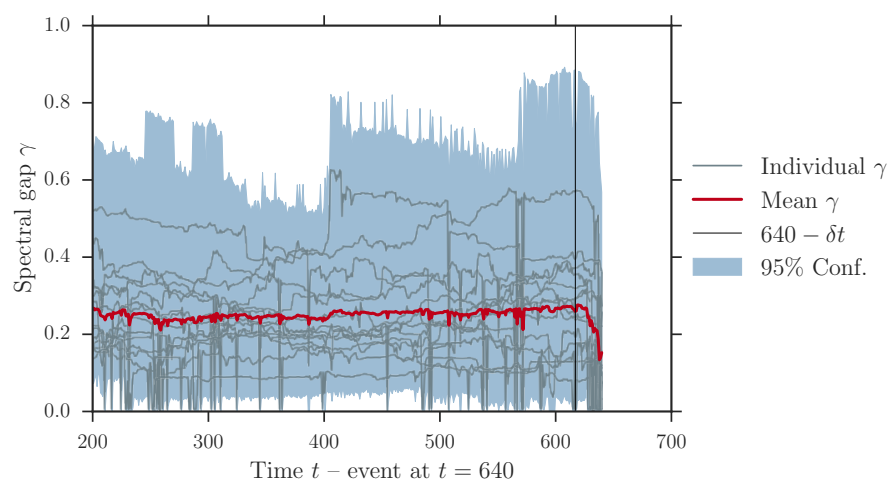


**Figure 5.13** | Spectral gap from 14  $[\text{Ca}^{2+}]$  and  $[\text{NH}_4^+]$  time series combined. Same interpretation as Figure 5.12, using  $[\text{NH}_4^+]$  instead of  $[\text{Na}^+]$ . The mean value of  $\gamma$  is close to constant at around 0.25.

## 5.4 Varying Parameters in the Transfer Operator Analysis

Here we repeat some of the calculations presented above while varying the parameters chosen for approximating  $\mathcal{L}_\tau$ . The purpose of this is to verify that the results we have obtained are not strongly dependent on the chosen parameters, and so a qualitative agreement is the objective.

Below is presented both ensemble means of  $\gamma(t)$ , the spectral gap as a function of time, and a subset of  $\gamma(t)$  series calculated for specific events. We will mainly focus on the ensemble means – the individual series are shown for completeness.

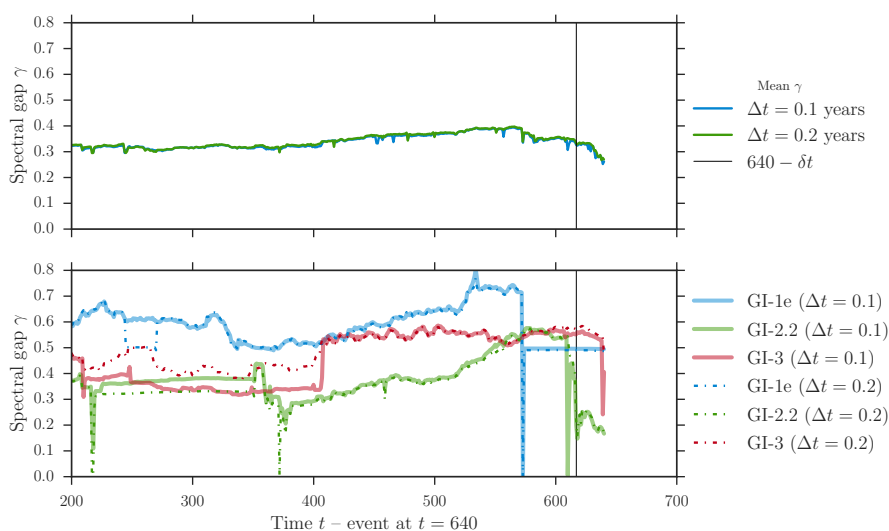


**Figure 5.14 | Spectral gap of  $[\text{Ca}^{2+}]$  for varying  $\Delta t$**  Here we analyze the 13 DO events marked “b)” in Table 5.3 where interpolation to  $\Delta t = 0.1$  years is feasible without upsampling. We perform this analysis for the  $[\text{Ca}^{2+}]$  data only, as this variable has the least fraction of consecutive missing values (cf. Figure 5.6). There are only negligible differences in the results of the two computations indicating that the data  $\Delta t = 0.1$  does not significantly influence the results.

These results in Figure 5.15 are in agreement with Tantet et al. (2015a, Figure 15) where it is found that decreasing the grid resolution leads to an increasing ‘rate’, the inverse of decorrelation time. The second rate  $r_2$  in Tantet et al. (2015a) corresponds to  $-\ln(1 - \gamma)/\tau$ .

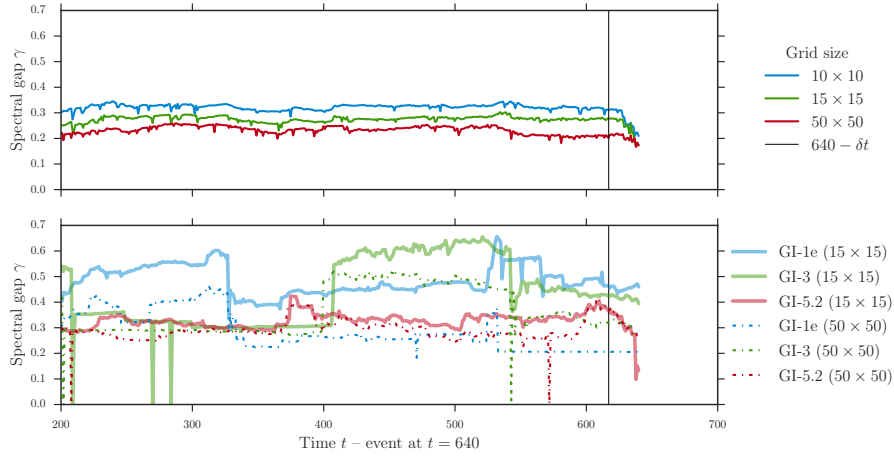


**Figure 5.15 | Spectral gap of  $[\text{Ca}^{2+}]$  and  $[\text{Na}^+]$  for varying grid resolution.** The results of lowering the grid resolution to  $10 \times 10$  and increasing the resolution to  $50 \times 50$  are shown. The same pattern is evident in all three series and we conclude that the results presented above are robust to changing grid size.

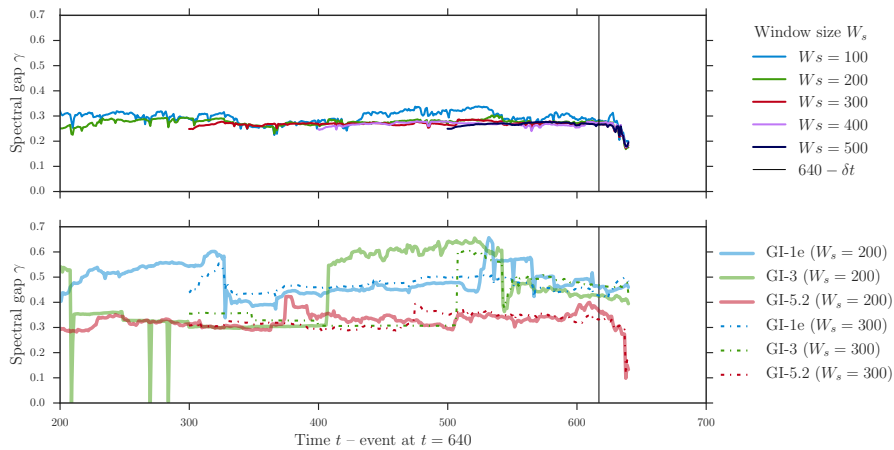


**Figure 5.16 | Spectral gap of  $[\text{Ca}^{2+}]$  and  $[\text{Na}^+]$  for varying window size.** We see that a larger window size  $W_s$  yields a series  $\gamma(t)$  that fluctuates less, which is to be expected when including more data points in the calculation. The general pattern is the same in all cases, an indication that the results are robust to variations in window size.

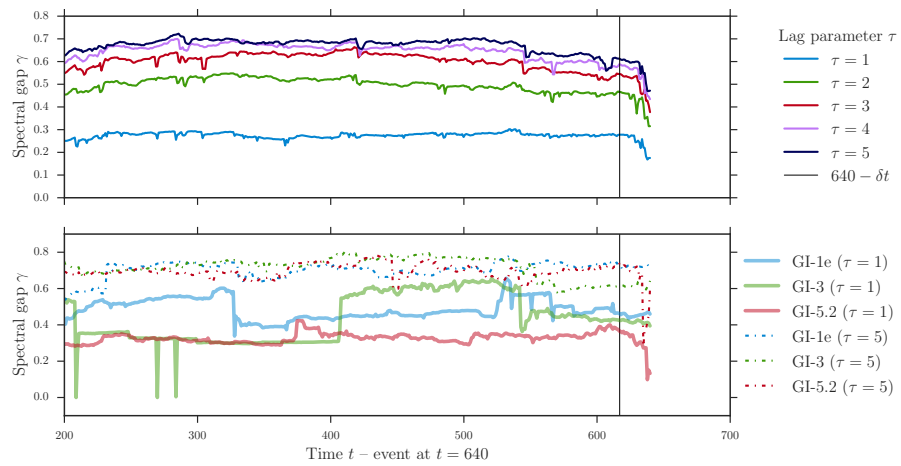


**Figure 5.17** | Spectral gap of  $[\text{Ca}^{2+}]$  and  $[\text{Na}^+]$  for varying lag parameter  $\tau$ . The variations in  $\gamma(t)$  seems to be higher for larger values of the lag parameter  $\tau$ . This is investigated further in Section 5.4.2.

### 5.4.1 Irreducible Markov Chains and Data

$W_s$	$N_r \times N_c$	# Points ( $\gamma$ )	% Irreducible	% Aperiodic
200	$10 \times 10$	6174	93.8%	97.2%
200	$15 \times 15$	6174	89.8%	94.9%
200	$50 \times 50$	6174	59.8%	75.5%
100	$15 \times 15$	7574	82.9%	91.9%
200	$15 \times 15$	6174	89.8%	94.9%
300	$15 \times 15$	4774	92.0%	95.9%
400	$15 \times 15$	3374	92.2%	95.8%
500	$15 \times 15$	1974	91.9%	95.5%

**Table 5.5 | Spectral gap for  $[\text{Ca}^{2+}]$  and  $[\text{Na}^+]$  time series – variation of parameters.** Percentage of irreducible and aperiodic transition matrices. It is clear that the amount of data available to calculate the matrices affect the results, as increasing the window size or decreasing the grid resolution leads to fewer reducible transition matrices; however, this number is seen to saturate at about 92% for a window size of 300. Highlighted rows denote the standard parameters.

### 5.4.2 Increasing the Lag Parameter to $\tau = 5$

In Figure 5.17 it appeared that increasing the lag parameter  $\tau$  will affect the results. To determine whether this is the case we compute  $\gamma$  for the  $[\text{Ca}^{2+}]$  time series with  $\tau = 5$ . The results are shown in Figure 5.18. We do observe a decrease in the ensemble mean of  $\gamma(t)$ , when investigating the individual series of  $\gamma(t)$  this decrease turns out to be caused by only three events, namely GI-18, GI-19.1 and GI-19.2 that we show in green in Figure 5.18.

Data	# Points ( $\gamma$ )	% Irreducible	% Aperiodic
$[\text{Ca}^{2+}]$	6174	88.3%	92.7%

**Table 5.6 | Irreducible and aperiodic Markov chains in Figure 5.18** These statistics for the computation using the  $[\text{Ca}^{2+}]$  series are comparable to the values reported in Table 5.4.

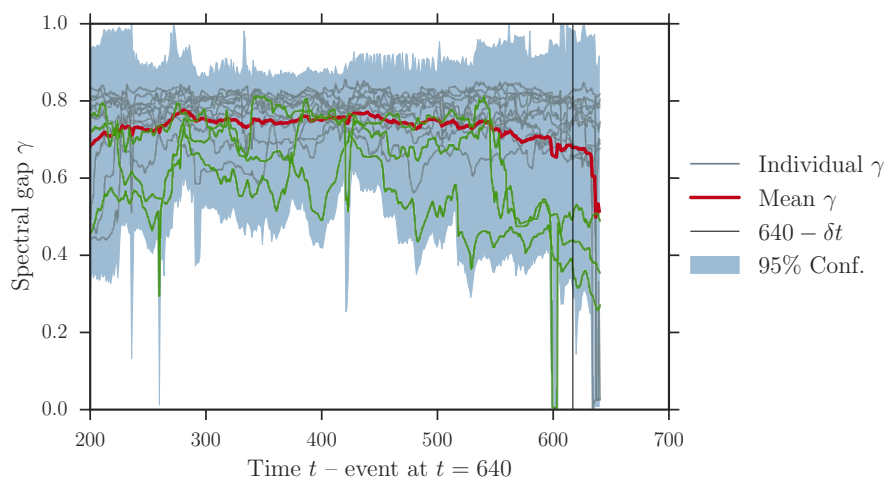


**Figure 5.18 | Spectral gap of the  $[\text{Ca}^{2+}]$  time series for  $\tau = 5$ .** Parameters are as in Figure 5.9, but here we also show the 95% confidence region calculated from 200 surrogate matrices at each value of  $\gamma(t)$  – the shaded area shows the maximum and minimum range for all series. The mean value of  $\gamma$  starts to drop at around  $t = 550$  – however, this pattern is only evident in three of the individual series of  $\gamma$ , corresponding to GI-18, GI-19.1 and GI-19.2 (shown in green). We can thus conclude that this is not a general feature of all (or most of) the events.

## 5.5 Discussion

We have analyzed three proxies from the NGRIP data set using the transfer operator. This analysis required choosing a set of parameters. Initially our choice of grid size, or number of boxes used to partition the reduced state space, was guided by demanding that a large fraction of the calculated transition matrices should represent irreducible and aperiodic Markov chains (cf. Section 4.2).

Within the confidence region of the estimated spectral gap  $\gamma(t)$ , we did not find any EWS leading up to the DO transitions in any of the timeseries we analyzed in Section 5.3. Varying the chosen parameters in Section 5.4 did not change this conclusion, thus confirming that the results were not caused by specific parameter choices.

Our findings here do not support the several of the studies in Section 1.3.2 where EWS were reported, but do support Ditlevsen and Johnsen (2010) where no EWS prior to DO events were reported. Likewise, our conclusion may support the findings of Ditlevsen et al. (2007) where the recurrence times of the DO events were studied and found to be compatible with random occurrences, as opposed to being cyclic.

## 6 Minimal Ice Sheet Model With Stochastic Forcing

In the manuscript Mikkelsen et al. (2017) (Appendices D and E) we study a minimal complexity ice sheet model that describes the time evolution of an ice sheet as a function of temperature. When forcing the model with fluctuating temperatures we find that the steady state volume decreases; ie. the *variation* in temperature is directly responsible for the lower steady state volume.

The idea for this study was initially proposed by Aslak Grinsted at the Centre for Ice and Climate (CIC) retreat at Møn, August 16th–18th, 2014. At the time of writing we are finishing revisions before re-submitting the manuscript to Geophysical Research Letters (GRL).

### 6.1 Summary of Mikkelsen et al. (2017)

#### 6.1.1 Notation

We remark that there are slight differences between the notation used in the manuscript, and that used in the rest of this thesis. In the manuscript we use angle brackets to denote expectation, and use subscript  $t$  for a *discrete* time variable. The choice was made to use  $E[\cdot]$  for the expectation in this thesis due to the extensive use of angle brackets as inner products in Chapter 2. Conversely, brackets are commonly used to denote expectation in physics (eg. Ditlevsen (2004) and Weisstein (2017)), in which we expect the readers of the manuscript to have a background. As this chapter is most likely read in connection with the manuscript, we will use the same notation here in Chapter 6 as in Mikkelsen et al. (2017). The choice of different notation can be summarized as follows: if

$$\langle X_t \rangle = \bar{X}, \quad (6.1.1)$$

then the expected value of the discrete time series  $\{X_t\}$  is  $\bar{X}$ .

#### 6.1.2 Summary

For this study we use a model proposed by Oerlemans (2003). The ice sheet in the model is sketched in Figure 6.1, and the model is thoroughly described in Appendix E. We choose parameters so that the steady state ice sheet volume in the model roughly approximates the ice sheet volume on Greenland (Appendix E, Table 1).

Oerlemans (2003) describes the model “quasi-analytical” in the sense that one can obtain an analytical relationship specifying  $dR/dt = f(T, R)$ , where

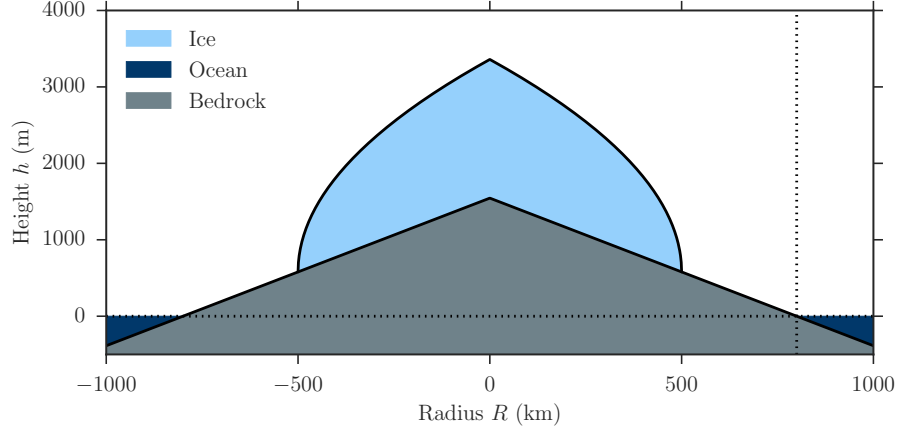


**Figure 6.1 | Sketch of the ice sheet in the Oerlemans (2003) model.** The ice sheet is symmetric around  $R = 0$  and coupled to the surrounding temperature through the height of the equilibrium line (Appendix E, Figure 1 and Equation 2).

$R$  is the radius of the ice sheet, and  $T$  the temperature at the surface. For a given set of parameters, the volume  $V$  can then be uniquely determined from  $R$ , allowing us to write

$$\dot{V} := \frac{dV}{dt} = f(T, V), \quad (6.1.2)$$

whereafter we integrate Equation (6.1.2) numerically. We use the EM method for this purpose since it is adequate (Appendix E, Figure 2) and integrate the model with  $\Delta t = 1$  year. At a steady state  $(T_0, V_0)$  the volume will not change:

$$f(T_0, V_0) = 0. \quad (6.1.3)$$

We now let the temperature fluctuate as follows. We fit an AR(1) model to the observed annual mean temperature over Greenland from 1851 to 2011 (Appendix E, p. 6), allowing us to generate temperature time series  $T_t$  with different mean temperatures  $\bar{T} = \langle T_t \rangle$ .

Now, as opposed to Equation (6.1.3), a *statistical* steady state will be characterized by

$$\langle f(\bar{T}, \bar{V}) \rangle = 0 \quad (6.1.4)$$

where  $\bar{V} = \langle V_t \rangle$  is the time average of the volume time series  $V_t$  resulting from integrating Equation (6.1.2) with  $T_t$  as forcing.

The main observation in Mikkelsen et al. (2017) is attained after performing a Taylor expansion of Equation (6.1.4) around  $(\bar{T}, \bar{V})$  (Appendix D, Equations 2-5), whence we obtain

$$\langle f(T_t, V_t) \rangle \approx f^0 + \frac{\sigma^2}{2} f_{TT}^0; \quad (6.1.5)$$

here  $f^0 = f(\bar{T}, \bar{V})$  and  $f_{TT}^0 = \frac{\partial^2 f}{\partial T^2} |_{(\bar{T}, \bar{V})}$ . To arrive at Equation (6.1.5), first note that some terms in the Taylor expansion vanish because we expand around  $(\bar{T}, \bar{V})$ . The remaining terms that involve  $f_{VV}^0$  and  $f_{TV}^0$  (defined in a similar

way as  $f_{TT}^0$ ) are evaluated numerically and found to be negligible (Appendix E, Figure 4). Note that the arguments leading to Equation (6.1.5) are independent of the Oerlemans (2003) model.

The physical mechanism responsible for the decrease in steady state volume can be explained quite simply: a large temperature increase has the potential to melt a large amount of ice in a short time. On the other hand, it takes a long time to build up an ice sheet through precipitation. This asymmetry is evident in the surface mass balance (SMB) against  $T$  curves (Appendix D, Figure 2 left).

Next we “forecast” the effect of temperature fluctuations by comparing the prediction of Equation (6.1.5) with time series  $V_t$  from the model; we find an excellent agreement (Appendix D, Figure 1).

Finally we evaluate this effect on the study by Robinson et al. (2012). They present a series of long term Greenland Ice Sheet (GrIS) forecasts for a range of temperature increases or “warmings”. Robinson et al. (2012) couple their ice sheet model to a regional climate model (RCM) which in turn is forced by a constant temperature climatology at the boundaries (Robinson et al. 2012, Methods).

For a realistic warming relative to today, we find that Robinson et al. (2012) may overestimate the GrIS SMB by as much as 30 Gt/yr (gigaton per year). For context, the current GrIS SMB is estimated at  $-234 \pm 20$  Gt/yr (Barletta et al. 2013).

## 6.2 Discussion

Our estimate of the effect of temperature fluctuations on the results of Robinson et al. (2012) is a worst case scenario, since the coupling of the ice sheet model to an RCM presumably generates some temperature fluctuations; thus the effect we describe is most likely accounted for to some extent.

Furthermore, many studies may already *implicitly* account for this effect since ice sheet models are often *tuned* to the problem under investigation. When tuning an ice sheet model, one could – for example – attempt to reproduce an observed ice sheet history with a model using a time series of observed forcing (temperature, precipitation etc.) as input. Parameters in the model are then adjusted so that output best matches observations; see eg. Muresan et al. (2016) for an example of this approach.

By adjusting a range of parameters this way it is possible, and likely, that the effect we describe is already partly or completely accounted for in many model studies; not explicitly, but “hidden” in the parameter tuning.

## 6.3 Ideas for Future Work

The logical next step is to investigate the effect of fluctuating temperatures using a more realistic model than the Oerlemans (2003) model.

Currently we are working on the design of a study using the Parallel Ice Sheet Model (PISM) (Bueller and Brown 2009; Aschwanden. et al. 2012; PISM 2017) for this purpose, incidentally the same ice sheet model that was used in Muresan et al. (2016).



# 7 Discussion & Conclusion

## 7.1 Transfer Operator Analysis of NGRIP Data

In the first part of this thesis we used a novel method based on the transfer operator to search for EWS before DO events. This analysis was done after verifying that the method could distinguish time series from a double well potential model undergoing either 1) a stochastic transitions or 2) a bifurcation induced transitions. Based on the literature review presented in Section 1.3.2, we focused our analysis on ensembles of events instead of time series from individual events.

As we did not observe any EWS, our findings suggest that DO events are most likely random transitions. Thus our conclusion supports the findings of Ditlevsen et al. (2007) and Ditlevsen and Johnsen (2010), but does not support the findings of for example Cimatoribus et al. (2013), Nikolaou et al. (2014), and Rypdal (2016).

Active research is still being contributed to an already well developed body of literature on the theoretical aspects of transfer operators. On the other hand, the literature concerned with applications is quite scattered. This means that the road from an interesting data set to a finished analysis based on the transfer operator requires sourcing information from several articles, as opposed to a unified source.

The situation at present then clearly calls for a review paper with a focus on methodology, while still presenting a necessary amount of theory. Such a paper would ideally include topics from the chaotic hypothesis to the spectral mapping theorem. The biggest challenges presented by writing such a paper would be to balance between presenting all the sufficient – but only the necessary – theory at each step.

A review paper in this format would make transfer operator methods accessible to a much wider audience, and would ideally be accompanied or complemented by a well-tested and well-documented numerical library in a language suited for numerical analysis, such as `Python`, `Julia` or `R`.

In Chapter 1 we mentioned the *R*-tipping and the relatively recent results obtained in this area of research. To the author’s knowledge, no results combining knowledge about *R*-tipping and transfer operators have been contributed. Analysis of time series from an *R*-tipping system could provide an exciting challenge for the transfer operator approach to tackle. As the *raison d’être* for *R*-tipping as a concept was the *compost-bomb instability* – a real world climatic problem – such an analysis could potentially contribute knowledge about an essential problem in climate research.

## 7.2 Minimal Ice Sheet Model With Stochastic Forcing

Our goal of the second part was to investigate the consequences of fluctuating surface temperatures in an ice sheet model. We derived an analytical relationship between the magnitude of the fluctuations and the reduction in steady state ice sheet volume, and we found this expression to be in agreement with numerical results from the minimal complexity Oerlemans (2003) model. We clearly showed that temperature fluctuations of a realistic magnitude lead to a decrease in steady state ice sheet volume.

Furthermore we estimated which effects fluctuating temperatures could have on the results of recent long term Greenland ice sheet simulations (Robinson et al. 2012), were a constant temperature climatology was used.

It is clear that studies exploiting more comprehensive ice sheet models are needed to further clarify this effect. Using a more comprehensive model such as the PISM would allow us to uncover in greater detail the physical mechanisms behind the mathematical results we presented in Mikkelsen et al. (2017).

The discussion of physical mechanisms leads to another intriguing area to explore. As opposed to the SMB vs. temperature-relationship we investigated in Mikkelsen et al. (2017), the SMB in large parts of Antarctica shows the *opposite* relationship to temperature: increasing temperature leads to increasing precipitation, which in turn drives a higher accumulation rate. This relationship is naturally only valid for a limited temperature increase relative to today. For such a study, one would likely need to couple the ice sheet model to a regional climate model as the precipitation is influenced strongly by the surrounding climate.

As melting of the West Antarctic Ice Sheet (WAIS) would have drastic consequences on sea level, the topic of most accurately modeling WAIS is natural are to explore.

An important question of a general nature is, how much has the effect of temperature fluctuations already been *implicitly* accounted for by model tuning? As mentioned in Section 6.2, the effect of temperature fluctuations may already be partly or completely accounted for by model tuning.

Nevertheless, the clearest possible interpretation of all model parameters is always desirable. We believe that our findings contribute to this by potentially isolating effects of temperature variation that were previously hidden in other parameters.

## Appendix A

# List of Acronyms

**AC** autocorrelation.

**ACF** autocorrelation function.

**AMOC** Atlantic Meridional Overturning Circulation.

**AR** autoregressive.

**ARIMA** autoregressive integrated moving average.

**ARMA** autoregressive moving average.

**BA** Bølling-Allerød.

**CFA** continuous flow analysis.

**CIC** Centre for Ice and Climate.

**CWT** continuous wavelet transform.

**DEW** distant early warning.

**DFA** detrended fluctuation analysis.

**DO** Dansgaard-Oeschger.

**DW** double well.

**DYE-3** Distant Early Warning Line (Cape Dyer), Station 3.

**EGRIP** East Greenland Ice-core Project.

**EM** Euler-Maryuama.

**ENSO** El Niño-Southern Oscillation.

**EOF** empirical orthogonal function.

**EWS** early warning signals.

- FP** Fokker-Planck.
- GA** genetic algorithm.
- GI** Greenland Interstadial.
- GICC05** Greenland Ice Core Chronology 2005.
- GICC05modelext** Greenland Ice Core Chronology 2005, model extended.
- GISP** Greenland Ice Sheet Project.
- GISP2** Greenland Ice Sheet Project 2.
- GRIP** Greenland Ice Core Project.
- GrIS** Greenland Ice Sheet.
- GRL** Geophysical Research Letters.
- GS** Greenland Stadial.
- ITCZ** intertropical convergence zone.
- ka** kilo years.
- ka b2k** kilo years before year 2000.
- LGM** Last Glacial Maximum.
- MA** moving average.
- Ma** million years.
- MCE** maximum counting error.
- NaN** not a number.
- NEEM** North Greenland Eemian Ice Drilling.
- NGRIP** North Greenland Ice Core Project.
- ODE** ordinary differential equation.
- OU** Ornstein-Uhlenbeck.
- PCA** principal component analysis.
- PF** Perron-Frobenius.
- PISM** Parallel Ice Sheet Model.
- ppbw** parts per billion, weight.
- RCE** relative counting error.

- RCM** regional climate model.
- RK** Runge-Kutta.
- SDE** stochastic differential equation.
- SMB** surface mass balance.
- SMT** Spectral Mapping Theorem.
- SRB** Sinai-Ruelle-Bowen.
- Sv** Sverdrup.
- THC** thermohaline circulation.
- TO** transfer operator.
- Var** variance.
- V-SMOW** Vienna standard mean ocean water.
- WAIS** West Antarctic Ice Sheet.
- YD** Younger Dryas.



## Appendix B

# Numerical Tools

### B.1 Libraries Developed and Reproducibility of Results

The results presented in Chapters 2 to 5 were made with Python, while we used MATLAB for Mikkelsen et al. (2017). Some of the routines we developed have been compiled into the libraries shown below, of which we give a brief and non-exhaustive summary.

The results shown in Chapter 5 were made using the NGRIP CFA dataset (Ruth et al. 2003; Bigler 2004); this data set is unfortunately not in the public domain at the time of writing. After having obtained this dataset and the GICC05 time scale available from CIC (2010) – and after having set local path variables – the results in Chapters 2 to 5 can be reproduced with the libraries mentioned in items 1–4 below; these have as dependency the Python packages in Appendix B.2. Note that the results in Chapters 2 to 4 are independent of the NGRIP dataset.

Similarly, most of the results presented in Mikkelsen et al. (2017) can be reproduced using the the library in item 5 below, which in turn have as dependency the MATLAB packages in Appendix B.3. To reproduce the full set of results, one must acquire the data from the simulations done by Robinson et al. (2012). This was obtained effortlessly by private communication with Alexander Robinson, but we do not consider it ours to share.

We have developed the following libraries:

1. [bitbucket.org/bogeholm/criticalstatistics](https://bitbucket.org/bogeholm/criticalstatistics) implements the EM method and is used for some calculations of running statistics.
2. [bitbucket.org/bogeholm/topy](https://bitbucket.org/bogeholm/topy) – for “transfer operators in Python” – is used for calculating transitions matrices and spectral gaps.
3. [bitbucket.org/bogeholm/notebookcommon](https://bitbucket.org/bogeholm/notebookcommon) contains various utility functions that are used in several Jupyter notebooks (see below).
4. [bitbucket.org/bogeholm/phd-mikkelsen-jupyter](https://bitbucket.org/bogeholm/phd-mikkelsen-jupyter) comprises the full set of Jupyter notebooks (see below) used for producing the results in Chapters 2 to 5.
5. [bitbucket.org/bogeholm/ice-sheets-fluctuating-temp](https://bitbucket.org/bogeholm/ice-sheets-fluctuating-temp) contains the MATLAB code for Mikkelsen et al. (2017).

6. [github.com/bogeholm/pytisean](https://github.com/bogeholm/pytisean) is a Python interface for the TISEAN library (Hegger et al. 1999) which we explored, but did ultimately not use in this thesis.

## B.2 Python Tools Used

We have derived tremendous utility from the following Python tools:

- **Scipy** ([scipy.org](https://scipy.org)) (Jones et al. 2001): numerical routines such as linear algebra functions, eigenvalue computations and curve fitting.
- **NumPy** ([numpy.org](https://numpy.org)) (Walt et al. 2011): implements matrices and vectors, and a variety of numerical routines.
- **IPython** ([ipython.org](https://ipython.org)) (Pérez and Granger 2007): interactive Python shell.
- **Jupyter** ([jupyter.org](https://jupyter.org)) (Kluyver et al. 2012): implements a notebook format so code, output and figures can be viewed together in a browser. This, dear reader, is the future!
- **Matplotlib** ([matplotlib.org](https://matplotlib.org)) (Hunter 2007): library for creating figures.
- **Pandas** ([pandas.pydata.org](https://pandas.pydata.org)) (McKinney 2010): implements a `DataFrame` object that is very useful for time series analysis.
- **Scikit-learn** ([scikit-learn.org](https://scikit-learn.org)) (Pedregosa et al. 2011): machine learning routines used for PCA when making Figure 2.4.
- **Seaborn** ([seaborn.pydata.org](https://seaborn.pydata.org)) (Waskom et al. 2014): additional plotting utilities.
- **PyDSTool** ([pydstool.sourceforge.net](https://pydstool.sourceforge.net)) Clewley et al. (2007) and Clewley (2012): methods for numerical continuation and creating bifurcation diagrams, used for making Figure 3.6.
- **Statsmodels** ([statsmodels.sourceforge.net](https://statsmodels.sourceforge.net)) (Seabold and Perktolf 2010): statistical routines used eg. for calculating autocorrelation, fitting AR models and curve fitting.
- **xarray** ([xarray.pydata.org](https://xarray.pydata.org)) (Hoyer and Hamman 2016; Hoyer et al. 2016) implements a data format that allows handling of arbitrary dimensional data sets.
- **NetworkX** ([networkx.github.io](https://networkx.github.io)) (Hagberg et al. 2008): we use the function `from_numpy_matrix()` to create a directed graph from transition matrices, which in turn allows us to use `is_strongly_connected()` and `is_aperiodic()` to determine if a matrix is irreducible and/or aperiodic, respectively.
- **SymPy** ([github.com/sympy/sympy](https://github.com/sympy/sympy)) (SymPy Development Team 2016): symbolic calculations.

### B.3 MATLAB Tools Used

The following MATLAB packages from the [MATLAB File Exchange](#) were used, mainly for producing the figures in Mikkelsen et al. (2017):

- [export\\_fig](#) by Yair Altman: for saving figures.
- [ds2nfu](#) by Michelle Hirsch: plotting utilities.
- [hslcolormap](#) by Aslak Grinsted: used for the colormap in Mikkelsen et al. (2017, Figure 1).
- [suplabel](#) by Ben Barrowes: plotting utilities.
- [matrix2latex](#) by Moritz Koehler: for exporting data to  $\text{\LaTeX}$  tables.



## Appendix C

# Co-Author Statements

The co-author statement regarding Mikkelsen et al. (2017) has been handed in separately from this thesis. The form is number 3A from [science.ku.dk/english/research/phd/student/forms/](https://science.ku.dk/english/research/phd/student/forms/).

The wording of the co-authorship statement is reproduced here.

- What was the role of the PhD student in designing the study?
  - The study was jointly designed by all three authors.
- How did the PhD student participate in data collection and/or development of theory?
  - Troels did the numerical work, Peter and Aslak contributed with ideas and interpretation.
- Which part of the manuscript did the PhD student write or contribute to?
  - Aslak and Troels co-wrote the introduction, Troels wrote draft versions of the rest of the paper.
- Did the PhD student read and comment on the final manuscript?
  - N/A



## Appendix D

# Influence of temperature fluctuations on equilibrium ice sheet volume

# **Influence of temperature fluctuations on equilibrium ice sheet volume**

**Troels Bøgeholm Mikkelsen<sup>1</sup>, Aslak Grinsted<sup>1</sup> and Peter D. Ditlevsen<sup>1</sup>**

<sup>1</sup>Centre for Ice and Climate, Niels Bohr Institute, Juliane Maries Vej 30, DK-2100 Copenhagen Ø

## **Key Points:**

- Fluctuating temperatures lower the steady state volume of an ice sheet model.
- We derive an analytic relationship between temperature fluctuations and volume.
- We evaluate the consequences for long term ice sheet simulations.

---

Corresponding author: Troels Mikkelsen, bogeholm@nbi.ku.dk

## Abstract

Forecasting the future sea level relies on accurate modeling of the response of the Greenland and Antarctic ice sheets to changing temperatures. We show why the steady state of an ice sheet is biased toward larger size if the interannual weather generated fluctuations in temperature are not taken into account in numerical modeling of the ice sheet. We illustrate this in a simple ice sheet model. This bias could, if not taken into account, imply that the risk of collapse in a given climate change scenario is underestimated. We estimate that the effect of temperature variability on the surface mass balance of the Greenland Ice Sheet in recent ensemble forecasting should be adjusted downward by approximately 13 percent of the present day observed value, if assuming a 2 degree warming. Many predicted scenarios of the future climate show an increased variability in temperature over much of the Earth. In light of our findings it is important to gauge the extent to which this increased variability will further influence the mass balance of the ice sheets.

## 1 Introduction

Using coupled climate and ice sheet models, long time forecasting is often made computationally feasible by running a climate model for one or more years and then repeatedly applying the climate (or the surface mass balance computed from it) to an ice sheet model [Vizcaino et al., 2015; Roche et al., 2014; Ziemen et al., 2014; Gregory et al., 2012]. Some studies [e.g. Kageyama et al., 2004] compute the surface mass balance from a climatology. The present analysis shows that computing the surface mass balance from a climatology can result in a bias towards a larger ice sheet size, if the tuning is done with computing the surface mass balance from individual model years. Peter ToDo: Check references Ice sheet modeling and evidence from paleoclimatic records indicate that ice sheets display a hysteresis response to climate forcing [Abe-Ouchi et al., 2013; Robinson et al., 2012]. There is a critical threshold in temperature, a tipping point, beyond which an ice sheet becomes unsustainable. This is a generic saddle-node bifurcation point, estimated by Robinson et al. [2012] to be reached for the Greenland Ice Sheet (GrIS) at a global warming of  $+1.6^{\circ}\text{C}$  ( $0.8^{\circ}\text{C} - 3.2^{\circ}\text{C}$ ) above preindustrial.

Several recent studies suggest that parts of the West Antarctic Ice Sheet (WAIS) may already have been destabilized [Favier et al., 2014; Joughin et al., 2014; Rignot et al., 2014; Mouginot et al., 2014; Seroussi et al., 2014]. Other studies find that East Antarctica may be more vulnerable to warming than previously thought [Mengel and Levermann, 2014; Greenbaum et al., 2015; Sun et al., 2014; Pollard et al., 2015; Fogwill et al., 2014]. There is a growing concern for a considerable risk of a marine ice-sheet instability of the WAIS may lead to a substantial sea level rise contribution already this century [Bamber and Aspinall, 2013].

Paleoclimatic records show a nonlinear relationship between temperature increase and sea level rise consistent with the threshold behavior of ice sheets, predicted by modeling studies. Gasson et al. [2012]; Foster and Rohling [2012] find that even a moderate global warming of  $+2^{\circ}\text{C}$  or  $\text{CO}_2$  levels of 400 ppm is associated with a likely long-term sea level rise of more than 9 m. This is consistent with evidence from the last interglacial which points toward a collapse of the WAIS [Kopp et al., 2009; Dahl-Jensen et al., 2013; Strugnell et al., 2012]. Likewise there is evidence for at least one substantial deglaciation period in Greenland having occurred during the past 1.1 million years. Blard et al. [2016]; Bierman et al. [2016]; Schaefer et al. [2016]

The greenhouse gas concentrations and intense warming in high-end scenarios such as ECP8.5 (Extended Concentration Pathways, extension of Representative Concentration Pathways beyond 2100) [Meinshausen et al., 2011] correspond to an ice-free planet in the paleoclimatic record [Gasson et al., 2012; Foster and Rohling, 2012] which evidence suggests was the case until approximately 35 million years ago [Ruddiman, 2014].

Observations, paleoclimatic records and model studies indicate a real risk of ice sheet collapse for realistic future scenarios global warming. A substantial part of WAIS may already be committed to collapse. The threshold for GrIS is estimated to be passed in ECP4.5 and ECP6, and even total deglaciation is within reach of the ECP8.5 scenario. The complete loss of the Greenland -, the West Antarctic -, and the East Antarctic ice sheets would raise global sea levels by 7.4 m, 4.3 m, and 53 m respectively, excluding any solid earth rebound effects that would take place during ice sheet decay [Bamber *et al.*, 2013; Fretwell *et al.*, 2013]. The risk that global warming might exceed the tipping points of ice sheet stability pose an existential threat to low lying coastal nations. Estimating how close each ice sheet is to a tipping point is thus critically important .

The stability of ice sheets is typically investigated by imposing a constant climate forcing and then letting the ice sheet model reach equilibrium [Robinson *et al.*, 2012; Solgaard and Langen, 2012; Huybrechts and de Wolde, 1999]. The hysteresis curve, and collapse thresholds are then traced out by repeating these experiments for a range of temperatures and starting from ice free conditions. However, this approach disregards the effects of interannual variability.

In the classical study of the effect of asynchronous coupling by Pollard *et al.* [1990] it was noticed that a stochastic forcing in an ice sheet model results in a smaller ice sheet in comparison to a constant constant forcing. Here we show how variability in forcing changes the expected mass balance of an ice sheet. We develop a general theoretical framework for how forcing variability impact the expected response in a model that exhibits a non-linear response. We illustrate the importance using a minimal model of how Greenland surface mass balance responds to temperature fluctuations. The simple model is also used to assess the bias adjustments needed in model studies when constant forcing is applied.

Though some studies implement full GCM coupling to the ice sheet model, or have some mixed approaches [Ridley *et al.*, 2005] [Gregory and Huybrechts, 2006], the computational demand of the GCM could come at an expense for the resolution of the ice sheet flow model. The results presented here shows explicitly how to account for the effect of unresolved temperature variability.

Previous studies of natural variability in the context of ice sheets include Fyke *et al.* [2014], who find that the variability of the GrIS surface mass balance will increase in a warmer climate due to increased ablation area, and Roe and O'Neal [2005] who find that large fluctuations in glacier extent can be driven by natural, fast fluctuations in climate.

That the SMB of an ice sheet model is nonlinear is well known. Ridley *et al.* [2010] specifically avoid using monthly climatologies in order to include the effect of interannual variability in their study. Seguinot [2013] shows how simplifying assumptions (in general leading to lower temperature variability) in a positive degree day (PDD) scheme leads to errors. Fettweis *et al.* [2013, see Figure 6h] investigate the GrIS SMB simulated by regional climate models (RCM) as a function of mean surface temperature from general circulation models (RCM). Our contribution is a quantification of this effect, and an estimate of the necessary bias correction in long term ice sheet simulations.

Sub-annual temperature variability in the context of positive degree-day (PDD) is investigated in Hock [2003], Seguinot [2013] and Wake and Marshall [2015] – in the present study we are concerned with interannual variability and our results apply to a broader class of models.

## 2 The Mass Balance of an Ice Sheet

### 2.1 A Minimal Ice Sheet Model

We consider a simple ice sheet model introduced by *Oerlemans* [2003] hereafter denoted *Oer03*. This model describes the essential dynamics of an ice sheet initiated from a mountain glacier. It assumes an axially symmetric ice sheet resting on a bed that slopes linearly downwards from the center. The ice is modeled as a perfectly plastic material, and the ice sheet is coupled to the surrounding climate by adjusting the height of the equilibrium line – above this the specific balance is constant and below this the balance decreases linearly with decreasing altitude (supplementing text).

The model is chosen for its simplicity, thus it is not accurately modeling a specific ice sheet; the two main reasons for choosing it for our analysis are: 1) The simplicity of *Oer03* allows the analytical approach detailed below and 2) The *Oer03* model shows the same functional relationship between surface mass balance (SMB) and temperature as has been found for regional climate models (RCM) for a range of temperature scenarios [*Fettweis et al.*, 2013]. The change in volume or mass of the ice sheet depends on the balance between accumulation, ablation and ice sheet discharge which in turn depends on both the interplay between the fluctuating temperature and the state of the ice sheet itself.

Before proceeding with the simple model, we investigate the effect of interannual temperature fluctuations by considering the ice sheet as a simple dynamical system. Assume the mass balance of the ice sheet to depend only on the volume  $V$  itself and a single time-varying mean temperature over the ice sheet,  $T$ ; thus all components of the mass budget are uniquely determined by temperature and volume. This is a vast simplification but sufficient to illuminate the essential dynamical effect we consider in this paper. Denoting the mass balance (change in ice sheet volume) as  $\dot{V}$ ,

$$\dot{V} = f(T, V), \quad (1)$$

where  $f(V, T)$  is some non-linear function. The (stable) fixed point,  $f(T, V) = 0$  corresponds to a balance between loss and gain in the ice volume. This is in general an implicit equation to determine the steady state volume  $V_0(T)$  as a function of temperature, such that  $f(V_0(T), T) = 0$ .

However, the fixed point is not identical to the statistically steady state volume with a temporally fluctuating temperature  $T_t = T(t)$  with expectation value  $\langle T_t \rangle = \bar{T}$ . A comparison between an ice sheet model with and without interannual fluctuating temperature shows that in steady state the ice sheet volume  $V_t$  will fluctuate around  $\langle V_t \rangle = \bar{V}$  where  $\bar{V}$  is systematically smaller than the corresponding  $V_0(T)$ .

Since the temperature  $T_t$  – and thus the ice sheet ice sheet volume  $V_t$  – is a stochastic variable the following will characterize an equilibrium state:

$$\langle f(T_t, V_t) \rangle = 0. \quad (2)$$

To calculate  $\bar{V}$  we perform a Taylor expansion of (2) around the – presently unknown – steady state  $(\bar{T}, \bar{V})$  and calculate the mean volume  $\bar{V}$ . We use the notation  $f_T := \frac{\partial f}{\partial T}$ ,  $f_{TV} := \frac{\partial^2 f}{\partial T \partial V}$ , etc. Furthermore,  $f^0 := f(\bar{T}, \bar{V})$ ,  $f_T^0 := \left. \frac{\partial f}{\partial T}(T, V) \right|_{(\bar{T}, \bar{V})}$  etc. We then get:

$$\begin{aligned} \langle f(T_t, V_t) \rangle &= f^0 + \langle T_t - \bar{T} \rangle f_T^0 + \langle V_t - \bar{V} \rangle f_V^0 + \frac{1}{2} \langle (T_t - \bar{T})^2 \rangle f_{TT}^0 \\ &\quad + \frac{1}{2} \langle (V_t - \bar{V})^2 \rangle f_{VV}^0 + \langle (T_t - \bar{T})(V_t - \bar{V}) \rangle f_{TV}^0 + \mathcal{O}(3), \end{aligned} \quad (3)$$

where  $\mathcal{O}(3)$  represents higher order terms.

We can simplify (3) considerably: First note that since  $\bar{T}$  is the expectation value of  $T_t$  we have  $\langle T_t - \bar{T} \rangle = \langle T_t \rangle - \bar{T} = \bar{T} - \bar{T} = 0$  and with the same argument  $\langle V_t - \bar{V} \rangle = 0$ . The

quantity  $\langle (T_t - \bar{T})^2 \rangle$  is the variance of the fluctuating temperature – we will assume this is known in simulations and substitute  $\langle (T_t - \bar{T})^2 \rangle = \sigma_T^2$ . Since the temperature variations are small with respect to the mean and has a symmetric distribution we may neglect higher order terms in (3) *Rodriguez and Tuckwell [1996]* We are left with:

$$\begin{aligned} \langle f(T_t, V_t) \rangle &\approx f^0 + \frac{\sigma_T^2}{2} f_{TT}^0 \\ &+ \frac{1}{2} \langle (V_t - \bar{V})^2 \rangle f_{VV}^0 + \langle (T_t - \bar{T})(V_t - \bar{V}) \rangle f_{TV}^0. \end{aligned} \quad (4)$$

We have evaluated the last two terms in (4) numerically for the model presented in Section 3 and found that  $\langle (V_t - \bar{V})^2 \rangle$  and  $\langle (T_t - \bar{T})(V_t - \bar{V}) \rangle$  tend to zero (supplementing information) – neglecting the last two terms (4) reduces to

$$\langle f(T_t, V_t) \rangle \approx f^0 + \frac{\sigma_T^2}{2} f_{TT}^0. \quad (5)$$

Equation (5) is the main observation in this work. We shall in the following estimate the implications of this result on realistic asynchronously coupled state-of-the-art ice sheet climate model simulations. As  $\langle f(T_t, V_t) \rangle = 0$  at the steady state it can be seen from (5) that

$$\begin{aligned} 0 &= f^0 + \frac{\sigma_T^2}{2} f_{TT}^0 \Rightarrow \\ f^0 &= -\frac{\sigma_T^2}{2} f_{TT}^0 > 0 \end{aligned} \quad (6)$$

since  $f_{TT}^0 < 0$  – this negative curvature of  $f^0$  is the nonlinear effect causing the bias.  $V_0(T)$  is the stable fixed point;  $f(V_0(T), T) = 0$ , thus  $f(V, T) > 0$  for  $V < V_0$  and  $f(V, T) < 0$  for  $V > V_0$ . This together with (6) implies that  $\bar{V} < V_0$ .

### 3 Ice Sheet Simulations

#### 3.1 Fluctuating Temperatures

To generate an ensemble of volume simulations we use time series  $T_t$  comparable to the observed temperatures over Greenland between year 1851 and 2011. For this we use the AR(1)-process [*Hasselmann, 1976; Frankignoul and Hasselmann, 1977; von Storch and Zwiers, 2003; Mudelsee, 2010*]:

$$T_{t+1} = \bar{T} + a \times (T_t - \bar{T}) + \sigma_{AR} W_t. \quad (7)$$

The parameters  $(a, \sigma_{AR}^2)$  were obtained by fitting (7) to the observed annual mean temperatures over Greenland between year 1851 and 2011 (supplementing information). We obtain  $(a, \sigma_{AR}^2) = (0.67, 0.85)$  thus the process (7) has variance [*Box et al., 2008*]  $\sigma_T^2 = \sigma_{AR}^2 / (1 - a^2) = 1.54 \text{ K}^2$  comparable to the observed temperature over Greenland  $\sigma_T^{obs} = 1.55 \text{ K}^2$ .

We find time step size of one year to be sufficient for integrating the Oer03-model (supplementing information); thus  $T_{t+1}$  in (7) represents the temperature one year after  $T_t$ .

To find the steady state volume we run the Oer03-model forward long enough for the ice sheet to reach equilibrium, with and without fluctuating temperatures. The results of this procedure are shown in Figure 1 (left) where it is clearly seen that the steady state volume is lower for simulations with fluctuating temperatures than with constant temperature. We emphasize that the fluctuating temperature time series  $\{T_t\}$  have as mean the constant temperature,  $\langle T_t \rangle = \bar{T}$  so that the results are due to the temperature fluctuation.

In Figure 1 (right) the effect of temperature fluctuations is shown in the  $(T, V)$ -plane: The markers “+” are steady states of numerical simulations with constant temperature, while

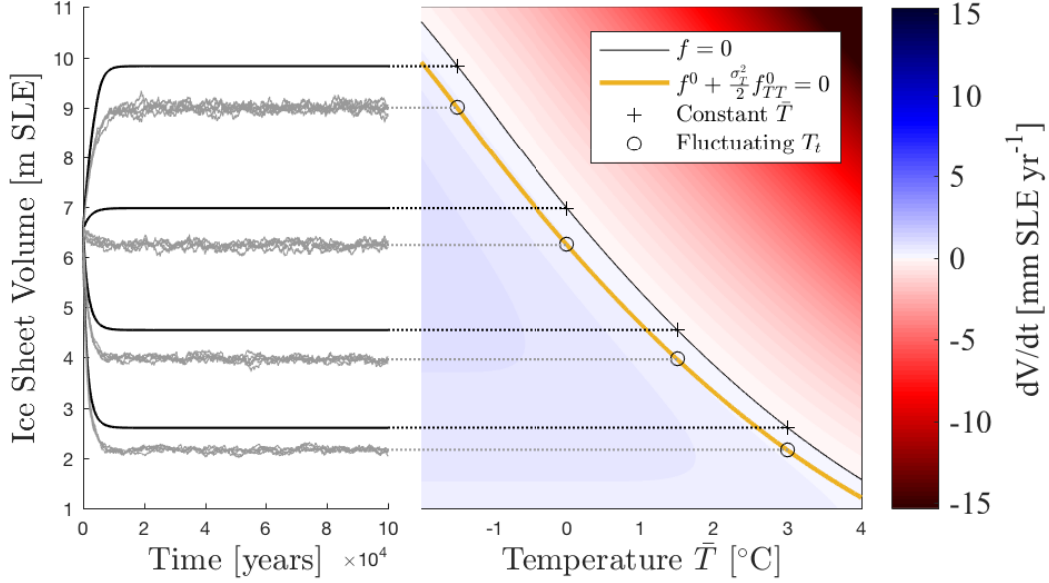


**Figure 1.** (Left) Simulations of the Oer03-model for  $\bar{T} = -1.5, 0, 1.5$  and  $3$ . The black curves denote a constant temperature and the grey curves fluctuating temperatures generated with (7). (Right) The mass balance (Equation 1) for the Oer03-model in the  $(T, V)$ -plane. The black contour is the steady state  $f = dV/dt = 0$ . The markers represent the average of the numerical simulation with constant (+) and fluctuating (o) temperature seen on the left. Finally the yellow contour shows the approximation derived in (5).

the circles represent ensemble averages of simulations with fluctuating temperatures. It is evident that temperature fluctuations decrease the steady state ice volume. The yellow curve in Figure 1 (right) was calculated using (5) and gives a good agreement with the results from ensemble simulations.

In order to illustrate the physics behind (5), consider values of the mass budget function  $f$  for different ice sheet volumes  $V$ , shown in Figure 2. The insert shows, for a particular value of  $V$ , how the steady state is influenced by fluctuating temperatures: The average mass budget of a colder year and a warmer year is less than the mass budget of a year with a temperature corresponding to the average of “cold” and “warm”; to put it another way: the increased SMB of a single anomalously cold year cannot balance the increased melt from an equally anomalously warm year. In particular let  $T_c = \bar{T} - \sigma$  and  $T_h = \bar{T} + \sigma$ :

$$\frac{f(V, T_c) + f(V, T_h)}{2} < f\left(V, \frac{T_c + T_h}{2}\right); \quad (8)$$

this is consistent with  $f^0_{TT} < 0$  as shown in (6).

#### 4 Consequences for Long Term Ice Sheet Simulations

Here we investigate the effect of accounting for fluctuating temperatures when running long time scale climate simulations. These can be either transient runs, scenarios with specified changing  $\text{CO}_2$ -forcing or equilibrium runs with specified constant forcing. Specifically we analyze the results of *Robinson et al.* [2012] where the long term stability of the GrIS is investigated. In this study an ice sheet model is forced by the output of a regional climate

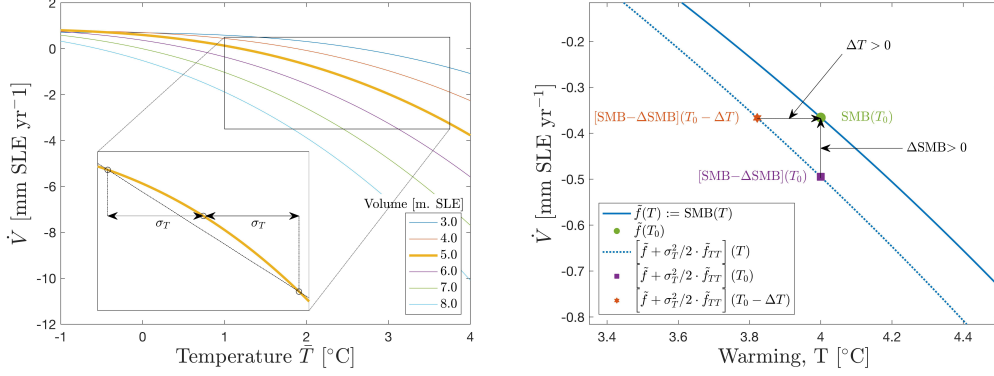


**Figure 2.** **Left:** Mass balance  $\dot{V}$  of the ice sheet for different values of the total ice sheet ice volume  $V$  in the Oer03-model. Similar to Figure 1 but here we show  $\dot{V}$  as a function of  $\bar{T}$  for different total volumes  $V$ . **Insert, left:** The curvature of  $\dot{V}(\bar{T})$  influences the steady state behavior – a cold year does not cancel out the effect of an equally warm year as shown in Eq. 8. The value of  $\sigma_T$  is used for illustration and is given as the square root of the temperature variance,  $\sigma_T = \sqrt{1.54\text{K}^2} = 1.24\text{K}$ . Note the similarity of the  $\dot{V}(\bar{T})$  found here to Figure 6h in *Fettweis et al.* [2013]. **Right:** Estimating the effect of fluctuating temperatures on GrIS projections. The full curve is obtained by fitting a third degree polynomial  $\tilde{f}(T)$  to an  $\text{SMB}(T)$  from *Robinson et al.* [2012]. The dotted line show the effect of temperature fluctuations obtained by applying Eq. (5). For a warming of  $4^\circ\text{C}$  the green circle shows the  $\text{SMB}$ .  $\Delta\text{SMB}$  is obtained by applying Eq. (10) and represents the change in mass balance resulting from the temperature fluctuations.  $-\Delta T$  is the temperature change required to negate this effect and is obtained implicitly from Eq. (11).

model driven by the ERA40 climatology with a constant temperature anomaly applied, see *Robinson et al.* [2012] and Supplementary Information.

As parameters in ice sheet models are often tuned to best match the problem under investigation (eg. *Muresan et al.* [2016]), the ice sheet volume bias we describe may already be implicitly compensated. To estimate the size of the temperature fluctuation bias, we assume that this has not already been accounted for by parameter tuning.

*Fettweis et al.* [2013] compare the output of RCMs forced with multiple future climate scenarios and show that the effect of rising temperature on the GrIS SMB is well described by a third degree polynomial (note the qualitative similarities between Figure 2 and Figure 6h in *Fretwell et al.* [2013]). Here we take the same approach. To the ensemble of simulations in *Robinson et al.* [2012] we fit third degree polynomials to the SMB as a function of temperature at time  $t = 200$  years (supplementing information) and obtain third degree polynomials in  $T$ :

$$\left\{ \tilde{f}_{ij}(T) \mid \tilde{f}_{ij}(T) = A_{ij}T^3 + B_{ij}T^2 + C_{ij}T + D_{ij} \right\} \quad (9)$$

where the indices  $i$  and  $j$  run over two separate parameters in the model that take 9 – respectively 11 – values [*Robinson et al.*, 2012] so in total we have 99 unique polynomial fits. These polynomials are then used as a simple description of the mass balance function as a function of temperature,  $\text{SMB}_{ij}(T) = \tilde{f}_{ij}(T)$ . Differentiating twice we obtain  $\tilde{f}_{TT}(T) = 6AT + 2B$  (suppressing indices  $i, j$  for clarity).

For all parameter pairs  $(i, j)$  we evaluate  $\tilde{f}(T)$  and  $\tilde{f}(T) + (\sigma_T^2/2)\tilde{f}_{TT}(T)$  – this is shown in Figure 2 (right) as the full and dotted lines, respectively.

To illustrate this approach we pick a specific temperature  $T_0$ .  $\tilde{f}(T_0)$  is thus the SMB for a constant temperature and  $\tilde{f}(T_0) + (\sigma_T^2/2)\tilde{f}_{TT}(T_0)$  represents the effect of letting the

temperatures fluctuate. This procedure gives us an expression for  $\Delta\text{SMB}$

$$\begin{aligned}\Delta\text{SMB} &= \tilde{f}(T_0) - \left[ \tilde{f}(T_0) + \frac{\sigma_T^2}{2} \tilde{f}_{TT}(T_0) \right] \\ &= -\frac{\sigma_T^2}{2} \tilde{f}_{TT}(T_0)\end{aligned}\quad (10)$$

where  $\Delta\text{SMB}$  is positive in accordance with (6). Next we find the temperature difference  $\Delta T$  such that

$$\tilde{f}(T_0 - \Delta T) + \frac{\sigma_T^2}{2} \tilde{f}_{TT}(T_0 - \Delta T) = \tilde{f}(T_0). \quad (11)$$

In this way  $\Delta T$  is the *effective* temperature change resulting from considering fluctuating temperatures.

The results of applying the steps outlined above on the data from *Robinson et al.* [2012] are shown in Figure 3 (see also supplementing information). The red curves in Figure 3 shows the most likely  $\Delta T$  and  $\Delta\text{SMB}$ ; the grey curves are estimates for the  $9 \times 11$  individual parameter values and the blue shade area represents the 95% credibility region.

The warmings quoted in *Robinson et al.* [2012] are relative to the preindustrial period whereas the reported warming from the preindustrial period to the present day is estimated to  $1^\circ\text{C}$  [*Stocker et al.*, 2013, p. 78]. Furthermore, as a likely warming from today to the year 2100 can be taken the RCP45 scenario yielding *more likely than not* a further warming of  $2.0^\circ\text{C}$  [*IPCC*, 2013, p. 21]. Combing these numbers we arrive at a warming of  $3.0^\circ\text{C}$  in the year 2100 relative to the preindustrial when considering the RCP45 scenario. For this value it is seen in Figure 3 that an additional  $0.12^\circ\text{C}$  should be added to any constant warming term when considering simulations of the Greenland ice sheet, assuming the same temperature variance as in Section 3 (top). Further, Figure 3 (bottom) shows the most likely  $\Delta\text{SMB}$  resulting from temperature fluctuations at a  $3^\circ\text{C}$  warming to be  $30 \text{ Gt/y}$ . To put this number in context, consider *Barletta et al.* [2013] who report an average GrIS SMB of  $-234 \pm 20 \text{ Gt/y}$  for the period 2003 to 2011.

Observe in Fig. (3) that  $\Delta T$  goes to zero for low temperature anomalies and appears to saturate for higher temperature anomalies. In the framework presented here this can be explained by considering the  $\text{SMB}(T)$ -curves shown in Fig. (2). For low temperature anomalies the  $\text{SMB}(T)$  curve is close to flat so the second derivative is small; this gives a small contribution to  $\Delta\text{SMB}$  from Eq. (10). On the other hand, as the  $\text{SMB}(T)$  curve becomes progressively steeper, a correspondingly smaller  $\Delta T$  in Eq. (11) is required to compensate for  $\Delta\text{SMB}$ .

The results above highlight that interannual temperature variability cannot be neglected in long term studies involving ice sheet models. The straightforward approach would be to simply include the expected temperature variability in a number simulations followed by calculating the ensemble average. Conversely, one could calculate the effect of temperature variability for a range of climate scenarios as a starting point for a following bias adjustment.

## 5 Discussion

### 5.1 Limitations of this study

When calculating the  $\tilde{f}$ 's in (9) and (10) we assume a constant volume in the data from *Robinson et al.* [2012], but in reality the relative variations are as large as 9.5% when considering all the warming temperatures shown in Figure 3 (supplementing information). However to draw the conclusion about the consequences of a  $3^\circ\text{C}$  warming it is adequate to consider warmings less than  $4^\circ\text{C}$  and here the volume variation was less than 3% of the average. Neglecting variations in volume does add uncertainty to our results, and it is not immediately clear to us how to quantify that uncertainty. Additionally, at time  $t = 200$  where we extracted the data the ice sheets in *Robinson et al.* [2012] are not in steady state, expanding the analysis using a data set from ice sheet simulations in steady state would be desirable.

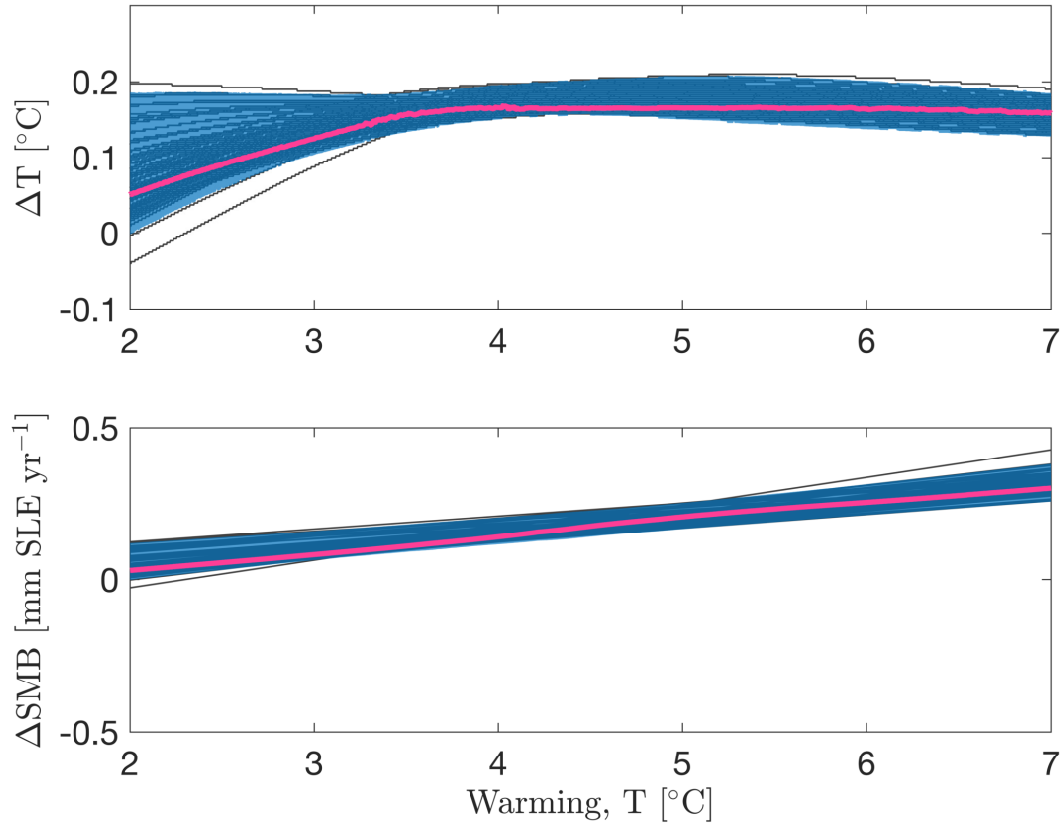


**Figure 3.** Maximum likelihood estimates of  $\Delta T$  and  $\Delta \text{SMB}$  (red curves). The grey curves are estimates from individual simulations and the blue shaded area denotes 95% credibility regions.

The temperature fluctuation is accounted for in most studies either explicitly [Ridley et al., 2010; Seguinot, 2013] or implicitly in the tuning of the surface mass balance scheme. Our result may be used to explicitly implement the contribution from the temperature fluctuations in the mass balance schemes before bias correcting due to other possible model deficiencies.

## 5.2 Conclusion and outlook

From a theoretical argument and by considering a minimal ice sheet model we have shown that fluctuating temperatures forcing the ice sheet have an effect on the steady state volume of the ice sheet.

The effect is explained by the curvature, or second derivative, of the mass balance as a function of temperature. A negative curvature gives rise to nonlinear effects meaning that the average mass accumulation resulting from a cold year and a warm year in succession is less than the mass accumulation of two consecutive years having the average temperature of the “warm” and “cold” years.

Even though we considered a simple ice sheet model, the results are transferable to other more realistic models as long as the rather weak assumptions leading up to (5) hold. E.g. models of sub-shelf melting, grounding line migration, and ice discharge respond very non-linearly to changes in ocean temperatures [Favier et al., 2014; Joughin et al., 2014; Seroussi et al., 2014; Mengel and Levermann, 2014; Pollard et al., 2015; Fogwill et al., 2014], thus it is critical to take variability into account for quantitative assessments.

The response of a real ice sheet to temperature increase is naturally much more complex than what can be described in a simple study such as the present paper. In a model study *Born and Nisancioglu* [2012] observe mass loss acceleration of the Northeastern GrIS as a response to warming. This part of the GrIS experiences comparatively little precipitation and thus increasing melt is not compensated by increasing accumulation. However, the opposite has been shown to be the case for Antarctica. *Frieler et al.* [2015] show that increasing temperatures will *increase* Antarctic SMB at continental scales due to increasing precipitation. This is an interesting special case of an accumulation dominated mass balance, where the curvature term in Eq. (5) has the opposite sign, thus an underestimated temperature fluctuation would lead to an underestimation of the growth of the ice sheet.

We have evaluated the consequences of the temperature fluctuation bias on long-term GrIS simulations and found that, if the full effects are taken into account with no further modifications, a significant *effective* temperature change would be required for an unbiased estimation of the equilibrium ice volume. Peter: Skulle vi gentage vores talestimator p temperatur stigning og masse tab her?

### Acknowledgments

We would like to thank Johannes Oerlemans for providing the original code for his model and Alexander Robinson for being very helpful in providing the data from their study.

Furthermore we are very thankful for valuable comment from the anonymous reviewers.

This work is part of the Dynamical Systems Interdisciplinary Network (DSIN) – T.M. was financially supported by the Centre for Ice and Climate and the DSIN, both University of Copenhagen.

The authors declare no conflict of interest.

<https://bitbucket.org/bogeholm/ice-sheets-fluctuating-temp> contains the code used for this study.

### References

- Abe-Ouchi, A., F. Saito, K. Kawamura, M. E. Raymo, J. Okuno, K. Takahashi, and H. Blatter (2013), Insolation-driven 100,000-year glacial cycles and hysteresis of ice-sheet volume, *Nature*, *500*, 190–193, doi:10.1038/nature12374.
- Applegate, P. J., B. R. Parizek, R. E. Nicholas, R. B. Alley, and K. Keller (2014), Increasing temperature forcing reduces the greenland ice sheet’s response time scale, *Climate Dynamics*, *45*(7-8), 2001–2011, doi:10.1007/s00382-014-2451-7.
- Bamber, J. L., and W. P. Aspinall (2013), An expert judgement assessment of future sea level rise from the ice sheets, *Nature Climate Change*, *3*, 424–427, doi:10.1038/nclimate1778.
- Bamber, J. L., J. A. Griggs, R. T. W. L. Hurkmans, J. A. Dowdeswell, S. P. Gogineni, I. Howat, J. Mouginot, J. Paden, S. Palmer, E. Rignot, and D. Steinhage (2013), A new bed elevation dataset for greenland, *The Cryosphere*, *7*, 499–510, doi:10.5194/tc-7-499-2013.
- Barletta, V. R., L. S. Sørensen, and R. Forsberg (2013), Scatter of mass changes estimates at basin scale for greenland and antarctica, *The Cryosphere*, *7*, 1411–1432, doi:10.5194/tc-7-1411-2013.
- Bierman, P. R., J. D. Shakun, L. B. Corbett, S. R. Zimmerman, and D. H. Rood (2016), A persistent and dynamic East Greenland Ice Sheet over the past 7.5 million years, *Nature*, *540*, 256–260, doi:10.1038/nature20147.
- Blard, P.-H., G. Leduc, and N. Glasser (2016), Climate science: The history of Greenland’s ice, *Nature*, *540*, 202–203, doi:10.1038/540202a.
- Born, A., and K. H. Nisancioglu (2012), Melting of northern greenland during the last interglaciation, *The Cryosphere*, *6*, 1239–1250, doi:10.5194/tc-6-1239-2012.

- Box, G. E. P., G. M. Jenkins, and G. C. Reinsel (2008), *Time Series Analysis - Forecasting and Control*, fourth edition ed., John Wiley & Sons, Inc.
- Church, J., P. Clark, A. Cazenave, J. Gregory, S. Jevrejeva, A. Levermann, M. Merrifield, G. Milne, R. Nerem, P. Nunn, A. Payne, W. Pfeffer, D. Stammer, and A. Unnikrishnan (2013), *Sea Level Change*, book section 13, pp. 1137–1216, Cambridge University Press, Cambridge, United Kingdom and New York, NY, USA, doi:10.1017/CBO9781107415324.026.
- Dahl-Jensen, D., M. R. Albert, a. Aldahan, N. Azuma, D. Balslev-Clausen, M. Baumgartner, a. M. Berggren, M. Bigler, T. Binder, T. Blunier, J. C. Bourgeois, E. J. Brook, S. L. Buchardt, C. Buizert, E. Capron, J. Chappellaz, J. Chung, H. B. Clausen, I. Cvijanovic, S. M. Davies, P. Ditlevsen, O. Eicher, H. Fischer, D. a. Fisher, L. G. Fleet, G. Gfeller, V. Gkinis, S. Gogineni, K. Goto-Azuma, a. Grinsted, H. Gudlaugsdottir, M. Guillevic, S. B. Hansen, M. Hansson, M. Hirabayashi, S. Hong, S. D. Hur, P. Huybrechts, C. S. Hvidberg, Y. Iizuka, T. Jenk, S. J. Johnsen, T. R. Jones, J. Jouzel, N. B. Karlsson, K. Kawamura, K. Keegan, E. Kettner, S. Kipfstuhl, H. a. Kjæ r, M. Koutnik, T. Kuramoto, P. Köhler, T. Laepple, a. Landais, P. L. Langen, L. B. Larsen, D. Leuenberger, M. Leuenberger, C. Leuschen, J. Li, V. Lipenkov, P. Martinerie, O. J. Maselli, V. Masson-Delmotte, J. R. McConnell, H. Miller, O. Mini, a. Miyamoto, M. Montagnat-Rentier, R. Mulvaney, R. Muscheler, a. J. Orsi, J. Paden, C. Panton, F. Pattyn, J.-R. Petit, K. Pol, T. Popp, G. Possnert, F. Prié, M. Prokopiou, a. Quiquet, S. O. Rasmussen, D. Raynaud, J. Ren, C. Reutenauer, C. Ritz, T. Röckmann, J. L. Rosen, M. Rubino, O. Rybak, D. Samyn, C. J. Sapart, a. Schilt, a. M. Z. Schmidt, J. Schwander, S. Schüpbach, I. Seierstad, J. P. Severinghaus, S. Sheldon, S. B. Simonsen, J. Sjolte, a. M. Solgaard, T. Sowers, P. Sperlich, H. C. Steen-Larsen, K. Steffen, J. P. Steffensen, D. Steinhage, T. F. Stocker, C. Stowasser, a. S. Sturevik, W. T. Sturges, a. Sveinbjörnsdottir, a. Svensson, J.-L. Tison, J. Uetake, P. Vallelonga, R. S. W. van de Wal, G. van der Wel, B. H. Vaughn, B. Vinther, E. Waddington, a. Wegner, I. Weikusat, J. W. C. White, F. Wilhelms, M. Winstrup, E. Witrant, E. W. Wolff, C. Xiao, and J. Zheng (2013), Eemian interglacial reconstructed from a Greenland folded ice core, *Nature*, 493(7433), 489–494, doi:10.1038/nature11789.
- Eakins, B., and G. Sharman (2010), Volumes of the world's oceans from etopo1.
- Favier, L., G. Durand, S. L. Cornford, G. H. Gudmundsson, O. Gagliardini, F. Gillet-Chaulet, T. Zwinger, a. J. Payne, and a. M. Le Brocq (2014), Retreat of Pine Island Glacier controlled by marine ice-sheet instability, *Nature Climate Change*, 4, 117–121, doi:10.1038/nclimate2094.
- Fettweis, X., B. Franco, M. Tedesco, J. H. van Angelen, J. T. M. Lenaerts, M. R. van den Broeke, and H. Gallée (2013), Estimating Greenland ice sheet surface mass balance contribution to future sea level rise using the regional atmospheric climate model MAR, *The Cryosphere*, 7, 469–489, doi:10.5194/tc-7-469-2013.
- Fogwill, C. J., C. S. M. Turney, K. J. Meissner, N. R. Golledge, P. Spence, J. L. Roberts, M. H. England, R. T. Jones, and L. Carter (2014), Testing the sensitivity of the East Antarctic Ice Sheet to Southern Ocean dynamics: Past changes and future implications, *Journal of Quaternary Science*, 29(1), 91–98, doi:10.1002/jqs.2683.
- Foster, G., and E. Rohling (2012), Relationship between sea level and climate forcing by CO<sub>2</sub> on geological timescales, *Proceedings of the National Academy of Sciences*, 110(4), 1209–1214, doi:10.1073/pnas.1216073110.
- Frankignoul, C., and K. Hasselmann (1977), Stochastic climate models, part ii – application to sea-surface temperature anomalies and thermocline variability, *Tellus*, 29(4), 289–305, doi:10.1111/j.2153-3490.1977.tb00740.x.
- Fretwell, P., H. D. Pritchard, D. G. Vaughan, J. L. Bamber, N. E. Barrand, R. Bell, C. Bianchi, R. G. Bingham, D. D. Blankenship, G. Casassa, G. Catania, D. Callens, H. Conway, a. J. Cook, H. F. J. Corr, D. Damaske, V. Damm, F. Ferraccioli, R. Forsberg, S. Fujita, Y. Gim, P. Gogineni, J. a. Griggs, R. C. a. Hindmarsh, P. Holmlund, J. W. Holt, R. W. Jacobel, a. Jenkins, W. Jokat, T. Jordan, E. C. King, J. Kohler, W. Krabill, M. Riger-Kusk, K. a. Langley, G. Leitchenkov, C. Leuschen, B. P. Luyendyk, K. Matsuoka, J. Mouginot, F. O. Nitsche, Y. Nogi, O. a. Nost, S. V. Popov, E. Rignot, D. M. Rippin, a. Rivera, J. Roberts,

- N. Ross, M. J. Siegert, a. M. Smith, D. Steinhage, M. Studinger, B. Sun, B. K. Tinto, B. C. Welch, D. Wilson, D. a. Young, C. Xiangbin, and a. Zirizzotti (2013), Bedmap2: Improved ice bed, surface and thickness datasets for Antarctica, *The Cryosphere*, 7(1), 375–393, doi:10.5194/tc-7-375-2013.
- Frieler, K., P. U. Clark, F. He, C. Buizert, R. Reese, S. R. M. Ligtenberg, M. R. van den Broeke, R. Winkelmann, and A. Levermann (2015), Consistent evidence of increasing antarctic accumulation with warming, *Nature Climate Change*, 5, 348–352, doi:10.1038/NCLIMATE2574.
- Fyke, J. G., Miren, Vizcaíno, W. Lipscomb, and S. Price (2014), Future climate warming increases greenland ice sheet surface mass balance variability, *Geophysical Research Letters*, 41(2), 470–475, doi:10.1002/2013GL058172.
- Gasson, E., M. Siddall, D. J. Lunt, O. J. L. Rackham, and C. H. Lear (2012), Exploring Uncertainties in the Relationship Between Temperature, Ice Volume, and Sea Level Over the Past 50 Million Years, *Reviews of Geophysics*, 50(RG1005), 1–35, doi:10.1029/2011rg000358.
- Greenbaum, J. S., D. D. Blankenship, D. a. Young, T. G. Richter, J. L. Roberts, a. R. a. Aitken, B. Legresy, D. M. Schroeder, R. C. Warner, T. D. van Ommen, and M. J. Siegert (2015), Ocean access to a cavity beneath Totten Glacier in East Antarctica, *Nature Geoscience*, 8(4), 294–298, doi:10.1038/NGEO2388.
- Gregory, J. M., and P. Huybrechts (2006), Ice-sheet contributions to future sea-level change., *Philosophical Transactions of the Royal Society A: Mathematical, Physical and Engineering Sciences*, 364(1844), 1709–1731, doi:10.1098/rsta.2006.1796.
- Gregory, J. M., O. J. H. Browne, A. J. Payne, J. K. Ridley, and I. C. Rutt (2012), Modelling large-scale ice-sheet–climate interactions following glacial inception, *Climate of the Past*, 8(5), 1565–1580, doi:10.5194/cp-8-1565-2012.
- Hasselmann, K. (1976), Stochastic climate models – part i. theory, *Tellus A*, 28(6), 473–485, doi:10.3402/tellusa.v28i6.11316.
- Hock, R. (2003), Temperature index melt modelling in mountain areas, *Journal of Hydrology*, 282(1–4), 104–115, doi:10.1016/S0022-1694(03)00257-9.
- Höll, M., and H. Kantz (2015), The fluctuation function of the detrended fluctuation analysis - Investigation on the AR ( 1 ) process, *European Physical Journal B*, 88(5), 1–15, doi:10.1140/epjb/e2015-60143-1.
- Huybrechts, P., and J. de Wolde (1999), The dynamic response of the Greenland and Antarctic ice sheets to multiple-century climatic warming, *Journal of Climate*, 12(8), 2169–2188.
- IPCC (2013), *Summary for Policymakers*, book section SPM, pp. 1–30, Cambridge University Press, Cambridge, United Kingdom and New York, NY, USA, doi:10.1017/CBO9781107415324.004.
- Joughin, I., B. E. Smith, D. E. Shean, and D. Floricioiu (2014), Brief communication: Further summer speedup of Jakobshavn Isbræ, *The Cryosphere*, 8(1), 209–214, doi:10.5194/tc-8-209-2014.
- Kageyama, M., S. Charbit, C. Ritz, M. Khodri, and G. Ramstein (2004), Quantifying ice-sheet feedbacks during the last glacial inception, *Geophysical Research Letters*, 31(L24203), 1–4, doi:10.1029/2004GL021339.
- (KNMI), R. N. M. I. (2015), Knmi climate explorer.
- Kopp, R. E., F. J. Simons, J. X. Mitrovica, A. C. Maloof, and M. Oppenheimer (2009), Probabilistic assessment of sea level during the last interglacial stage., *Nature*, 462(7275), 863–867, doi:10.1038/nature08686.
- Meinshausen, M., S. J. Smith, K. Calvin, J. S. Daniel, M. L. T. Kainuma, J. Lamarque, K. Matsumoto, S. a. Montzka, S. C. B. Raper, K. Riahi, a. Thomson, G. J. M. Velders, and D. P. P. van Vuuren (2011), The RCP greenhouse gas concentrations and their extensions from 1765 to 2300, *Climatic Change*, 109(1–2), 213–241, doi:10.1007/s10584-011-0156-z.
- Mengel, M., and A. Levermann (2014), Ice plug prevents irreversible discharge from East Antarctica, *Nature Climate Change*, 4(6), 451–455, doi:10.1038/nclimate2226.
- Mouginot, J., E. Rignot, and B. Scheuchl (2014), Sustained increase in ice discharge from the amundsen sea embayment, west antarctica, from 1973 to 2013, *Geophysical Research*

- Letters*, 41(5), 1576–1584, doi:10.1002/2013GL059069.
- Mudelsee, M. (2010), *Climate Time Series Analysis - Classical Statistical and Bootstrap Methods*, Springer, doi:10.1007/978-90-481-9482-7.
- Muresan, I. S., S. A. Khan, A. Aschwanden, C. Khroulev, T. V. Dam, J. Bamber, M. R. van den Broeke, B. Wouters, P. K. Munneke, and K. H. Kjær (2016), Modelled glacier dynamics over the last quarter of a century at jakobshavn isbræ, *The Cryosphere*, 10(2), 597–611, doi:10.5194/tc-10-597-2016.
- NOAA (2015), Greenland ice sheet.
- Oerlemans, J. (2003), A quasi-analytical ice-sheet model for climate studies, *Nonlinear Processes in Geophysics*, 10(4/5), 441–452, doi:10.5194/npg-10-441-2003.
- Oerlemans, J. (2008), *Minimal Glacier Models*, second print in march 2011 (with some revisions) ed., Igitur, Utrecht Publishing & Archiving Services, Universiteitsbibliotheek Utrecht.
- Pollard, D., I. Muszynski, S. H. Schneider, and S. L. Thompson (1990), Asynchronous coupling of ice-sheet and atmospheric forcing models, *Annals of Glaciology*, 14, 247–251, doi:10.1017/s0260305500008685.
- Pollard, D., R. M. DeConto, and R. B. Alley (2015), Potential antarctic ice sheet retreat driven by hydrofracturing and ice cliff failure, *Earth and Planetary Science Letters*, 412, 112 – 121, doi:10.1016/j.epsl.2014.12.035.
- Ridley, J., J. M. Gregory, P. Huybrechts, and J. Lowe (2010), Thresholds for irreversible decline of the Greenland ice sheet, *Climate Dynamics*, 35(6), 1049–1057, doi:10.1007/s00382-009-0646-0.
- Ridley, J. K., P. Huybrechts, J. M. Gregory, and J. A. Lowe (2005), Elimination of the Greenland Ice Sheet in a High CO<sub>2</sub> Climate, *Journal of Climate*, 18(17), 3409–3427, doi:10.1175/JCLI3482.1.
- Rignot, E., J. Mouginot, M. Morlighem, H. Seroussi, and B. Scheuchl (2014), Widespread, rapid grounding line retreat of Pine Island, Thwaites, Smith, and Kohler glaciers, West Antarctica, from 1992 to 2011, *Geophysical Research Letters*, 41(10), 3502–3509, doi:10.1002/2014GL060140.
- Robinson, A., R. Calov, and A. Ganopolski (2012), Multistability and critical thresholds of the Greenland ice sheet, *Nature Climate Change*, 2(6), 429–432, doi:10.1038/nclimate1449.
- Roche, D. M., C. Dumas, M. Bügelmayer, S. Charbit, and C. Ritz (2014), Adding a dynamical cryosphere to iloveclim (version 1.0): coupling with the grisli ice-sheet model, *Geoscientific Model Development*, 7(4), 1377–1394, doi:10.5194/gmd-7-1377-2014.
- Rodriguez, R., and H. C. Tuckwell (1996), Statistical properties of stochastic nonlinear dynamical models of single spiking neurons and neural networks, *Physical Review E*, 54(5), 5585–5590, doi:10.1103/physreve.54.5585.
- Roe, G. H., and M. O’Neal (2005), The response of glaciers to intrinsic climate variability: observations and models of late-holocene variations in the pacific northwest, *Journal of Glaciology*, 55(193), 839–854, doi:10.3189/002214309790152438.
- Ruddiman, W. F. (2014), *Earth’s Climate - Past and Future*, 3rd edition ed., W.H. Freeman.
- Schaefer, J. M., R. C. Finkel, G. Balco, R. B. Alley, M. W. Caffee, J. P. Briner, N. E. Young, A. J. Gow, and R. Schwartz (2016), Greenland was nearly ice-free for extended periods during the Pleistocene, *Nature*, 540, 252–255, doi:10.1038/nature20146.
- Seguinot, J. (2013), Spatial and seasonal effects of temperature variability in a positive degree-day glacier surface mass-balance model, *Journal of Glaciology*, 59(218), 1202–1204, doi:10.3189/2013JoG13J081.
- Seroussi, H., M. Morlighem, E. Rignot, J. Mouginot, E. Larour, M. Schodlok, and A. Khazendar (2014), Sensitivity of the dynamics of Pine Island Glacier, West Antarctica, to climate forcing for the next 50 years, *The Cryosphere*, 8(5), 1699–1710, doi:10.5194/tc-8-1699-2014.
- Solgaard, A. M., and P. L. Langen (2012), Multistability of the Greenland ice sheet and the effects of an adaptive mass balance formulation, *Climate Dynamics*, 39(7–8), 1599–1612, doi:10.1007/s00382-012-1305-4.

- Stocker, T., D. Qin, G.-K. Plattner, L. Alexander, S. Allen, N. Bindoff, F.-M. Bréon, J. Church, U. Cubasch, S. Emori, P. Forster, P. Friedlingstein, N. Gillett, J. Gregory, D. Hartmann, E. Jansen, B. Kirtman, R. Knutti, K. Krishna Kumar, P. Lemke, J. Marotzke, V. Masson-Delmotte, G. Meehl, I. Mokhov, S. Piao, V. Ramaswamy, D. Randall, M. Rhein, M. Rojas, C. Sabine, D. Shindell, L. Talley, D. Vaughan, and S.-P. Xie (2013), *Technical Summary*, book section TS, pp. 33–115, Cambridge University Press, Cambridge, United Kingdom and New York, NY, USA, doi:10.1017/CBO9781107415324.005.
- Strugnell, J. M., P. C. Watts, P. J. Smith, and A. L. Allcock (2012), Persistent genetic signatures of historic climatic events in an Antarctic octopus, *Molecular Ecology*, *21*(11), 2775–2787, doi:10.1111/j.1365-294X.2012.05572.x.
- Sun, S., S. L. Cornford, Y. Liu, and J. C. Moore (2014), Dynamic response of Antarctic ice shelves to bedrock uncertainty, *The Cryosphere*, *8*(4), 1561–1576, doi:10.5194/tc-8-1561-2014.
- Vernon, C. L., J. L. Bamber, J. E. Box, M. R. van den Broeke, X. Fettweis, E. Hanna, and P. Huybrechts (2013), Surface mass balance model intercomparison for the greenland ice sheet, *The Cryosphere*, *7*, 599–614, doi:10.5194/tc-7-599-2013.
- Vizcaino, M., U. Mikolajewicz, F. Ziemen, C. B. Rodehacke, R. Greve, and M. R. van den Broeke (2015), Coupled simulations of greenland ice sheet and climate change up to a.d. 2300, *Geophysical Research Letters*, *42*(10), 3927–3935, doi:10.1002/2014gl061142.
- von Storch, H., and F. W. Zwiers (2003), *Statistical Analysis in Climate Research*, netlibrary edition ed., Cambridge University Press.
- Wake, L., and S. Marshall (2015), Assessment of current methods of positive degree-day calculation using in situ observations from glaciated regions, *Journal of Glaciology*, *61*(226), 329–344, doi:10.3189/2015JoG14J116.
- Ziemen, F. A., C. B. Rodehacke, and U. Mikolajewicz (2014), Coupled ice sheet–climate modeling under glacial and pre-industrial boundary conditions, *Climate of the Past*, *10*(5), 1817–1836, doi:10.5194/cp-10-1817-2014.



## Appendix E

# Supporting Information for “Influence of temperature fluctuations on equilibrium ice sheet volume”

1 **Supporting Information for**  
 2 **“Influence of temperature fluctuations on equilibrium volume in conceptual**  
 3 **ice sheet model”**

4 **Troels Bøgeholm Mikkelsen<sup>1</sup>, Aslak Grinsted<sup>1</sup> and Peter D. Ditlevsen<sup>1</sup>**

5 <sup>1</sup>Centre for Ice and Climate, Niels Bohr Institute, Juliane Maries Vej 30, DK-2100 Copenhagen Ø

6 **Contents**

- 7 1. The *Oer03* model  
 8 2. Observed Fluctuations in Greenland Temperature  
 9 3. Evaluation of Neglected Terms in Equation 5)  
 10 4. Analysis of *Robinson et al.* [2012]’s Data  
 11 5. References

12 **The *Oer03* model**

13 The *Oer03* model is introduced in *Oerlemans* [2003] – some details are briefly summa-  
 14 rized here. The model is “highly parameterized” and coupled to the surrounding climate by  
 15 the altitude of the runoff line. Effectively the model consists of three steps: 1) describing the  
 16 shape of the ice sheet, 2) analytically integrating the mass balance over the ice sheet and 3),  
 17 numerically integrating the resulting expression for  $dR/dt$  where  $R$  is the radius of the ice  
 18 sheet; the volume  $V$  is then uniquely determined from  $R$ .

19 Above the runoff line the accumulation is constant, below the balance gradient is con-  
 20 stant; this is illustrated in Figure 1. The ice sheet is axially symmetric and rests on a sloping  
 21 bed; furthermore ice is assumed to be a perfectly plastic material [*Oerlemans*, 2003].

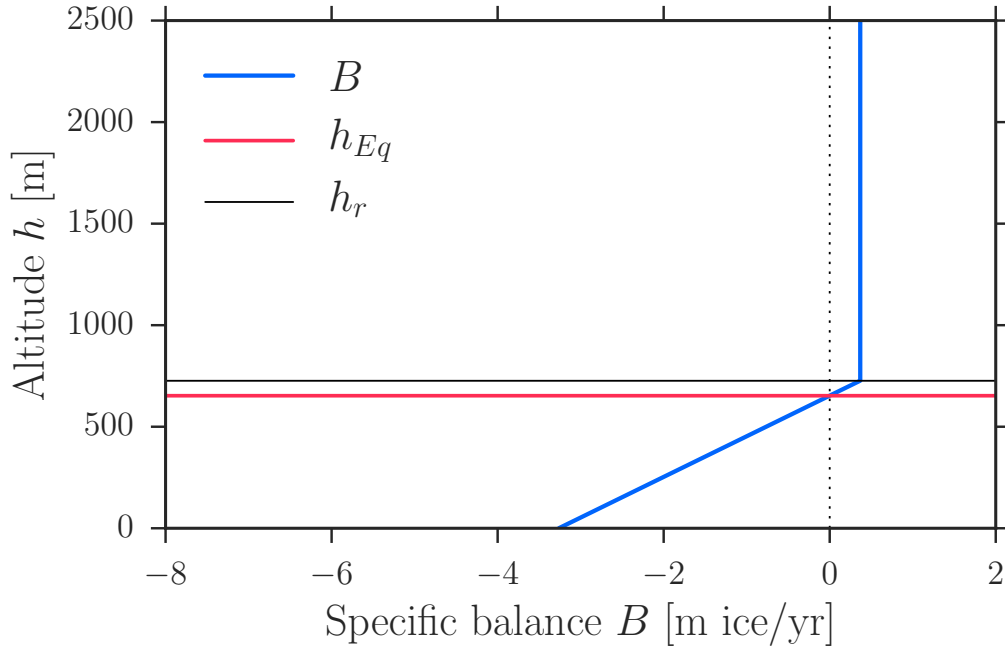
22 The parameters we use are shown in Table 1. We have kept most parameters fixed  
 23 as compared to *Oerlemans* [2003] but changed a total of 7 values to crudely approximate  
 24 Greenland – note that we do not claim to be able to make accurate predictions of the GrIS  
 25 even with this parametrisation. The temperature  $\bar{T} = 5.8^\circ\text{C}$  has been chosen so that no  
 26 temperature anomaly (i.e. setting  $T = 0$  in Equation 2) gives a equilibrium volume of about  
 27 7m SLE, corresponding roughly to the GrIS [*Church et al.*, 2013].

---

Corresponding author: Troels B. Mikkelsen, bogeholm@nbi.ku.dk

Name	Unit	Value	Notes
$A_0$	m ice yr <sup>-1</sup>	1.0 <sup>†</sup>	Characteristic specific balance.
$\beta$	m ice yr <sup>-1</sup> m <sup>-1</sup>	0.005 <sup>†</sup>	Specific balance gradient.
$c$	m <sup>1/2</sup>	$2 \times 10^6$ <sup>†</sup>	Bed slope effect parameter.
$C_R$	m	$5 \times 10^5$ <sup>†</sup>	$e$ -folding radius for “desert effect” from large ice sheets; see Eq. 3
$d_0$	m	$= h_{E,0}$ *)	Undisturbed bed height at center of ice sheet.
$h_{Eq}$	m	See Eq. 2 *)	Height of equilibrium line.
$h_{E,0}$	m	1545 *)	Equilibrium line height at $T = 0$ . Approximate 1990 - 2010 average
$f$	yr <sup>-1</sup>	0.5 <sup>+</sup>	Bulk flow parameter related to ice discharge.
$\mu_0$	m <sup>1/2</sup>	8 <sup>†</sup>	Bed slope effect parameter.
$\mu = \mu_0 + cs^2$			Equation 4 in <i>Oerlemans</i> [2003]
$\rho_i$	kg m <sup>-3</sup>	900 <sup>+</sup>	Density of ice.
$\rho_w$	kg m <sup>-3</sup>	1025 <sup>+</sup>	Density of sea water.
$\rho_m$	kg m <sup>-3</sup>	3500 <sup>+</sup>	Density of bedrock.
$r_c$	m	$8 \times 10^5$ *)	Continental radius. Approximate width of Greenland.
$r_{gr}$	m	$8 \times 10^5$ *)	Initial value – dynamical value in the model.
$s$	m/m	$d_0/r_c \approx 0.002$ *)	Bed slope.
$\bar{T}$	°C	5.8*)	Temperature offset.

28 **Table 1.** <sup>†</sup>: Suggested in *Oerlemans* [2003]. <sup>+</sup>: suggested in private communication with Hans Oerlemans.  
 29 \*) : chosen by the present authors.



30 **Figure 1.** Specific balance  $B$  for  $\bar{T} = 0$  resulting from the parameters in Table 1 and Equations 2, 3 and  
 31 4. For  $h \leq h_R$  we have  $B = A$ , whereas for  $h < h_R$ ,  $B = A - \beta(h_R - h)$  (Equation 14 in *Oerlemans*  
 32 [2003].) Above the runoff line  $h_r$  the specific balance is constant, below  $h_r$  the balance gradient is constant.  
 33  $h_{Eq}$  denotes the equilibrium line.

34 Steps 1 through 11 below describe the *Oer03* model setting used – these steps describe  
 35 calculations performed at every time step that give an expression for

$$\frac{dR}{dt} = f(T, R); \quad (1)$$

36  $dR/dt$  is then integrated using the Euler scheme with a time step of 1 year. We find that using  
 37 a smaller time step size than this only produce negligible differences – see Figure 2 for an  
 38 example.

39 1. We couple the ice sheet to the ambient temperature by introducing the following rela-  
 40 tionship between temperature and height of the equilibrium line [*Oerlemans*, 2008]:

$$h_{Eq} = h_{E,0} + (T - \bar{T}) \cdot 1000/6.5. \quad (2)$$

41 Equation 2 represents an increase of the equilibrium line altitude of approximately 154  
 42 m °C<sup>-1</sup>.

43 2. Equation 3 reflects that the accumulation rate will likely decrease for a large ice sheet  
 44 (Equation 20 in *Oerlemans* [2003]):

$$A \leftarrow A_0 e^{-R/R_C}. \quad (3)$$

45 3. Height of the runoff line (Equation 15 in *Oerlemans* [2003]):

$$h_R \leftarrow h_{Eq} + A/\beta. \quad (4)$$

46 4. Height of the bedrock where the ice sheet ends:

$$h_E \leftarrow d_0 - sR. \quad (5)$$

47 5. Location where the runoff line intersects the ice sheet surface (Equation 17 in *Oerle-*  
 48 *mans* [2003]):

$$r_R \leftarrow R - (h_R - h_E)^2/\mu. \quad (6)$$

49 6. Check if the ice sheet extends into the sea, i.e. if  $R > r_c$ . If so, use Equation (7) in  
 50 *Oerlemans* [2003] to define the radial coordinate of the grounding line  $r_{gr}$ :

51 • **if**  $R > r_c$ :

$$r_{gr} = R - h_E^2/\mu. \quad (7)$$

52 7. If the radial coordinate of the runoff line is larger than of the grounding line, set runoff  
 53 coordinate to grounding coordinate:

54 • **if**  $r_R > r_{gr}$ :

$$r_R \leftarrow r_{gr}. \quad (8)$$

55 8. If the height of the runoff line is smaller than the height of ice sheet termination, set  
 56 radial coordinate of the runoff line to radius of the ice sheet:

57 • **if**  $h_R < h_E$

$$r_R \leftarrow R. \quad (9)$$

58 9. If  $R < r_c$  the ice sheet is continental. Equations 10 and 11 are included for numerical  
 59 reasons.

60 • **if**  $R \leq r_c$

61 – **if**  $r_R < 0$

$$r_R \leftarrow 0 \quad (10)$$

62 – **if**  $R < 1$

$$R \leftarrow 1 \quad (11)$$

63

 – Calculate total  $dV/dt = B_{tot}$ :

$$B_{tot} \leftarrow \pi AR^2 \quad (12)$$

$$- \pi \beta (h_R - h_E) (R^2 - r_R^2) \quad (13)$$

$$+ \frac{4\pi\beta\mu^{1/2}}{5} (R - r_R)^{5/2} \quad (14)$$

$$- \frac{4\pi\beta\mu^{1/2}}{3} R (R - r_R)^{3/2}. \quad (15)$$

$$(16)$$

64

 10. If  $R > r_c$  the the ice sheet extends into the sea:

65

 • if  $R > r_c$ 

$$B_{tot} \leftarrow \pi Ar_{gr}^2 \quad (17)$$

$$- \pi \beta (h_R - h_E) (r_{gr}^2 - r_R^2) \quad (18)$$

$$+ \frac{4\pi\beta\mu^{1/2}}{5} \left( (R - r_R)^{5/2} - (R - r_{gr})^{5/2} \right) \quad (19)$$

$$- \frac{4\pi\beta\mu^{1/2}}{3} \left( R (R - r_R)^{3/2} - R (R - r_{gr})^{3/2} \right) \quad (20)$$

$$- 2\pi r_{gr} \left( \frac{\rho_w}{\rho_i} \right) f (sr_{gr} - d_0)^2. \quad (21)$$

66

 Here the last term corresponds to Equation 19 in *Oerlemans* [2003] and is related to the flux across the grounding line.

67

68

 11. Relationship between  $\frac{dR}{dt}$  and  $B_{tot}$ , corresponding to Equation 13 in *Oerlemans* [2003]:

69

 • if  $R \leq r_c$ 

$$Q \leftarrow \pi \left( 1 + \frac{\rho_i}{\rho_m - \rho_i} \right) \left( \frac{4}{3} \mu^{1/2} R^{3/2} - sR^2 \right), \quad (22)$$

$$\frac{dR}{dt} \leftarrow B_{tot}/Q. \quad (23)$$

70

 • if  $R > r_c$ 

$$Q \leftarrow \pi \left( 1 + \frac{\rho_i}{\rho_m - \rho_i} \right) \left( \frac{4}{3} \mu^{1/2} R^{3/2} - sR^2 \right) \quad (24)$$

$$- 2 \frac{\rho_w}{\rho_m - \rho_i} (\pi s R^2 - d_0 R), \quad (25)$$

$$\frac{dR}{dt} \leftarrow B_{tot}/Q. \quad (26)$$

71

72

73

 Integrating steps 1-11 yield a time series of the ice sheet radius. To convert to volume we use the following relations (Equations 9, 11 and 12 in *Oerlemans* [2003]); the volume of the continental part of the ice sheet:

$$V_{cont} = \frac{8\pi\mu^{1/2}}{15} R^{5/2} - \frac{1}{3} \pi s R^3. \quad (27)$$

74

In the case of the ice extending to the sea, the volume of the sea water replaced by ice:

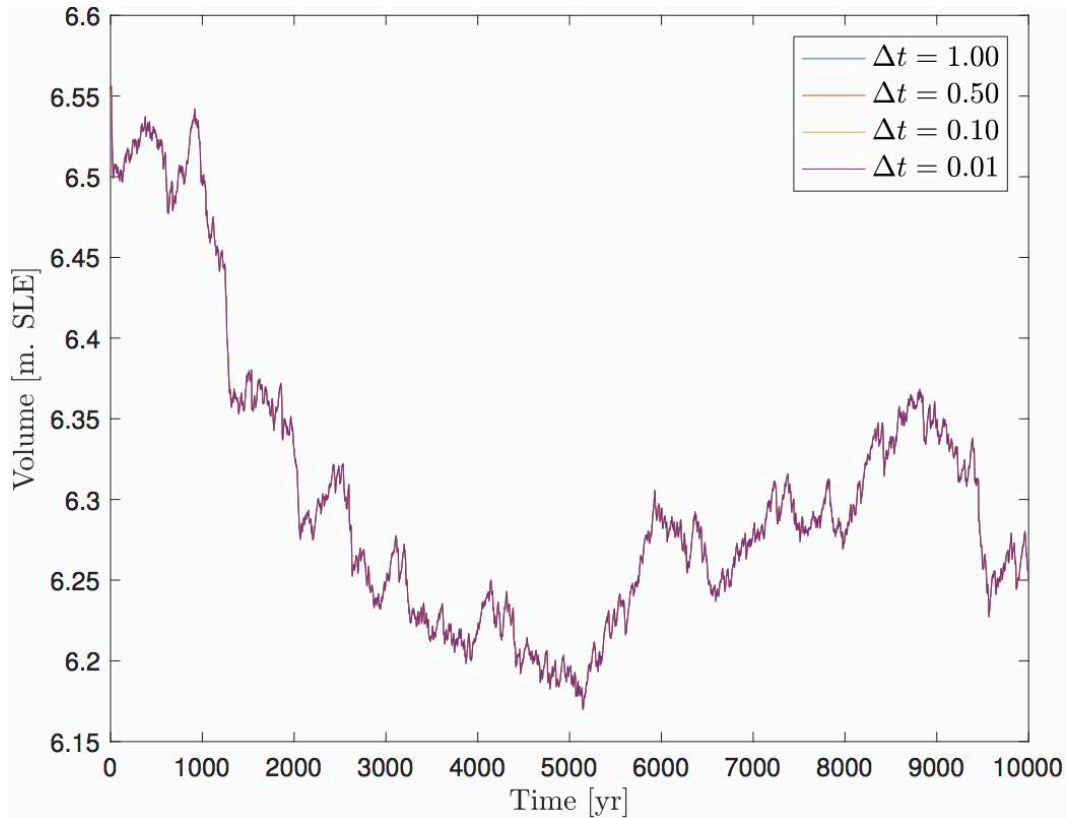
$$V_{sea} = \pi \left( \frac{2}{3} s (R^3 - r_c^3) - d_0 (R^2 - r_c^2) \right) \quad (28)$$

75

76

 $V_{sea}$  is set to zero if the ice does not extend to the sea and thus  $R < r_c$ . The total volume is given by:

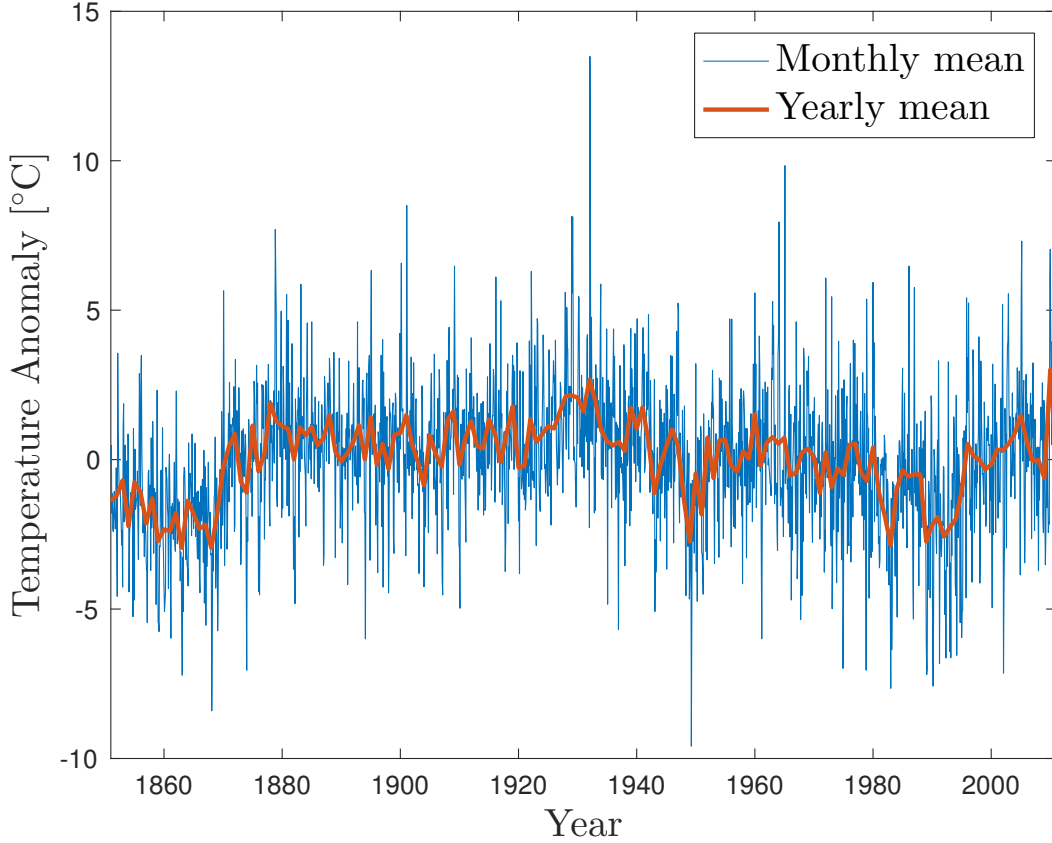
$$V_{tot} = V_{cont} \left( 1 + \frac{\rho_i}{\rho_m - \rho_i} \right) - \frac{\rho_w}{\rho_m - \rho_i} V_{sea}. \quad (29)$$



77 **Figure 2.** Varying the integration stepsize  $\Delta t$  from 1 year to 0.01 years for a simulation with  $\overline{T} = 0$ , such  
78 that the (random) fluctuating temperature  $T_t$  is the same for each whole year. A visual inspection confirms  
79 qualitatively that the graphs for varying  $\Delta t$  coincide and we do not further analyze the consequences of  
80 varying  $\Delta t$ .

81 **Observed Fluctuations in Greenland temperature**

82 Surface temperature anomalies were obtained from (*KNMI*) [2015]. We use the “Twentieth  
83 Century Reanalysis V2c” from the years 1851 to 2011 in a box spanning 68°N to 80°N  
84 and 25°W to 60°W. The raw data consists of monthly means and is shown in Figure 3 as the  
85 blue curve.



86 **Figure 3.** Reanalysis data showing monthly mean surface temperature anomaly (blue curve) over the area  
87 68°N – 80°N, 25°W – 60°W covering a large part of Greenland. The red curve is the annual mean surface  
88 temperature anomaly.

89 We treat the temperature data as follows:

- 90 1. We calculate the yearly mean (the red curve in Figure 3),
- 91 2. To the yearly means we fit an autoregressive model of order 1 or an AR(1)-model,
- 92 3. The parameters from this model is used to generate artificial temperature time series  
93  $\{T_t\}$  that fluctuate in a way similar to the observed temperatures over Greenland.

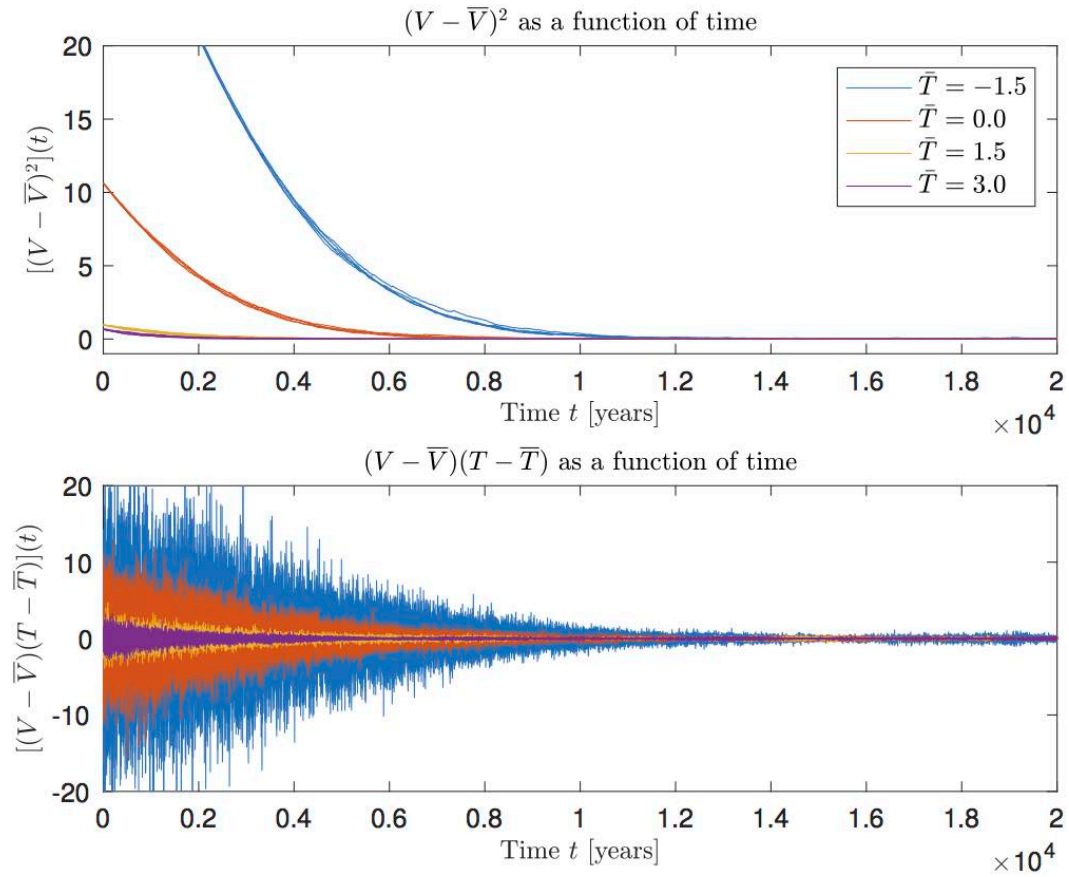
94 An AR(1) model describing describing  $\{T_t\}$  has the form

$$T_{t+1} = c + aT_t + \sigma_{AR}W_t. \quad (30)$$

95 where  $(c, a, \sigma_{AR})$  are parameters to be determined and  $W_t$  is white noise with unit variance  
96 and zero mean. The parameters  $(a, \sigma_{AR})$  are found using MATLAB’s `estimate()`. We find

$$(a, \sigma_{AR}^2) = (0.67, 0.85). \quad (31)$$

97

**Evaluating Neglected Terms in Equation 5)**

98

**Figure 4.** Evaluation of part of the terms dropped from Equation 4 in the main article, for simulations with

99

same parameters as in Figure 1. It is clear that  $\langle (V_t - \bar{V})^2 \rangle$  and  $\langle (T_t - \bar{T})(V_t - \bar{V}) \rangle$  tend to zero.

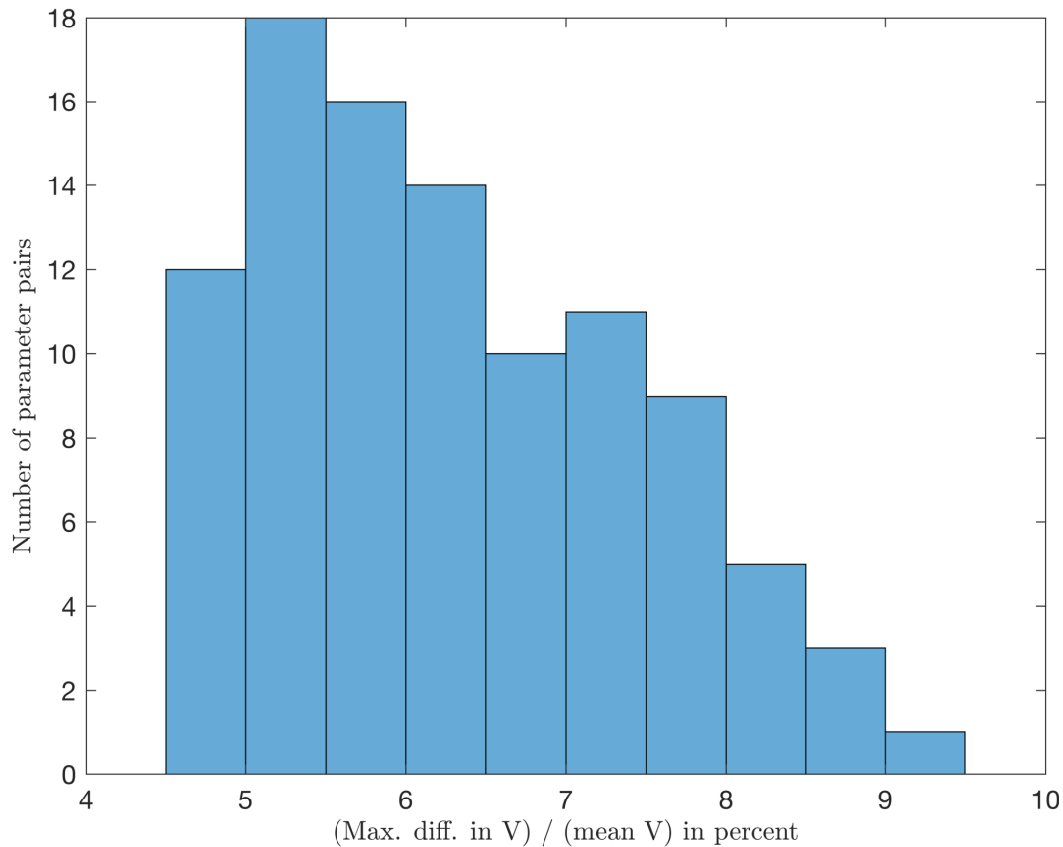
100 **Analysis of *Robinson et al.* [2012]’s Data**

101 We aim to estimate what effect a fluctuating temperature would have on the results  
102 quoted in *Robinson et al.* [2012] concerning the stability of the Greenland Ice Sheet (GrIS).

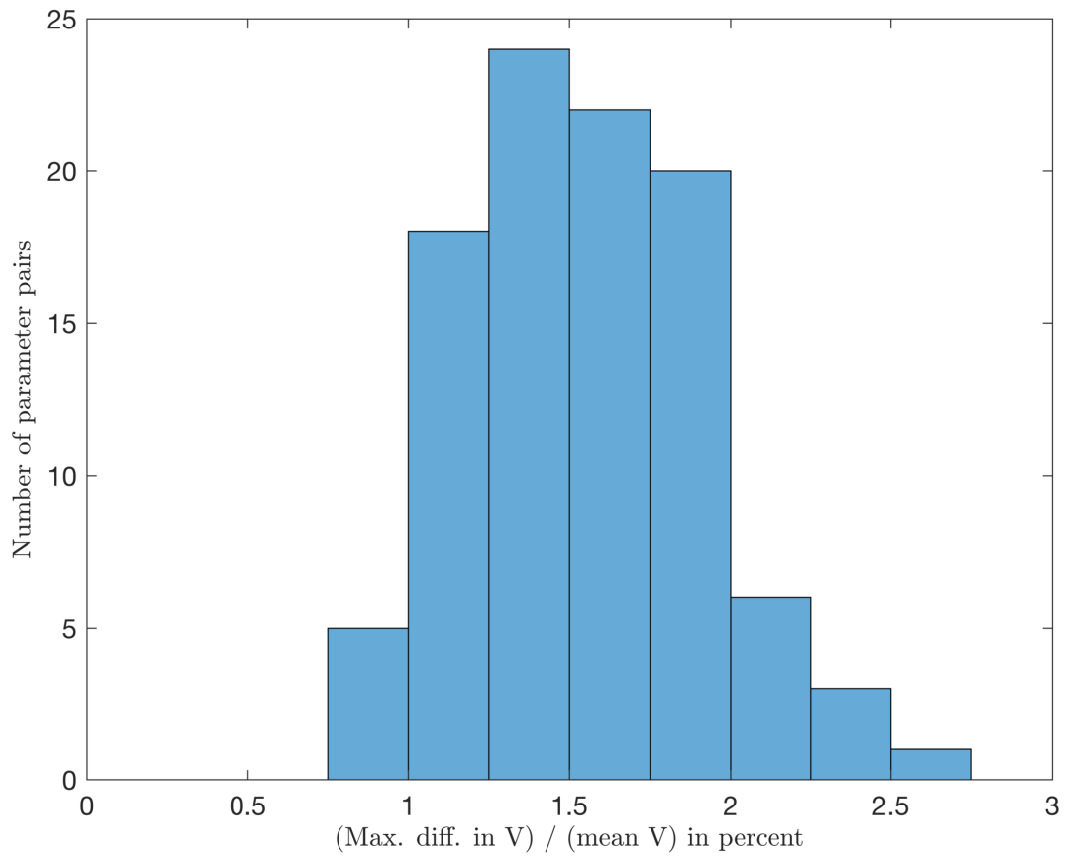
103 **Methodology**

104 The Surface Mass Balance (SMB) as a function of warming ( $\bar{T}$ ) is extracted as follows:

- 105 • In *Robinson et al.* [2012] the warming is ramped for the first 100 years for numerical  
106 reasons. We wait until  $t = 200$  years to extract SMB( $T$ ),
- 107 • *Robinson et al.* [2012] employ  $9 \times 11$  values of two separate parameters deemed “equally  
108 likely” in their simulations,
- 109 • For each of these 99 simulations a 3rd degree polynomial is fitted to SMB( $T$ ) following  
110 *Fettweis et al.* [2012]. We denote these fits  $g_{ij}(T)$ ,
- 111 • We proceed as outlined in Section 4 (main article).
- 112 • Finally we calculate 95% credible intervals for each value of  $T$ . This is done by fitting  
113 a densities to the obtained  $\Delta T$  and  $\Delta \text{SMB}$  and calculating the interval containg 95%  
114 of the observations.



115 **Figure 5.** Histogram of the maximum difference in volume for different temperature anomalies divided  
116 by the mean volume  $t = 200$  years in the data from *Robinson et al.* [2012], calculated for each parameter  
117 combination; in total there are  $9 \times 11$  combinations of two separate parameters .



118

**Figure 6.** Same as Figure 5 but for a maximum warming of 4°C.

# Bibliography

- Alley, R. B., J. Marotzke, W. D. Nordhaus, J. T. Overpeck, D. M. Peteet, R. A. Pielke Jr., R. T. Pierrehumbert, P. B. Rhines, T. F. Stocker, L. D. Talley, and J. M. Wallace (2003). “Abrupt Climate Change”. In: *Science* 229, pp. 2005–2010. DOI: [10.1126/science.1081056](https://doi.org/10.1126/science.1081056).
- Alley, R. B. (2000). “The Younger Dryas cold interval as viewed from central Greenland”. In: *Quaternary Science Reviews* 19.1–5, pp. 213–226. DOI: [10.1016/S0277-3791\(99\)00062-1](https://doi.org/10.1016/S0277-3791(99)00062-1).
- (2004). *GISP2 Ice Core Temperature and Accumulation Data*. IGBP PAGES/World Data Center for Paleoclimatology Data Contribution Series #2004-013. NOAA/NGDC Paleoclimatology Program, Boulder CO, USA. URL: [ftp://ftp.ncdc.noaa.gov/pub/data/paleo/icecore/greenland/summit/gisp2/isotopes/gisp2\\_temp\\_accum\\_alley2000.txt](ftp://ftp.ncdc.noaa.gov/pub/data/paleo/icecore/greenland/summit/gisp2/isotopes/gisp2_temp_accum_alley2000.txt).
- Andersen, K. K., A. Svensson, S. J. Johnsen, S. O. Rasmussen, M. Bigler, R. Rothlisberger, U. Ruth, M.-L. Siggaard-Andersen, J. P. Steffensen, D. Dahl-Jensen, B. M. Vinther, and H. B. Clausen (2006). “The Greenland Ice Core Chronology 2005, 15–42ka. Part 1: constructing the time scale”. In: *Quaternary Science Reviews* 25.23–24, pp. 3246–3257. DOI: [10.1016/j.quascirev.2006.08.002](https://doi.org/10.1016/j.quascirev.2006.08.002).
- Aschwendon, A., E. Bueler, C. Khroulev, and H. Blatter (2012). “An enthalpy formulation for glaciers and ice sheets”. In: *Journal of Glaciology* 58.209, pp. 441–457. DOI: [10.3189/2012JG11J088](https://doi.org/10.3189/2012JG11J088).
- Ashwin, P. and P. Ditlevsen (2015). “The middle Pleistocene transition as a generic bifurcation on a slow manifold”. In: *Climate Dynamics* 45.9, pp. 2683–2695. DOI: [10.1007/s00382-015-2501-9](https://doi.org/10.1007/s00382-015-2501-9).
- Ashwin, P., S. Wieczorek, R. Vitolo, and P. Cox (2012). “Tipping points in open systems: bifurcation, noise-induced and rate-dependent examples in the climate system”. In: *Philosophical Transactions of the Royal Society A: Mathematical, Physical and Engineering Sciences* 370, pp. 1166–1184. DOI: [10.1098/rsta.2011.0306](https://doi.org/10.1098/rsta.2011.0306).
- Asmussen, S. (2003). *Applied Probability and Queues*. Ed. by B. Rozovskii and M. Yor. Second. Springer-Verlag New York. ISBN: 0-387-00211-1.
- Baladi, V. (2000). *Positive Transfer Operators and Decay of Correlations*. World Scientific Publishing Co. Pte. Ltd. ISBN: 981-02-3328-0.
- Barletta, V. R., L. S. Sørensen, and R. Forsberg (2013). “Scatter of mass changes estimates at basin scale for Greenland and Antarctica”. In: *The Cryosphere* 7.5, pp. 1411–1432. DOI: [10.5194/tc-7-1411-2013](https://doi.org/10.5194/tc-7-1411-2013).
- Bartlein, P. J. (2013). “PALEOCLIMATE | Timescales of Climate Change”. In: *Encyclopedia of Quaternary Science*, pp. 93–101. DOI: [10.1016/B978-0-444-53643-3.00006-6](https://doi.org/10.1016/B978-0-444-53643-3.00006-6).
- Berglund, N. and B. Gentz (2006). *Noise-Induced Phenomena in Slow-Fast Dynamical Systems. A Sample-Paths Approach*. Springer-Verlag London. ISBN: 978-1-84628-038-2.
- Bigler, M. (2004). “Hochauflösende Spurenstoffmessungen an polaren Eisbohrkernen: Glaziochemische und klimatische Prozessstudien”. PhD thesis. University of Bern, Switzerland. URL: [http://www.zb.unibe.ch/download/eldiss/04bigler\\_m.pdf](http://www.zb.unibe.ch/download/eldiss/04bigler_m.pdf).
- Blank, M. and G. Keller (1998). “Random perturbations of chaotic dynamical systems: stability of the spectrum”. In: *Nonlinearity* 11.5, pp. 1351–1364. DOI: [10.1088/0951-7715/11/5/010](https://doi.org/10.1088/0951-7715/11/5/010).
- Blank, M., G. Keller, and C. Liverani (2002). “Ruelle–Perron–Frobenius spectrum for Anosov maps”. In: *Nonlinearity* 15.6, pp. 1905–1973. DOI: [10.1088/0951-7715/15/6/309](https://doi.org/10.1088/0951-7715/15/6/309).
- Box, G. E. P., G. M. Jenkins, and G. C. Reinsel (2008). *Time Series Analysis - Forecasting and Control*. Fourth. John Wiley & Sons, Inc.

- Breton, D. J., B. G. Koffman, A. V. Kurbatov, K. J. Kreutz, and G. S. Hamilton (2012). “Quantifying Signal Dispersion in a Hybrid Ice Core Melting System”. In: *Environmental Science & Technology* 46, pp. 11922–11928. DOI: [10.1021/es302041k](https://doi.org/10.1021/es302041k).
- Brook, E. J. (2013). “ICE CORE METHODS | Stable Isotopes”. In: *Encyclopedia of Quaternary Science*, pp. 347–352. DOI: [10.1016/b978-0-444-53643-3.00316-2](https://doi.org/10.1016/b978-0-444-53643-3.00316-2).
- Bueler, E. and J. Brown (2009). “Shallow shelf approximation as a “sliding law” in a thermodynamically-coupled ice sheet model”. In: *Journal of Geophysical Research* 114. DOI: [10.1029/2008JF001179](https://doi.org/10.1029/2008JF001179).
- Butterley, O. (2016). “A Note on Operator Semigroups Associated to Chaotic Flows”. In: *Ergodic Theory and Dynamical Systems* 36.05, pp. 1396–1408. DOI: [10.1017/etds.2014.127](https://doi.org/10.1017/etds.2014.127).
- Butterley, O. and C. Liverani (2007). “Smooth Anosov Flows: Correlation Spectra and Stability”. In: *Journal of Modern Dynamics* 1.2, pp. 301–321. DOI: [10.3934/jmd.2007.1.301](https://doi.org/10.3934/jmd.2007.1.301).
- Centre for Ice and Climate (2010). *GICC05model.txt time scale and  $\delta^{18}O$  values*. <http://www.iceandclimate.nbi.ku.dk/data>. URL: [http://www.iceandclimate.nbi.ku.dk/data/2010-11-19\\_GICC05model.txt\\_for\\_NGRIP.xls](http://www.iceandclimate.nbi.ku.dk/data/2010-11-19_GICC05model.txt_for_NGRIP.xls).
- (2016). *The GICC05 time scale*. <http://www.iceandclimate.nbi.ku.dk>. URL: [http://www.iceandclimate.nbi.ku.dk/research/strat\\_dating/annual\\_layer\\_count/gicc05\\_time\\_scale/](http://www.iceandclimate.nbi.ku.dk/research/strat_dating/annual_layer_count/gicc05_time_scale/).
- Cessi, P. (1994). “A Simple Box Model of Stochastically Forced Thermohaline Flow”. In: *Journal of Physical Oceanography* 24, pp. 1911–1920. DOI: [10.1175/1520-0485\(1994\)024<1911:ASBMOS>2.0.CO;2](https://doi.org/10.1175/1520-0485(1994)024<1911:ASBMOS>2.0.CO;2).
- Chekroun, M. D., E. Simonnet, and M. Ghil (2011). “Stochastic climate dynamics: Random attractors and time-dependent invariant measures”. In: *Physica D* 240, pp. 1685–1700. DOI: [10.1016/j.physd.2011.06.005](https://doi.org/10.1016/j.physd.2011.06.005).
- Chekroun, M. D., J. D. Neelin, D. Kondrashov, J. C. McWilliams, and M. Ghil (2014). “Rough parameter dependence in climate models and the role of Ruelle-Pollicott resonances.” In: *Proceedings of the National Academy of Sciences of the United States of America* 111.5, pp. 1684–90. DOI: [10.1073/pnas.1321816111](https://doi.org/10.1073/pnas.1321816111).
- Cimadoribus, A. A., S. S. Drijfhout, V. Livina, and G. van der Schrier (2013). “Dansgaard-Oeschger events: Bifurcation points in the climate system”. In: *Climate of the Past* 9.1, pp. 323–333. DOI: [10.5194/cp-9-323-2013](https://doi.org/10.5194/cp-9-323-2013).
- Clewley, R. (2012). “Hybrid Models and Biological Model Reduction with PyDSTool”. In: *PLoS Computational Biology* 8.8, e1002628. DOI: [10.1371/journal.pcbi.1002628](https://doi.org/10.1371/journal.pcbi.1002628).
- Clewley, R. H., W. E. Sherwood, M. D. LaMar, and J. M. Guckenheimer (2007). *PyDSTool, a software environment for dynamical systems modeling*. URL: <http://pydstool.sourceforge.net>.
- Crucifix, M. (2012). “Oscillators and relaxation phenomena in Pleistocene climate theory”. In: *Philosophical Transactions of the Royal Society A: Mathematical, Physical and Engineering Sciences* 370.1962, pp. 1140–1165. DOI: [10.1098/rsta.2011.0315](https://doi.org/10.1098/rsta.2011.0315).
- Dahl-Jensen, D., M. Kirk, L. B. Larsen, S. G. Sheldon, and J. P. Steffensen (2016). *Field season 2016 – East Greenland Ice core Project (EGRIP) 2015-2020: Establishing the EGRIP drilling camp*. Ice and Climate Group, NBI for The EGRIP project responsables and participants and Danish and Greenlandic authorities. Copenhagen. URL: <http://www.isaaffik.org/sites/default/files/egrip2016fieldplan.pdf>.
- Dakos, V., S. R. Carpenter, W. A. Brock, A. M. Ellison, V. Guttal, A. R. Ives, S. Kéfi, V. Livina, D. A. Seekell, E. H. van Nes, and M. Scheffer (2012a). “Methods for Detecting Early Warnings of Critical Transitions in Time Series Illustrated Using Simulated Ecological Data”. In: *PLoS One* 7.7, e401010 1–20. DOI: [10.1371/journal.pone.0041010](https://doi.org/10.1371/journal.pone.0041010).
- Dakos, V., E. H. van Nes, P. D’Odorico, and M. Scheffer (2012b). “Robustness of variance and autocorrelation as indicators of critical slowing down”. In: *Ecology* 93.2, pp. 264–271. DOI: [10.1890/11-0889.1](https://doi.org/10.1890/11-0889.1).
- Dakos, V., M. Scheffer, E. H. van Nes, V. Brovkin, V. Petoukhov, and H. Held (2008). “Slowing down as an early warning signal for abrupt climate change”. In: *PNAS* 105.38, pp. 14308–14312. DOI: [10.1073/pnas.0802430105](https://doi.org/10.1073/pnas.0802430105).
- Dansgaard, W. (1964). “Stable isotopes in precipitation”. In: *Tellus* 16.4, pp. 436–468. DOI: [10.1111/j.2153-3490.1964.tb00181.x](https://doi.org/10.1111/j.2153-3490.1964.tb00181.x).
- Dansgaard, W., H. B. Clausen, N. Gundestrup, C. U. Hammer, S. F. Johnsen, P. M. Kristinsdottir, and N. Reeh (1982). “A New Greenland Deep Ice Core”. In: *Science* 218.4579, pp. 1273–1277. DOI: [10.1126/science.218.4579.1273](https://doi.org/10.1126/science.218.4579.1273).
- Dansgaard, W., S. J. Johnsen, H. B. Clausen, D. Dahl-Jensen, N. S. Gundestrup, C. U. Hammer, C. S. Hvidberg, J. P. Steffensen, a. E. Sveinbjörnsdottir, J. Jouzel, and G.

- Bond (1993). “Evidence for general instability of past climate from a 250-kyr \nice-core record”. In: *Nature* 364.6434, pp. 218–220. ISSN: 0028-0836. DOI: [10.1038/364218a0](https://doi.org/10.1038/364218a0).
- Davies, E. B. (2007). *Linear Operators and Their Spectra*. Cambridge University Press. ISBN: 978-0-511-28503-5.
- Dellnitz, M., G. Froyland, C. Horenkamp, K. Padberg-Gehle, and A. S. Gupta (2009). “Seasonal variability of the subpolar gyres in the Southern Ocean: a numerical investigation based on transfer operators”. In: *Nonlinear Processes in Geophysics* 16, pp. 655–664. DOI: [10.5194/npg-16-655-2009](https://doi.org/10.5194/npg-16-655-2009). URL: <http://www.nonlin-processes-geophys.net/16/655/2009/>.
- Dellnitz, M., G. Froyland, and S. Sertl (2000). “On the isolated spectrum of the Perron-Frobenius operator”. In: *Nonlinearity* 13.4, pp. 1171–1188. DOI: [10.1088/0951-7715/13/4/310](https://doi.org/10.1088/0951-7715/13/4/310).
- Dellnitz, M. and O. Junge (1999). “On the Approximation of Complicated Dynamical Behavior”. In: *SIAM J. Numer. Anal.* 36.2, pp. 491–515. DOI: [10.1007/978-0-387-21830-4\\_22](https://doi.org/10.1007/978-0-387-21830-4_22).
- Dijkstra, H. A. (2013). *Nonlinear Climate Dynamics*. Cambridge University Press. ISBN: 978-0-521-87917-0.
- Ditlevsen, P. D., K. K. Andersen, and A. Svensson (2007). “The DO-climate events are probably noise induced: statistical investigation of the claimed 1470 years cycle”. In: *Climate of the Past* 3, pp. 129–134. DOI: [10.5194/cp-3-129-2007](https://doi.org/10.5194/cp-3-129-2007).
- Ditlevsen, P. D. (1999). “Observations of  $\alpha$ -stable noise induced millennial climate changes from an ice-core record”. In: *Geophysical Research Letters* 26.10, pp. 1441–1444. DOI: [10.1029/1999gl1900252](https://doi.org/10.1029/1999gl1900252).
- (2004). *Turbulence and Climate Dynamics*. Copenhagen: Print J & R Frydendahl A/S. ISBN: 87990522-0-2.
- Ditlevsen, P. D. and S. J. Johnsen (2010). “Tipping points: Early warning and wishful thinking”. In: *Geophysical Research Letters* 37.19, pp. 1–4. DOI: [10.1029/2010gl1044486](https://doi.org/10.1029/2010gl1044486).
- Ditlevsen, P. D., M. S. Kristensen, and K. K. Andersen (2005). “The Recurrence Time of Dansgaard–Oeschger Events and Limits on the Possible Periodic Component”. In: *Journal of Climate* 18, pp. 2594–2603. DOI: [10.1175/JCLI3437.1](https://doi.org/10.1175/JCLI3437.1).
- Ditlevsen, S. (2008). *Example: the Ornstein-Uhlenbeck process*. <http://www.math.ku.dk/~susanne/StatDiff/Overheads1b>. Lecture Notes. Retrieved September 24, 2016.
- Dorfman, J. R. (1999). *An Introduction to Chaos in Nonequilibrium Statistical Mechanics*. Cambridge University Press. ISBN: 0-521-65589-7.
- Eckmann, J.-P. and D. Ruelle (1985). “Ergodic theory of chaos and strange attractors”. In: *Review of Modern Physics* 57.3, pp. 617–656. DOI: [10.1103/revmodphys.57.617](https://doi.org/10.1103/revmodphys.57.617).
- Engel, K.-J. and R. Nagel (2000). *One-Parameter Semigroups for Linear Evolution Equations*. Ed. by S. Axler, F. Gehring, and K. Ribet. Springer-Verlag New York Berlin Heidelberg. ISBN: 0-387-98463-1.
- Froyland, G. (1998). “Approximating Physical Invariant Measures of Mixing Dynamical Systems in Higher Dimensions”. In: *Nonlinear Analysis, Theory, Methods & Applications* 32.7, pp. 831–860. DOI: [10.1016/S0362-546X\(97\)00527-0](https://doi.org/10.1016/S0362-546X(97)00527-0).
- (2007). “On Ulam approximation of the isolated spectrum and eigenfunctions of hyperbolic maps”. In: *Discrete and Continuous Dynamical Systems* 17.3, pp. 671–689. DOI: [10.3934/dcds.2007.17.671](https://doi.org/10.3934/dcds.2007.17.671).
- (2008). “Unwrapping eigenfunctions to discover the geometry of almost-invariant sets in hyperbolic maps”. In: *Physica D* 237.6, pp. 840–853. DOI: [10.1016/j.physd.2007.11.004](https://doi.org/10.1016/j.physd.2007.11.004).
- Froyland, G., C. González-Tokman, and A. Quas (2014). “Detecting Isolated Spectrum Of Transfer And Koopman Operators With Fourier Analytic Tools”. In: *Journal of Computational Dynamics* 1.2, pp. 249–278. DOI: [10.3934/jcd.2014.1.249](https://doi.org/10.3934/jcd.2014.1.249).
- Froyland, G., S. Lloyd, and A. Quas (2009). “Coherent structures and isolated spectrum for Perron–Frobenius cocycles”. In: *Ergodic Theory and Dynamical Systems* 30.03, pp. 729–756. URL: [10.1017/s0143385709000339](https://doi.org/10.1017/s0143385709000339).
- Galewsky, J., H. C. Steen-Larsen, R. D. Field, J. Worden, C. Risi, and M. Schneider (2016). “Stable isotopes in atmospheric water vapor and applications to the hydrologic cycle”. In: *Review of Geophysics* 54, pp. 1–57. DOI: [10.1002/2015rg000512](https://doi.org/10.1002/2015rg000512).
- Gallavotti, G. and E. G. D. Cohen (1995). “Dynamical ensembles in stationary states”. In: *Journal of Statistical Physics* 80.5–6, pp. 931–970. DOI: [10.1007/bf02179860](https://doi.org/10.1007/bf02179860).
- Gardiner, C. (2009). *Stochastic Methods. A Handbook for the Natural and Social Sciences*. Fourth. Springer Series in Synergetics. Springer-Verlag Heidelberg. ISBN: 978-3-540-70712-7.

- Gaspard, P., G. Nicolis, A. Provata, and S. Tasaki (1995). “Spectral signature of the pitchfork bifurcation: Liouville equation approach”. In: *Physical Review E* 51.1, pp. 74–94. DOI: [10.1103/physreve.51.74](https://doi.org/10.1103/physreve.51.74).
- Gaspard, P. and S. Tasaki (2001). “Liouvillian Dynamics of the Hopf Bifurcation”. In: *Physical Review E* 64.056232, pp. 1–22. DOI: [10.1103/physreve.64.056232](https://doi.org/10.1103/physreve.64.056232).
- Gfeller, G., H. Fischer, M. Bigler, S. Schüpbach, D. Leuenberger, and O. Mini (2014). “Representativeness and seasonality of major ion records derived from NEEM firn cores”. In: *The Cryosphere* 8, pp. 1855–1870. DOI: [10.5194/tc-8-1855-2014](https://doi.org/10.5194/tc-8-1855-2014).
- Gowers, T., J. B. (associate), and I. L. (associate), eds. (2008). *The Princeton Companion to Mathematics*. Princeton University Press. ISBN: 978-0-691-11880-2.
- Grootes, P. M., M. Stuiver, J. W. C. White, S. Johnsen, and S. Jouzel (1993). “Comparison of oxygen isotope records from the GISP2 and GRIP Greenland ice cores”. In: *Nature* 366.6455, pp. 552–554. DOI: [10.1038/366552a0](https://doi.org/10.1038/366552a0).
- Guckenheimer, J. and P. Holmes (1983). *Nonlinear Oscillations, Dynamical Systems, and Bifurcations of Vector Fields*. Vol. 42. Applied Mathematical Sciences. Corrected seventh printing, 2002. Springer.
- Hagberg, A. A., D. A. Schult, and P. J. Swart (2008). “Exploring network structure, dynamics, and function using NetworkX”. In: *Proceedings of the 7th Python in Science Conference (SciPy2008)*. Pasadena, CA USA, pp. 11–15. URL: <http://math.lanl.gov/~hagberg/Papers/hagberg-2008-exploring.pdf>.
- Hairer, E., S. P. Nørsett, and G. Wanner (2008). *Solving Ordinary Differential Equations I – Nonstiff Problems*. Second Revised Edition, Corrected 3rd Printing 2008. Springer. ISBN: 978-3-540-56670-0. DOI: [10.1007/978-3-540-78862-1](https://doi.org/10.1007/978-3-540-78862-1).
- Hairer, E. and G. Wanner (2010). *Solving Ordinary Differential Equations II – Stiff and Differential-Algebraic Problems*. Second Revised Edition, Corrected printing 2002, First Softcover Printing 2010. Springer. ISBN: 978-3-642-05220-0. DOI: [10.1007/978-3-642-05221-7](https://doi.org/10.1007/978-3-642-05221-7).
- Hasselmann, K. (1976). “Stochastic Climate Models – Part I. Theory”. In: *Tellus XXVII* 6. DOI: [10.3402/tellusa.v28i6.11316](https://doi.org/10.3402/tellusa.v28i6.11316).
- Heath, M. T. (2005). *Scientific Computing: An Introductory Survey*. Second International Edition. McGraw-Hill Companies, Inc. ISBN: 007-124489-1.
- Hegger, R., H. Kantz, and T. Schreiber (1999). “Practical implementation of nonlinear time series methods: The TISEAN package”. In: *Chaos* 9.2, pp. 413–435. DOI: [10.1063/1.166424](https://doi.org/10.1063/1.166424).
- Held, H. and T. Kleinen (2004). “Detection of climate system bifurcations by degenerate fingerprinting”. In: *Geophysical Research Letters* 31.23, pp. 1–4. ISSN: 00948276. DOI: [10.1029/2004gl020972](https://doi.org/10.1029/2004gl020972).
- Higham, D. J. (2001). “An Algorithmic Introduction to Numerical Simulation of Stochastic Differential Equations”. In: *SIAM Review* 43.3, pp. 525–546. DOI: [10.1137/S0036144500378302](https://doi.org/10.1137/S0036144500378302).
- Hoegh-Guldberg, O., P. J. Mumby, A. J. Hooten, R. S. Steneck, P. Greenfield, E. Gomez, C. D. Harvell, P. F. Sale, A. J. Edwards, K. Caldeira, N. Knowlton, C. M. Eakin, R. Iglesias-Prieto, N. Muthiga, R. H. Bradbury, A. Dubi, and M. E. Hatzioiols (2007). “Coral Reefs Under Rapid Climate Change and Ocean Acidification”. In: *Science* 318.5857, pp. 1737–1742. DOI: [10.1126/science.1152509](https://doi.org/10.1126/science.1152509).
- Höll, M. and H. Kantz (2015). “The fluctuation function of the detrended fluctuation analysis - Investigation on the AR ( 1 ) process”. In: *European Physical Journal B* 88.5, pp. 1–15. DOI: [10.1140/epjb/e2015-60143-1](https://doi.org/10.1140/epjb/e2015-60143-1).
- Horsthemke, W. and R. Lefever (2006). *Noise-Induced Transitions. Theory and Applications in Physics, Chemistry, and Biology*. 2nd Printing 2006. Springer-Verlag Berlin Heidelberg New York. ISBN: 978-3-540-11359-1.
- Hoyer, S. and J. Hamman (2016). “xarray: N-D labeled arrays and datasets in Python”. In: *in prep, J. Open Res. Software*. URL: <http://xarray.pydata.org>.
- Hoyer, S., C. Fitzgerald, J. Hamman, et al. (2016). *xarray: v0.8.0*. DOI: [10.5281/zenodo.59499](https://doi.org/10.5281/zenodo.59499).
- Hughen, K. A., J. R. Southon, S. J. Lehman, and J. T. Overpeck (2000). “Synchronous Radiocarbon and Climate Shifts During the Last Deglaciation”. In: *Science* 290, pp. 1951–1954. DOI: [10.1126/science.290.5498.1951](https://doi.org/10.1126/science.290.5498.1951).
- Hunter, J. D. (2007). “Matplotlib: A 2D Graphics Environment”. In: *Computing in Science & Engineering* 9.3, pp. 90–95. DOI: [10.1109/MCSE.2007.55](https://doi.org/10.1109/MCSE.2007.55).
- Hutterli, M. A., T. Crueger, H. Fischer, K. K. Andersen, C. C. Raible, T. F. Stocker, M. L. Siggaard-Andersen, J. R. McConnell, R. C. Bales, and J. F. Burkhart (2007). “The influ-

- ence of regional circulation patterns on wet and dry mineral dust and sea salt deposition over Greenland”. In: *Climate Dynamics* 28, pp. 635–647. DOI: [10.1007/s00382-006-0211-z](https://doi.org/10.1007/s00382-006-0211-z).
- IPCC (2013). “Annex III: Glossary”. In: *Climate Change 2013: The Physical Science Basis. Contribution of Working Group I to the Fifth Assessment Report of the Intergovernmental Panel on Climate Change*. Ed. by T. Stocker, D. Qin, G.-K. Plattner, M. Tignor, S. Allen, J. Boschung, A. Nauels, Y. Xia, V. Bex, and P. Midgley. Cambridge, United Kingdom and New York, NY, USA: Cambridge University Press. Chap. AIII, pp. 1447–1466. ISBN: ISBN 978-1-107-66182-0. DOI: [10.1017/CB09781107415324.031](https://doi.org/10.1017/CB09781107415324.031). URL: <http://www.climatechange2013.org>.
- Johnsen, S. J., H. B. Clausen, W. Dansgaard, K. Fuhrer, N. Gundestrup, C. U. Hammer, P. Iversen, J. Jouzel, B. Stauffer, and J. P. Steffensen (1992). “Irregular glacial interstadials recorded in a new Greenland ice core”. In: *Nature* 359.6393, pp. 311–313. DOI: [10.1038/359311a0](https://doi.org/10.1038/359311a0).
- Johnsen, S. J., W. Dansgaard, and J. W. C. White (1989). “The origin of Arctic precipitation under present and glacial conditions”. In: *Tellus B* 41.4, pp. 452–468. DOI: [10.3402/tellusb.v41i4.15100](https://doi.org/10.3402/tellusb.v41i4.15100).
- Jones, E., T. Oliphant, P. Peterson, et al. (2001). *SciPy: Open source scientific tools for Python*. URL: <http://www.scipy.org/> (visited on 10/10/2016).
- Kantelhardt, J. W., E. Koscielny-Bunde, H. H. Rego, S. Havlin, and A. Bunde (2001). “Detecting long-range correlations with detrended fluctuation analysis”. In: *Physica A: Statistical Mechanics and its Applications* 295.3–4, pp. 441–454. DOI: [10.1016/s0378-4371\(01\)00144-3](https://doi.org/10.1016/s0378-4371(01)00144-3).
- Kantz, H. and T. Schreiber (2000). *Nonlinear Time Series Analysis*. Second Edition published 2004. Cambridge University Press.
- Keller, G. (1984). “On the rate of convergence to equilibrium in one-dimensional systems”. In: *Mathematical Physics* 96.2, pp. 181–193. DOI: [10.1007/bf01240219](https://doi.org/10.1007/bf01240219).
- Kloeden, P. E. and E. Platen (1995). *Numerical Solution of Stochastic Differential Equations*. Ed. by I. Karatzas and M. Yor. Second Corrected Printing. Springer-Verlag Berlin Heidelberg. ISBN: 3-540-54062-8.
- Kluyver, T., B. Ragan-Kelley, F. Pérez, B. Granger, M. Bussonnier, J. Frederic, K. Kelley, J. Hamrick, J. Grout, S. Corlay, P. Ivanov, D. Avila, S. Abdalla, C. Willing, and Jupyter Development Team (2012). “Jupyter Notebooks – a publishing format for reproducible computational workflows”. In: *Positioning and Power in Academic Publishing: Players, Agents and Agendas*. IOS Press, pp. 87–90. URL: [10.3233/978-1-61499-649-1-87](https://doi.org/10.3233/978-1-61499-649-1-87).
- Kreutz, K. and B. Koffman (2013). “ICE CORE METHODS | Glaciochemistry”. In: *Encyclopedia of Quaternary Science*, pp. 326–333. DOI: [10.1016/b978-0-444-53643-3.00312-5](https://doi.org/10.1016/b978-0-444-53643-3.00312-5).
- Kuehn, C. (2011). “A Mathematical Framework for Critical Transitions: Bifurcations, Fast-Slow Systems and Stochastic Dynamics”. In: *Physica D* 240.12, pp. 1020–1035. DOI: [10.1016/j.physd.2011.02.012](https://doi.org/10.1016/j.physd.2011.02.012).
- (2012). “A Mathematical Framework for Critical Transitions: Normal Forms, Variance and Applications”. In: *Journal of Nonlinear Science* 23.3, pp. 457–510. DOI: [10.1007/s00332-012-9158-x](https://doi.org/10.1007/s00332-012-9158-x).
- Kuznetsov, Y. A. (1998). *Elements of Applied Bifurcation Theory*. Ed. by I. Karatzas and M. Yor. Second. Vol. 112. Applied Mathematical Sciences. Springer-Verlag New York. ISBN: 0-387-98382-1.
- (2006). “Andronov-Hopf Bifurcation”. In: *Scholarpedia* 1.10. revision #90964, p. 1858. DOI: [doi:10.4249/scholarpedia.1858](https://doi.org/10.4249/scholarpedia.1858). URL: [http://www.scholarpedia.org/article/Andronov-Hopf\\_bifurcation](http://www.scholarpedia.org/article/Andronov-Hopf_bifurcation).
- Kwasniok, F. and G. Lohmann (2012). “A stochastic nonlinear oscillator model for glacial millennial-scale climate transitions derived from ice-core data”. In: *Nonlinear Processes in Geophysics* 19, pp. 595–603. DOI: [10.5194/npg-19-595-2012](https://doi.org/10.5194/npg-19-595-2012).
- Kwasniok, F. and G. Lohmann (2009). “Deriving dynamical models from paleoclimatic records: application to glacial millennial-scale climate variability”. In: *Physical Review E* 80, pp. 066104-1–066104-9. DOI: [10.1103/PhysRevE.80.066104](https://doi.org/10.1103/PhysRevE.80.066104).
- Lackenbauer, P. W., M. J. Farish, and J. Arthur-Lackenbauer (2005). *The Distant Early Warning (DEW) Line: A Bibliography and Documentary Resource List*. The Arctic Institute of North America. ISBN: 1-894788-01-X. URL: <http://pubs.aina.ucalgary.ca/aina/DEWLineBib.pdf>.
- Lasota, A. and M. C. Mackey (1994). *Chaos, Fractals, and Noise. Stochastic Aspects of Dynamics*. Ed. by J. Marsden and L. Sirovich. Second. Springer Science+Business Media New York. ISBN: 0387940499.

- Legrand, M. and P. Mayewski (1997). “Glaciochemistry of Polar Ice Cores: A Review”. In: *Review of Geophysics* 35.3, pp. 219–243. DOI: [10.1029/96rg03527](https://doi.org/10.1029/96rg03527).
- Lenton, T. M., V. N. Livina, V. Dakos, and M. Scheffer (2012a). “Climate bifurcation during the last deglaciation?”. In: *Climate of the Past* 8.4, pp. 1127–1139. DOI: [10.5194/cp-8-1127-2012](https://doi.org/10.5194/cp-8-1127-2012).
- Lenton, T. M., V. N. Livina, V. Dakos, E. H. van Nes, and M. Scheffer (2012b). “Early warning of climate tipping points from critical slowing down: comparing methods to improve robustness”. In: *Philosophical Transactions of the Royal Society A: Mathematical, Physical and Engineering Sciences* 370, pp. 1185–1204. DOI: [10.1098/rsta.2011.0304](https://doi.org/10.1098/rsta.2011.0304).
- Lenton, T. M. (2011). “Early warning of climate tipping points”. In: *Nature Climate Change* 1.4, pp. 201–209. DOI: [10.1038/nclimate1143](https://doi.org/10.1038/nclimate1143).
- Lenton, T. M., H. Held, E. Kriegler, J. W. Hall, W. Lucht, S. Rahmstorf, and H. J. Schellnhuber (2008). “Tipping elements in the Earth’s climate system”. In: *PNAS* 105.6, pp. 1786–1793. DOI: [10.1073/pnas.0705414105](https://doi.org/10.1073/pnas.0705414105).
- Leon, S. J. (2006). *Linear Algebra With Applications*. Seventh Edition, Pearson International Edition. Pearson Prentice Hall. ISBN: 0-13-200306-6.
- Levin, D. A., Y. Peres, and E. L. Wilmer (2008). *Markov Chains and Mixing Times*. Electronic PDF version. With a chapter on “Coupling from the Past”, by James G. Propp and David B. Wilson. American Mathematical Society. URL: <http://darkwing.uoregon.edu/~dlevin/MARKOV/>.
- Livina, V. N., P. D. Ditlevsen, and T. M. Lenton (2012). “An independent test of methods of detecting system states and bifurcations in time-series data”. In: *Physica A* 391, pp. 485–496. DOI: [10.1016/j.physa.2011.08.025](https://doi.org/10.1016/j.physa.2011.08.025).
- Livina, V. N., F. Kwasiok, and T. M. Lenton (2010). “Potential analysis reveals changing number of climate states during the last 60 kyr”. In: *Climate of the Past* 6, pp. 77–82. DOI: [10.5194/cp-6-77-2010](https://doi.org/10.5194/cp-6-77-2010).
- Livina, V. N., F. Kwasiok, G. Lohmann, J. W. Kantelhardt, and T. M. Lenton (2011). “Changing climate states and stability: from Pliocene to present”. In: *Climate Dynamics* 37, pp. 2437–2453. DOI: [10.1007/s00382-010-0980-2](https://doi.org/10.1007/s00382-010-0980-2).
- Livina, V. N. and T. M. Lenton (2007). “A modified method for detecting incipient bifurcations in a dynamical system”. In: *Geophysical Research Letters* 34.3, pp. 1–5. DOI: [10.1029/2006GL028672](https://doi.org/10.1029/2006GL028672).
- Lorenz, E. N. (1963). “Deterministic Nonperiodic Flow”. In: *Journal of the Atmospheric Sciences* 20.2, pp. 130–141. ISSN: 0309-1333. DOI: [10.1175/1520-0469\(1963\)020<0130:dnf>2.0.co;2](https://doi.org/10.1175/1520-0469(1963)020<0130:dnf>2.0.co;2).
- Lowe, J. J., M. C. Walker, and S. C. Porter (2013). “INTRODUCTION | Understanding Quaternary Climatic Change”. In: *Encyclopedia of Quaternary Science*, pp. 26–35. DOI: [10.1016/b978-0-444-53643-3.00004-2](https://doi.org/10.1016/b978-0-444-53643-3.00004-2).
- Luke, C. M. and P. M. Cox (2011). “Soil carbon and climate change: from the Jenkinson effect to the compost-bomb instability”. In: *European Journal of Soil Science* 62, pp. 5–12. DOI: [10.1111/j.1365-2389.2010.01312.x](https://doi.org/10.1111/j.1365-2389.2010.01312.x).
- Madsen, H. (2008). *Time Series Analysis*. Chapman & Hall/CRC. ISBN: 978-1-4200-5967-0.
- McKinney, W. (2010). “Data Structures for Statistical Computing in Python”. In: *Proceedings of the 9th Python in Science Conference*. Editors: Stéfan van der Walt and Jarrod Millman, pp. 51–56.
- Mezic, I. (2013). “Analysis of Fluid Flows via Spectral Properties of the Koopman Operator”. In: *Annual Review of Fluid Mechanics* 45.1, pp. 357–378. DOI: [10.1146/annurev-fluid-011212-140652](https://doi.org/10.1146/annurev-fluid-011212-140652).
- (2015). *General background on dynamical systems*. <http://homepages.laas.fr/henrion/ecc15/mezic-workshop-ecc15.pdf>. Lecture notes.
- Mikkelsen, T. B. (2012). “Dive Into Chaos”. Course Paper.
- (2013). “Duffing’s Equation - Resonance, Fractal Structure and Period Doubling”. Master’s Thesis. MA thesis. University of Copenhagen.
- Mikkelsen, T. B., A. Grinsted, and P. D. Ditlevsen (2017). “Influence of temperature fluctuations on equilibrium ice sheet volume”. In: *Geophysical Research Letters*. Submitted; under revision by the authors.
- Mitsui, T. and M. Crucifix (2016). “Influence of external forcings on abrupt millennial-scale climate changes: a statistical modelling study”. In: *ArXiv e-prints*. DOI: [10.1007/s00382-016-3235-z](https://doi.org/10.1007/s00382-016-3235-z). arXiv: [1510.06290v2](https://arxiv.org/abs/1510.06290v2) [physics.ao-ph].
- Mudelsee, M. (2010). *Climate Time Series Analysis - Classical Statistical and Bootstrap Methods*. Springer.

- Muresan, I. S., S. A. Khan, A. Aschwanden, C. Khroulev, T. V. Dam, J. Bamber, M. R. van den Broeke, B. Wouters, P. K. Munneke, and K. H. Kjær (2016). “Modelled glacier dynamics over the last quarter of a century at Jakobshavn Isbræ”. In: *The Cryosphere* 10, pp. 597–611. DOI: [10.5194/tc-10-597-2016](https://doi.org/10.5194/tc-10-597-2016).
- Nes, E. H. v. and M. Scheffer (2007). “Slow Recovery from Perturbations as a Generic Indicator of a Nearby Catastrophic Shift.” In: *The American Naturalist* 169.6, pp. 738–747. DOI: [10.1086/516845](https://doi.org/10.1086/516845).
- Nicolis, G. (1995). *Introduction To Nonlinear Science*. Cambridge University Press. ISBN: 0-521-46228-2.
- Nikolaou, A., P. A. Gutiérrez, A. Durán, I. Dicaire, F. Fernández-Navarro, and C. Hervás-Martnez (2014). “Detection of early warning signals in paleoclimate data using a genetic time series segmentation algorithm”. In: *Climate Dynamics* 44.7–8, pp. 1919–1933. DOI: [10.1007/s00382-014-2405-0](https://doi.org/10.1007/s00382-014-2405-0).
- North Greenland Ice Core Project members (2004). “High-resolution record of Northern Hemisphere climate extending into the last interglacial period”. In: *Nature* 431, pp. 147–151. DOI: [10.1038/nature02805](https://doi.org/10.1038/nature02805). Author list: [North Greenland Ice Core Project members](https://www.northgreenlandicecoreproject.org/).
- Oerlemans, J. (2003). “A quasi-analytical ice-sheet model for climate studies”. In: *Nonlinear Processes in Geophysics* 10.4/5, pp. 441–452. DOI: [10.5194/npq-10-441-2003](https://doi.org/10.5194/npq-10-441-2003).
- Øksendal, B. (2013). *Stochastic Differential Equations*. Sixth Corrected Printing of the Sixth Edition. Springer. ISBN: 978-3-540-04758-2. DOI: [10.1007/978-3-642-14394-6](https://doi.org/10.1007/978-3-642-14394-6).
- Ostruszka, A. and K. Zyczkowski (2001). “Spectrum of the Frobenius–Perron operator for systems with stochastic perturbation”. In: *Physics Letters A* 289.6, pp. 306–312. DOI: [10.1016/s0375-9601\(01\)00628-4](https://doi.org/10.1016/s0375-9601(01)00628-4).
- Pedregosa, F., G. Varoquaux, A. Gramfort, V. Michel, B. Thirion, O. Grisel, M. Blondel, P. Prettenhofer, R. Weiss, V. Dubourg, J. Vanderplas, A. Passos, D. Cournapeau, M. Brucher, M. Perrot, and É. Duchesnay (2011). “Scikit-learn: Machine Learning in Python”. In: *Journal of Machine Learning Research* 12, pp. 2825–2830. URL: <http://scikit-learn.org/>.
- Peng, C.-K., S. V. Buldyrev, S. Havlin, M. Simons, H. E. Stanley, and A. L. Goldberger (1994). “Mosaic organization of DNA nucleotides”. In: *Physical Review E* 49.2, pp. 1685–1689. DOI: [10.1103/physreve.49.1685](https://doi.org/10.1103/physreve.49.1685).
- Pérez, F. and B. E. Granger (2007). “IPython: A System for Interactive Scientific Computing”. In: *Computing in Science & Engineering* 9.3, pp. 21–29. DOI: [10.1109/MCSE.2007.53](https://doi.org/10.1109/MCSE.2007.53).
- Perko, L. (2001). *Differential Equations and Dynamical Systems*. Ed. by J. Marsden, L. Sirovich, and M. Golubitsky. Third Edition. Springer-Verlag New York Berlin Heidelberg. ISBN: 0-387-95116-4.
- Pollicott, M. (1985). “On the rate of mixing of Axiom A flows”. In: *Inventiones Mathematicae* 81.3, pp. 413–426. DOI: [10.1007/bf01388579](https://doi.org/10.1007/bf01388579).
- Rahmstorf, S. (2013). “GLACIAL CLIMATES | Thermohaline Circulation”. In: *Encyclopedia of Quaternary Science*, pp. 737–747. DOI: [10.1016/b978-0-444-53643-3.00020-0](https://doi.org/10.1016/b978-0-444-53643-3.00020-0).
- Rasmussen, S. O., P. M. Abbott, T. Blunier, A. J. Bourne, E. Brook, S. L. Buchardt, C. Buizert, J. Chappellaz, H. B. Clausen, E. Cook, D. Dahl-Jensen, S. M. Davies, M. Guillevic, S. Kipfstuhl, T. Laepple, I. K. Seierstad, J. P. Severinghaus, J. P. Steffensen, C. Stowasser, A. Svensson, P. Vallelonga, B. M. Vinther, F. Wilhelms, and M. Winstrup (2013). “A first chronology for the North Greenland Eemian Ice Drilling (NEEM) ice core”. In: *Climate of the Past* 9.6, pp. 2713–2730. DOI: [10.5194/cp-9-2713-2013](https://doi.org/10.5194/cp-9-2713-2013).
- Rasmussen, S. O., K. K. Andersen, a. M. Svensson, J. P. Steffensen, B. M. Vinther, H. B. Clausen, M. L. Siggaard-Andersen, S. J. Johnsen, L. B. Larsen, D. Dahl-Jensen, M. Bigler, R. Röthlisberger, H. Fischer, K. Goto-Azuma, M. E. Hansson, and U. Ruth (2006). “A new Greenland ice core chronology for the last glacial termination”. In: *Journal of Geophysical Research: Atmospheres* 111.D6, pp. 1–16. DOI: [10.1029/2005jd006079](https://doi.org/10.1029/2005jd006079).
- Rasmussen, S. O., M. Bigler, S. P. Blockley, T. Blunier, S. L. Buchardt, H. B. Clausen, I. Cvijanovic, D. Dahl-Jensen, S. J. Johnsen, H. Fischer, V. Gkinis, M. Guillevic, W. Z. Hoek, J. J. Lowe, J. B. Pedro, T. Popp, I. K. Seierstad, J. P. Steffensen, A. M. Svensson, P. Vallelonga, B. M. Vinther, M. J. Walker, J. J. Wheatley, and M. Winstrup (2014). “A stratigraphic framework for abrupt climatic changes during the Last Glacial period based on three synchronized Greenland ice-core records: refining and extending the INTIMATE event stratigraphy”. In: *Quaternary Science Reviews* 106, pp. 14–28. DOI: [10.1016/j.quascirev.2014.09.007](https://doi.org/10.1016/j.quascirev.2014.09.007).
- Ritchie, P. and J. Sieber (2016). “Early-warning indicators for rate-induced tipping”. In: arXiv: [1509.01696v5](https://arxiv.org/abs/1509.01696v5) [math.DS].

- Robinson, A., R. Calov, and A. Ganopolski (2012). “Multistability and critical thresholds of the Greenland ice sheet”. In: *Nature Climate Change* 2.6, pp. 429–432. DOI: [10.1038/nclimate1449](https://doi.org/10.1038/nclimate1449).
- Röthlisberger, R., M. Bigler, M. Hutterli, S. Sommer, B. Stauffer, H. G. Junghans, and D. Wagenbach (2000). “Technique for Continuous High-Resolution Analysis of Trace Substances in Firn and Ice Cores”. In: *Environmental Science & Technology* 34, pp. 338–342. DOI: [10.1021/es9907055](https://doi.org/10.1021/es9907055).
- Ruddiman, W. F. (2013). *Earth’s Climate - Past and Future*. 3rd Edition (October 1, 2013). W.H. Freeman.
- Ruelle, D. (1986a). “Locating Resonances for Axiom A Dynamical Systems”. In: *Journal of Statistical Physics* 44.3–4, pp. 281–292. DOI: [10.1007/bf01011300](https://doi.org/10.1007/bf01011300).
- (1986b). “Resonances of Chaotic Dynamical Systems”. In: *Physical Review Letters* 56.5, pp. 405–407. DOI: [10.1103/physrevlett.56.405](https://doi.org/10.1103/physrevlett.56.405).
- Ruth, U., D. Wagenbach, J. P. Steffensen, and M. Bigler (2003). “Continuous record of microparticle concentration and size distribution in the central Greenland NGRIP ice core during the last glacial period”. In: *Journal of Geophysical Research* 108.D3, p. 4098. DOI: [10.1029/2002JD002376](https://doi.org/10.1029/2002JD002376).
- Rypdal, M. (2016). “Early-Warning Signals for the Onsets of Greenland Interstadials and the Younger”. In: *Journal of Climate* 29.22, pp. 4047–4056. DOI: [10.1175/jcli-d-15-0828.1](https://doi.org/10.1175/jcli-d-15-0828.1).
- Scheffer, M. (2009). *Critical Transitions in Nature and Society*. Princeton Studies in Complexity. Princeton University Press. ISBN: 978-0-691-12204-5.
- Scheffer, M., J. Bascompte, W. A. Brock, V. Brovkin, S. R. Carpenter, V. Dakos, H. Held, E. H. van Nes, M. Rietkerk, and G. Sugihara (2009). “Early-warning signals for critical transitions”. In: *Nature* 461.7260, pp. 53–59. DOI: [10.1038/nature08227](https://doi.org/10.1038/nature08227).
- Scheffer, M., S. R. Carpenter, T. M. Lenton, J. Bascompte, W. Brock, V. Dakos, J. van de Koppel, I. A. van de Leemput, S. A. Levin, E. H. van Nes, M. Pascual, and J. Vandermeer (2012). “Anticipating Critical Transitions”. In: *Science* 338.6105, pp. 344–348. DOI: [10.1126/science.1225244](https://doi.org/10.1126/science.1225244).
- Seabold, S. and J. Perktolf (2010). “Statsmodels: Econometric and Statistical Modeling with Python”. In: *Proceedings of the 9th Python in Science Conference (SciPy 2010)*, pp. 57–61. DOI: <https://conference.scipy.org/proceedings/scipy2010/>.
- Steffensen, J. P., K. K. Andersen, M. Bigler, H. B. Clausen, D. Dahl-Jensen, H. Fischer, K. Goto-Azuma, M. Hansson, S. J. Johnsen, J. Jouzel, V. Masson-Delmotte, T. Popp, S. O. Rasmussen, R. Röthlisberger, U. Ruth, B. Stauffer, M.-L. Siggaard-Andersen, A. E. Sveinbjornsdottir, A. Svensson, and J. W. C. White (2008). “High-Resolution Greenland Ice Core Data Show Abrupt Climate Change Happens in Few Years”. In: *Science* 321.5889, pp. 680–684. DOI: [10.1126/science.1157707](https://doi.org/10.1126/science.1157707).
- Stocker, T. F. and S. J. Johnsen (2003). “A minimum thermodynamic model for the bipolar seesaw”. In: *Paleoceanography* 18.4, pp. 11-1–11-9. DOI: [10.1029/2003PA000920](https://doi.org/10.1029/2003PA000920).
- Stommel, H. (1961). “Thermohaline convection with two stable regimes of flow”. In: *Tellus* 13, pp. 224–230. DOI: [10.3402/tellusa.v13i2.9491](https://doi.org/10.3402/tellusa.v13i2.9491).
- Strogatz, S. H. (1994). *Nonlinear Dynamics and Chaos*. With Applications to Physics, Biology, Chemistry and Engineering. Studies in Nonlinearity. First paperback printing, 2000. Perseus Books Publishing, LLC.
- Susuki, Y. and I. Mezic (2015). “A prony approximation of Koopman Mode Decomposition”. In: *2015 54th IEEE Conference on Decision and Control (CDC)*. DOI: [10.1109/cdc.2015.7403326](https://doi.org/10.1109/cdc.2015.7403326).
- Svensson, A., K. K. Andersen, M. Bigler, H. B. Clausen, D. Dahl-Jensen, S. M. Davies, S. J. Johnsen, R. Muscheler, F. Parrenin, S. O. Rasmussen, R. Röthlisberger, I. Seierstad, J. P. Steffensen, and B. M. Vinther (2008). “A 60 000 year Greenland stratigraphic ice core chronology”. In: *Climate of the Past* 4.1, pp. 47–57. DOI: [10.5194/cp-4-47-2008](https://doi.org/10.5194/cp-4-47-2008).
- SymPy Development Team (2016). *SymPy: Python library for symbolic mathematics*. URL: <http://www.sympy.org>.
- Tantet, A., F. R. van der Burgt, and H. a. Dijkstra (2015a). “An early warning indicator for atmospheric blocking events using transfer operators”. In: *Chaos: An Interdisciplinary Journal of Nonlinear Science* 25.3, p. 036406. ISSN: 1054-1500. DOI: [10.1063/1.4908174](https://doi.org/10.1063/1.4908174).
- Tantet, A., V. Lucarini, F. Lunkeit, and H. Dijkstra (2015b). “Crisis of the Chaotic Attractor of a Climate Model: A Transfer Operator Approach”. In: *ArXiv e-prints*. arXiv: [1507.02228v1 \[nlin.CD\]](https://arxiv.org/abs/1507.02228v1).
- Taylor, J. R. (1982). *An Introduction to Error Analysis - The Study of Uncertainties in Physical Measurements*. Second Edition. University Science Books. ISBN: 978-0-935702-75-0.

- Team, P. (2017). *PISM. Parallel Ice Sheet Model*. Development of PISM is supported by NASA grants NNX13AM16G and NNX13AK27G. URL: <http://pism-docs.org/>.
- Thomas, Z. A. (2016). “Using natural archives to detect climate and environmental tipping points in the Earth System”. In: *Quaternary Science Reviews* 152, pp. 60–71. DOI: [10.1016/j.quascirev.2016.09.026](https://doi.org/10.1016/j.quascirev.2016.09.026).
- Thompson, J. M. T. and J. Sieber (2010). “Climate tipping as a noisy bifurcation: a predictive technique”. In: *IMA Journal of Applied Mathematics* 76, pp. 27–46. DOI: [10.1093/imamat/hxq060](https://doi.org/10.1093/imamat/hxq060).
- Thompson, J. M. T. and J. Sieber (2011). “Predicting Climate Tipping As a Noisy Bifurcation: a Review”. In: *International Journal of Bifurcation and Chaos* 21.2. DOI: [10.1142/s0218127411028519](https://doi.org/10.1142/s0218127411028519).
- Ulam, S. (1964). *Problems in Modern Mathematics*. First Science Editions Printing. John Wiley & Sons, Inc.
- van der Pol, B. (1927). “VII. Forced oscillations in a circuit with non-linear resistance. (Reception with reactive triode)”. In: *The London, Edinburgh, and Dublin Philosophical Magazine and Journal of Science* 3.13, pp. 65–80. DOI: [10.1080/14786440108564176](https://doi.org/10.1080/14786440108564176).
- Vinther, B. M., H. B. Clausen, S. J. Johnsen, S. O. Rasmussen, K. K. Andersen, S. L. Buchardt, D. Dahl-Jensen, I. K. Seierstad, M. L. Siggaard-Andersen, J. P. Steffensen, a. Svensson, J. Olsen, and J. Heinemeier (2006). “A synchronized dating of three Greenland ice cores throughout the Holocene”. In: *Journal of Geophysical Research: Atmospheres* 111.D13, pp. 1–11. DOI: [10.1029/2005jd006921](https://doi.org/10.1029/2005jd006921).
- Vinther, B. M. and S. J. Johnsen (2013). “ICE CORE RECORDS | Greenland Stable Isotopes”. In: *Encyclopedia of Quaternary Science* 403–409. DOI: [10.1016/b978-0-444-53643-3.00323-x](https://doi.org/10.1016/b978-0-444-53643-3.00323-x).
- von Storch, H. and F. W. Zwiers (2003). *Statistical Analysis in Climate Research*. netLibrary Edition. Cambridge University Press. ISBN: 0 511 01018 4.
- WAIS Divide Project Members (2015). “Precise inter-polar phasing of abrupt climate change during the last ice age”. In: *Nature* 520, pp. 661–665. DOI: [10.1038/nature14401](https://doi.org/10.1038/nature14401). Author list: [Wais Divide Project Members](#).
- Walt, S. van der, S. C. Colbert, and G. Varoquaux (2011). “The NumPy Array: A Structure for Efficient Numerical Computation”. In: *Computing in Science & Engineering* 13.2, pp. 22–30. DOI: [10.1109/MCSE.2011.37](https://doi.org/10.1109/MCSE.2011.37).
- Waskom, M., O. Botvinnik, P. Hobson, J. B. Cole, Y. Halchenko, S. Hoyer, A. Miles, T. Augspurger, T. Yarkoni, T. Megies, L. P. Coelho, D. Wehner, cynddl, E. Ziegler, diego0020, Y. V. Zaytsev, T. Hoppe, S. Seabold, P. Cloud, M. Koskinen, K. Meyer, A. Qalieh, and D. Allan (2014). *seaborn: v0.5.0 (November 2014)*. DOI: [10.5281/zenodo.12710](https://doi.org/10.5281/zenodo.12710). URL: <https://github.com/mwaskom/seaborn/tree/v0.5.0>.
- Weber, H. J. and G. B. Arfken (2003). *Essential Mathematical Methods for Physicists*. Academic Press. An imprint of Elsevier Science. ISBN: 0-12-059877-9.
- Weisstein, E. W. (2017). *Expectation Value*. From [MathWorld](#) – A Wolfram Web Resource. URL: <http://mathworld.wolfram.com/ExpectationValue.html>.
- Wieczorek, S., P. Ashwin, C. M. Luke, and P. M. Cox (2011). “Excitability in ramped systems: the compost-bomb instability”. In: *Proceedings of The Royal Society A* 467, pp. 1243–1269. DOI: [10.1098/rspa.2010.0485](https://doi.org/10.1098/rspa.2010.0485).
- Wolff, E. W., J. Chappellaz, T. Blunier, S. O. Rasmussen, and A. Svensson (2010). “Millennial-scale variability during the last glacial: The ice core record”. In: *Quaternary Science Reviews* 29.21-22, pp. 2828–2838. DOI: [10.1016/j.quascirev.2009.10.013](https://doi.org/10.1016/j.quascirev.2009.10.013).
- Yiou, P., K. Fuhrer, L. D. Meeker, J. Jouzel, S. Johnsen, and P. A. Mayewski (1997). “Paleoclimatic variability inferred from the spectral analysis of Greenland and Antarctic ice-core data”. In: *Journal of Geophysical Research* 102.C12, pp. 26441–26454. DOI: [10.1029/97jc00158](https://doi.org/10.1029/97jc00158).
- Young, L.-S. (2002). “What Are SRB Measures and Which Dynamical Systems Have Them?”. In: *Journal of Statistical Physics* 108.5/6, pp. 733–754.